Applications of Balanced Incomplete Block Designs to Communication systems

---

A Dissertation

Presented to

the faculty of the School of Engineering and Applied Science

University of Virginia

---

in partial fulfillment

of the requirements for the degree

Doctor of Philosophy

by

Mohammad Noshad
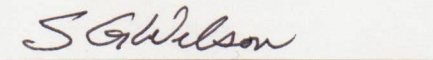
December

2013

APPROVAL SHEET

The dissertation

is submitted in partial fulfillment of the requirements

for the degree of
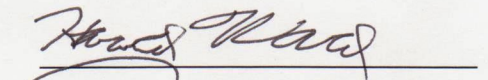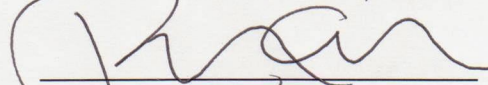
Doctor of Philosophy

_____

AUTHOR
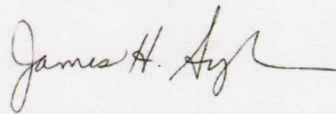
The dissertation has been read and approved by the examining committee:

_____
Advisor

_____
S G Wilson

_____

_____

_____

Accepted for the School of Engineering and Applied Science:

_____

Dean, School of Engineering and Applied Science

December

2013

Abstract

Balanced incomplete block design (BIBD) is an area of combinatorial mathematics that was first introduced in 1936 and developed very fast. Because of their unique fixed cross-correlation property, BIBDs have attracted the attention of researchers in communication systems. BIBDs have been used in various areas, such as error control coding, cryptography, code division multiple access networks, key distribution in sensor networks and watermarking. Among different BIBDs, symmetric designs are often used as codes; in order to simplify the signal processing, cyclic structures are of greatest interest.

In this dissertation, we introduce new applications of symmetric BIBDs in communication systems, with special emphasis on optical communications, and use them primarily in constructing the symbols of novel M-ary modulation schemes. The first modulation technique introduced is a spectral amplitude encoded scheme that uses BIBDs as the encoding pattern, and is shown to achieve a high bit-rate in non-line-of-sight ultraviolet (NLOS-UV) systems. The other three modulation schemes are based on pulse position modulation technique, and are proposed for application is systems with certain restrictions, such as peak-power limited systems. Because of the structure of the symbols in these modulation schemes, the symbols are susceptible to interference between adjacent time-chips, and the error probability increases in dispersive channels. We introduce a technique to decrease the interference effect on these three modulation schemes by interleaving the transmitted pulses at the transmitter and de-interleaving them at the receiver.

We then study the application of the new modulation schemes to visible light communication (VLC) systems. VLC is an appealing technology that is proposed for wireless indoor networking. Using this technique internet access can be provided by LED-based lighting system. Due to the integration of the illumination system with the communication system, it is crucial that the modulation techniques support lighting features. Dimming and low-fluctuations are the most challenging features to be supported by a communication system. We show that the proposed modulation techniques are able to provide a wide range of dimming levels and have a low fluctuation effect. We also present two techniques that enable VLC systems to provide simultaneous high-speed network access for multiple users.

Acknowledgments

First and foremost, I would like to express my sincere gratitude towards my supervisor, Professor Maïté Brandt-Pearce, for her support, encouragement, and patience during my PhD career. I enjoyed working with her, with all her considerate, thoughtful principles, and learning from her, with her vast knowledge about all aspects of my work. Her brilliant supervision, as she knew every single step that I had to take, is behind all my achievements since January 2011 in my PhD studies. I feel so blessed to work with her as her PhD student. I have been very fortunate to have Prof. Toby Berger and Prof. Stephen G. Wilson, two outstanding professors on my PhD advisory committee. I am indebted to them for learning and understanding different aspects of information and coding theory. I would also like to thank Prof. Harold Ward and Prof. Randy Cogill, my dissertation advisory committee members, whose supports and comments helped me improve this thesis.

Without the love and support of my family, this would have been a very hard journey. I am dedicating this work to my wife, Hoda, for giving me an unwavering love and support. I dare not even imagine how it would have been without you! I strive everyday to make you proud! I thank my father for teaching me good values such as hard work and appreciation for the gift of life and my mother without whom I would not be the person that I am today. My love for them is eternal. I would like to thank my parents in law, my sisters and brothers for their encouragement and support. This dissertation was impossible without their support.

I have shared numerous happy and sad moments with my friends in Charlottesville, which can hardly be expressed and acknowledged in words. I would like to thank Haiedi, Mehdi, Shahnaz and Fraidoon for their extreme support and kindness during the past three years.

Contents

List of Acronyms

AEPPM: Augmented Expurgated Pulse Position Modulation

APD: Avalanche Photo-Diode

AWGN: Additive White Gaussian Noise

BER: Bit Error Rate

BIBD: Balanced Incomplete Block Designs

BLP: Binary Linear Programming

BPPM: Binary Pulse Position Modulation

BPSK: Binary Phase Shift Keying

CCM: Code Cycle Modulation

CCR: Continuous Current Reduction

DMT: Discrete Multitone

EPPM: Expurgated Pulse Position Modulation

FOV: Field of View

FSO: Free Space Optic

FWHM: Full Width at Half Maximum

IM: Intensity Modulation

IR: Infrared

ISI: Inter-Symbol Interference

LD: Laser Diode

LED: Light Emitting Diode

LOS: Line-of-Sight

MAI: Multiple Access Interference

MEMS: Micro Electro Mechanical System

MEPPM: Multilevel Expurgated Pulse Position Modulation

ML: Maximum Likelihood

MPPM: Multi-Pulse Position Modulation

NLOS: Non-Line-of-Sight

OCDMA: Optical Code Division Multiple Access

OEPPM: Overlapping Expurgated Pulse Position Modulation

OFDM: Orthogonal Frequency Division Multiplexing

OOC: Optical Orthogonal Code

OOK: One-Off Keying

OPPM: Overlapping Pulse Position Modulation

OWC: Optical Wireless Communication

PAM: Pulse Amplitude Modulation

PAPR: Peak to Average Power Ratio

PDF: Probability Density Function

PMT: Photomultiplier Tube

PPM: Pulse Position Modulation

PWM: Pulse-Width Modulation

QPSK: Quadratic Phase Shift Keying

RF: Radio Frequency

SAC: Spectral Amplitude Coding

SNR: Signal to Noise Ratio

UV: Ultraviolet

UWB: Ultra Wide-Band

VLC: Visible Light Communication

List of Figures

i

iv

List of Tables

Chapter 1

Introduction

The primary goal of any communication system is to provide an error-free transmission of data. Among the two possible options for conveying information, digital signals are preferred over analog signals since they have the potential to detect and correct errors that are induced by noise over the transmission path. Digital communication systems utilize codes to efficiently decrease the noise effect. Codes are rules for converting a piece of information into another, not necessarily of the same type, such as letter to binary sequences, binaries to binaries, or words to ASCII codes. Codes are usually constructed based on mathematical structures that are designed to have specific properties between their elements. Combinatorial designs are one of these mathematical structures that have found many applications in communications and information theory, computer science, statistics, engineering, and life sciences. In this chapter we introduce combinatorial designs, and specifically balance incomplete block designs, which are used in the rest of this dissertation to construct new coding and modulation schemes with new applications in communication systems.

1.1   Combinatorial Designs

Combinatorial design theory is a very active area of mathematical research that deals with the existence, construction and properties of systems of finite sets whose arrangements satisfy concepts of balance and/or symmetry. As one of the fundamental discrete structures, combinatorial designs are used in fields as diverse as error-correcting codes, statistical design of experiments, cryptography and information security, mobile and wireless communications, group testing algorithms in DNA screening, software and hardware testing, and interconnection networks.

Design theory has its roots in recreational mathematics. Many types of designs that are studied

Figure 1.1: A 3×3 Latin square

today were first considered in the context of mathematical puzzles or brain-teasers in the eighteenth and nineteenth centuries. The study of design theory as a mathematical discipline really began in the twentieth century.

One of the first problems in combinatorial designs is a mathematical puzzle called "Thirty-six Officers Problem" proposed by Leonhard Euler in 1782. The question is "*Six regiments each sends a colonel, a lieutenant-colonel, a major, a captain, a lieutenant, and a sub-lieutenant. How can a delegation of these 36 officers be arranged in a regular 6×6 array such that no row or column duplicates a rank or a regiment?*". Euler correctly conjectured that this was impossible, and there is no solution for this puzzle. This problem has led to important work in combinatorics, and was the origin of the Latin Squares. A Latin square is an $n \times n$ array filled with n different letters, each occurring exactly once in each row and exactly once in each column. Figure 1.1 shows an example of a 3×3 Latin square. The "Thirty-six Officers Problem" indeed explores the existence of orthogonal Latin squares.

In 1853 Jakob Steiner rised the following question: "*For what integer N is it possible to*

Figure 1.2: Hadamard matrices with size 2, 4 and 8.

2

arrange N elements in triplets, so that every pair of elements is contained in exactly one triplet?", This problem was later extended to Steiner t-design. Thomas Kirkmans Schoolgirl Problem was a form of Steiner 2-design problem, which is "*Fifteen young ladies in a school walk out three abreast for seven days in succession: it is required to arrange them daily so that no two shall walk twice abreast*".

A Hadamard matrix is a square matrix that has +1 or -1 as its elements and each pair of rows are orthogonal. They were first invented by Sylvester in 1867 and named after the French mathematician Jacques Hadamard in honor of his work on these matrices. Because of the orthogonality of the rows, any N-dimensional space can be defined using a $N \times N$ Hadamard matrix. The Hadamard transform is introduced based on the orthogonality of Hadamard matrices. Figure. 1.2 show examples of Hadamard matrices with different sizes. Let $\mathbf{H}$ be the Hadamard matrix of order N. Then Hadamard matrix of order $2N$ is obtained as

$$\begin{bmatrix} \mathbf{H} & -\mathbf{H} \\ \mathbf{H} & \mathbf{H} \end{bmatrix}.$$

Block designs are another family of combinatorial designs. A block design is a pair (S, U) such that the following properties are satisfied:

i) S is a set of elements called points, and

ii) U is a collection (i.e., multiset) of nonempty subsets of S called blocks.

A graph can be considered as a block design in which every block has a size of 2.

1.2 Balanced Incomplete Block Designs

Modern communication systems include sophisticated modulation and signal processing algorithms, some of which rely heavily on binary code designs. In this dissertation we consider codes based on balanced incomplete block designs (BIBDs) and their applications. Because of their unique fixed cross-correlation property, BIBDs have been used in various areas, such as error control coding, cryptography, code division multiple access networks, key distribution in sensor networks and watermarking. We concentrate on existence conditions for BIBDs, designs algorithms for specific parameter sets, and applications in higher-order modulation schemes.

The origin of incomplete block designs dates back to 1936, when Yates introduced the concept of balanced incomplete block designs and their analysis utilizing both intra- and interblock information. Further contributions in BIBDs were made by Bose and Fisher in the late 1930's,

concerning the structure and construction of balanced incomplete block designs. Since then, the generation of block designs remains an unsolved problem in combinatorial mathematics [1]. Different techniques have been suggested to test the existence or non-existence of BIBDs for given parameters. But still there is no general algorithm to determine the existence of these designs. Although various construction methods have been introduced to build the elements of BIBDs for specific parameters, no general technique has been presented to find the structure of BIBDs. There are many open questions and conjectures that remain unsolved since the 1930's.

A BIBD is an incidence system (Q,K,λ,r,b), such that a set S with Q elements (called points), $\{u_1, u_2, \ldots, u_Q\}$, (i.e., $|S| = Q$ and $u_j \in S$), is divided into a family B of b subsets (called blocks), denoted as $\{U_1, U_2, \ldots, U_b\}$, each containing K elements (points) (i.e., $U_i \subset S$ and $|U_i| = K$) in such a way that each point appears in exactly r blocks and each pair of points appears in exactly λ blocks. Such a design requires that $K < Q$, which is where the "incomplete" term comes from. The five parameters Q, K, λ, r and b are not independent, and satisfy the two relations [1]

$$Qr = bK$$

$$\lambda(Q - 1) = r(K - 1).$$

A BIBD can be denoted by (Q,K,λ), since b and r are functions of these three parameters.

A BIBD is called symmetric if $Q = b$ and, equivalently, $K = r$. Symmetric BIBDs, denoted by (Q, K, λ), have the following relation:

$$\lambda(Q - 1) = K(K - 1). \tag{1.1}$$

A (Q, K, λ)-design is determined by its incidence matrix: this is the binary $Q \times Q$ matrix $\mathbf{C} = [c_{ij}]$ defined by

$$c_{ij} = \begin{cases} 1 & \text{if } u_j \in U_i, \\ 0 & \text{otherwise} \end{cases}.$$

BIBD codes are defined as a set of Q binary codewords with length Q and weight K, in which each pair of codewords has a fixed cross-correlation of λ. Hence, defining $\mathbf{c}_i = [c_{i1}, c_{i2}, \ldots, c_{iQ}]$ as the ith codeword, we have

$$\sum_{k=1}^{Q} c_{ki} c_{kj} = \begin{cases} K & i = j, \\ \lambda & i \neq j \end{cases}. \tag{1.2}$$
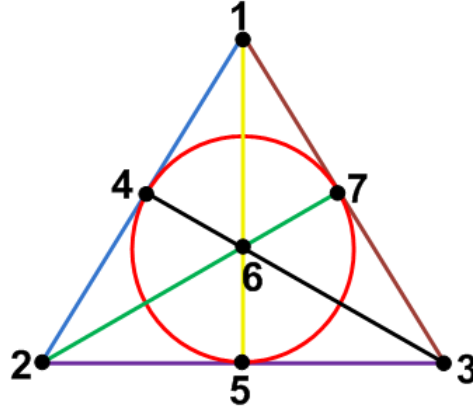
Figure 1.3: Fano plane

A list of available symmetric BIBDs can be found in [2]. A simple example of symmetric BIBDs is the Fano plane with parameters (7,3,1) as shown in Figure 1.3. This structure has seven points numbered from 1 to 7 and seven lines with different colors. There are exactly three points on each line, and exactly three lines passes through a point. Every two points define a line, and every two lines intersects at a point. The incident matrix of this Fano plane is

$$
\mathbf{C} = \begin{bmatrix}
1 & 1 & 0 & 1 & 0 & 0 & 0 \\
0 & 1 & 1 & 0 & 1 & 0 & 0 \\
0 & 0 & 1 & 1 & 0 & 1 & 0 \\
0 & 0 & 0 & 1 & 1 & 0 & 1 \\
1 & 0 & 0 & 0 & 1 & 1 & 0 \\
0 & 1 & 0 & 0 & 0 & 1 & 1 \\
1 & 0 & 1 & 0 & 0 & 0 & 1
\end{bmatrix}.
$$

Examples of symmetric designs are affine planes with parameters $(n^2, n, 1)$, and projective planes with parameters $(n^2 + n + 1, n + 1, 1)$ [1]. Table 1.1 lists some set of parameters for existing BIBD codes. The parameters of the cyclic BIBDs can be written in the form of $Q = tK + 1$, and $K = t\lambda + 1$ for most cases and for certain t's. The only cyclic BIBD that does not fit in this category is the $(109, 28, 7)$-BIBD. Some of the non-cyclic BBIDs are also listed in this table.

Table 1.1: List of parameters for which BIBDs exist

$Q = 2K+1,$ $K = 2\lambda+1$	$Q = 3K+1,$ $K = 3\lambda+1$	$(341,85,21)$	$Q = 9K+1,$ $K = 9\lambda+1$
$(7,3,1)$	$(10,4,1)$	$(677,169,42)$	$(91,10,1)$
$(11,5,2)$	$(31,10,3)$	$(901,225,56)$	$(820,91,10)$
$(15,7,3)$	$(40,13,4)$	$Q = 5K+1,$ $K = 5\lambda+1$	Non-Cyclic BIBDs
$(19,9,4)$	$(121,40,13)$	$(31,6,1)$	
$(23,11,5)$	$(364,121,40)$	$(156,31,6)$	$(16,6,2)$
$(31,15,7)$	$Q = 4K+1,$ $K = 4\lambda+1$	$(781,156,31)$	$(45,12,3)$
$(35,17,8)$	$(21,5,1)$	$Q = 7K+1,$ $K = 7\lambda+1$	$(27,13,6)$
$(43,21,10)$	$(37,9,2)$	$(57,8,1)$	$(36,15,6)$
$(47,23,11)$	$(85,21,5)$	$(400,57,8)$	$(96,20,4)$
$(59,29,14)$	$(101,25,6)$	$Q = 8K+1,$ $K = 8\lambda+1$	$(64,28,12)$
$(67,33,16)$	$(133,33,8)$	$(73,9,1)$	$(175,30,5)$
$(71,35,17)$	$(197,49,12)$	$(585,73,9)$	

1.3 Applications of Combinatorial Designs

Many applications of combinatorial designs have been proposed in communications, cryptography, statistics, lottery, quantum computing, and many other areas. Some detailed applications are as follows

Error-Correcting Codes: Channel coding is a technique used for controlling and correcting errors in data transmission over noisy channels. This technique utilizes error-correcting codes, which are algorithms for expressing sequences of symbols such that any errors that are introduced can be detected and corrected using the remaining symbols. BIBDs have been used to construct a new family of error-correcting codes [3], [4]. The codewords of BIBD are used as the rows of the parity-check matrix [5].

Authentication Codes: Researchers in the field of information security and cryptography are perpetually challenged to respond to new threats to information systems. In cryptography, an au-

thentication code is a short chunk of information used to authenticate a message and to provide integrity and authenticity assurances on the message. Integrity assurances decipher any changes in the message, while authenticity assurances acknowledge the origin of the message. Combinatorial designs, specially partial balanced designs can be useful in the construction of perfect authentication structures [6].

Group Testing and Superimposed Codes: Group testing is a combinatorial scheme developed for the purpose of efficient identification of infected individuals in a given pool of subjects. The main idea behind the approach is that if a small number of individuals are infected, one can test the population in groups, rather than individually, thereby saving in terms of the number of tests conducted. The coding schemes that are used for this testing are called superimposed codes. A family of superimposed codes are constructed based on block designs and Latin squares [7], [8], [9].

Quantum Computing: A Hadamard gate is a quantum gate that act on a single qubit, and maps $|0\rangle$ into $\frac{|0\rangle+|1\rangle}{\sqrt{2}}$ and $|1\rangle$ into $\frac{|0\rangle-|1\rangle}{\sqrt{2}}$. The Hadamard transform is also a crucial part of Shor's algorithm [10] in quantum computing.

Key Distribution Mechanisms: Secure communications in wireless sensor networks require providing symmetric keys to sensor nodes. New approaches based on combinatorial designs are proposed in [11] in order to decide how many and which keys to assign to each key-chain before sensor network deployment.

Lottery: Lotto is a gambling game in which a player buys a ticket, and hereby chooses k numbers from n numbers. At a certain point the organizers of the game stop selling the tickets, and p winning numbers are selected randomly from the n numbers. If any of the tickets sold match t of the winning numbers, the holder of the ticket receives a prize; usually t must be three or more to win a prize. The larger the value of t, the larger the prize. Many researches have been done to find the minimum number of tickets necessary to ensure that at least one ticket will intersect the winning numbers in t or more numbers, for different t's. BIBDs are found to be helpful in designing a lottery with given parameters (n, k, p, t) [12].

1.4 Contributions

The main contributions of this dissertation are:

- A new spectrally encoded M-ary modulation technique is introduced that increases the data-rate in free space optical communication systems. Transmitter and receiver structures are also presented for this modulation scheme.

- A modified form of pulse-position modulation (PPM), called expurgated PPM (EPPM), is introduced, which is able to decrease the error-probability for unipolar peak-power limited systems.

- Multilevel EPPM (MEPPM), a spectrally efficient multilevel modulation technique, is proposed for use in dispersive channels.

- A spectrally efficient modulation scheme is obtained by combining BIBD codes with quadrature-phase-shift-keying (QPSK), which is called coded-QPSK and is well suited to RF communication systems.

- An interleaving technique is suggested to be applied on EPPM, MEPPM and coded-QPSK to significantly decrease the channel-induced inter-symbol interference (ISI) effect.

- Overlapping pulses are proposed to increase the bit-rate of EPPM, MEPPM and coded-QPSK for system with band-limited sources.

- EPPM and MEPPM are used in visible light communication (VLC) systems and are shown to be able to support the dimming feature in lighting systems.

- Two networking techniques are introduced for use in VLC systems, which enables simultaneous access for a large number of users.

1.5 Organization of the Thesis

The remainder of the dissertation is organized as follows.

Chapter 2 describes non-line-of-sight (NLOS) ultraviolet (UV) communication systems, and presents a new closed-form link-loss for NLOS-UV channels. It proposes an application of BIBDs to these systems by using the codewords of a BIBD as spectrally amplitude modulated symbols.

This enables NLOS-UV systems to send the information using an M-ary scheme and transmit the data at higher bit-rates. Transmitter and receiver structures using lasers, light-emitting-diodes (LED) arrays, avalanche-photodiodes (APD) and photomultiplier-tubes (PMT) are proposed. Then the results are compared to conventional modulation techniques such as on-off keying (OOK).

New modulation schemes based on pulse-position modulation techniques are introduced in Chapter 3. In this chapter, BIBDs are used to construct symbols of modulation techniques. The first modulation is presented to improve the performance of the popular pulse-position modulation (PPM) in unipolar optical peak power limited system, and then a multilevel form of it is introduced to increase the spectral efficiency, which is defined as the bit-rate than can be transmitted over a given bandwidth. A modified form of this modulation is adapted to radio-frequency (RF) communication systems with phase-encoding possibility.

Chapter 4 introduces visible light communications (VLC), and proposes to apply the modulation schemes of Chapter 3 to indoor optical wireless communication systems. These modulation techniques are shown to be compatible with the lighting features such as dimming, and have the potential to transmit data for a wide range of peak to average power ratios (PAPR). Two multiple-access methods are presented for VLC networks in this chapter to support simultaneous access for multiple users. Using these techniques high-speed network access can be provided for a large number of users.

Two techniques are presented in Chapter 5 in order to increase the bit-rate of the proposed modulation schemes in channel and/or source band-limited systems. A lower bound on the performance of the optimum interleaver is derived. Numerical results are presented to show the performance of interleaving for visible light communication systems with multipath effect.

Chapter 6 discusses some of the open problems in combinatorial designs, and presents a new approach to deal with the existence of these designs. Finally Chapter 7 summarize the dissertation and proposes avenues for future research.

Chapter 2

Applications of BIBDs in NLOS UV Communication Systems

In this chapter we present an M-ary spectral amplitude code (SAC) modulation technique to improve the performance of free-space optical (FSO) communication systems. Although this approach can be used in any dispersive FSO system, in this work we focus on non-line of sight (NLOS) ultraviolet (UV) systems relying on atmospheric scattering.

A broadband optical source is required for SAC. Thus, since high-power broadband UV sources are scarce, widely-available broadband lasers in visible spectrum are proposed as transmitter light sources. The encoding is done in the visible/infrared (IR) region, and then the encoded signal is frequency-doubled (or tripled) to the UV range. We use symmetric BIBDs to construct spectrally encoded symbols. A differential structure using two photomultiplier tubes is utilized in conjunction with various demodulation algorithms to decode the received signal. The symbol time, T_s, is divided into smaller time slots and in each symbol interval decoding is done using a symbol-by-symbol detector. Optimum single PMT, optimum dual PMT, and optimum linear dual PMT demodulation are considered as the three options for making a decision on the received signal. The performance of the linear detector is shown to be close to that of the optimum detector. Intersymbol interference (ISI), received beam divergence and shot noise are considered as the main factors limiting the system performance. An analytical upper bound for the error probability is derived and compared with simulation results for various geometries and for different code parameters. The maximum bit rate for a fixed bit error probability is calculated in terms of the link length, and results for different alphabet sizes are shown. The performance of the optimum

linear dual PMT detector with various alphabet sizes is analyzed by considering the ISI, received beam divergence and shot noise. Through our numerical results we show that M-ary SAC can achieve higher distance-rate products compared to OOK. By sacrificing spectral efficiency without becoming more susceptible to ISI, the proposed system can support higher rates and longer distances for the same performance compared with on-off keying systems.

The results in this chapter have been published in [13], [14] and [15]. This chapter is organized as follows. Section 2.1 introduces NLOS UV systems. In Section 2.2 the configuration of the transmitter is described. Section 2.3 describes the channel model. Several structures for the receiver using PMTs are presented in Section 2.4. The analytical bit error probability is calculated in Section 2.5, using an upper bound. Then the system performance is analyzed using numerical results in Section 2.6. Finally, Section 2.7 summarize the chapter.

2.1 Introduction to Non-line-of-Sight Ultraviolet Communication Systems

Line-of-sight (LOS) communications is the primary way to set up a link between two point, in which the data is transmitted via the direct path from transmitter to receiver. In some situations this path is blocked by an obstacle, and LOS communication is not possible. In this case, non-line-of-sight (NLOS) communications is used to convey the information from transmitter to receiver. NLOS communications has attracted increasing interest because of its relative insensitivity to pointing errors and robustness against shadowing. FSO is one of the options that is considered for fulfilling NLOS communications [16]. Optical scattering is the key feature for transmitting optical signals via a NLOS path, using a part of the transmitted optical beam which is scattered by the air molecules and aerosols[1] and detected by the receiver. Atmospheric scattering in the UV band is higher than in other optical bands, and, consequently, in NLOS systems the receiver can receive more power from the transmitter than if it used another portion of the optical spectrum [17], making the UV band an interesting choice for NLOS communications [16]. Furthermore, background irradiance severely limits the performance of NLOS infrared and visible light optical communications, while the ultraviolet (UV) band (200-280 nm) has low background light because of sunlight filtering by the upper atmosphere [16]. Yet the strong scattering in the NLOS UV channel imposes a temporal dispersion on the transmitted optical pulses. Thus, both intersymbol

---

[1]suspended solid particles in the air

Figure 2.1: Illustration of a NLOS-UV system in an urban area [photo by Google Maps].

interference (ISI) and low received power can be factors limiting the data rate in NLOS UV links
[18].

Figure 2.1 shows a NLOS UV network over an urban area, UV transmitter and receivers
are installed on the roofs of the buildings. In this case NLOS UV communications is used to
set up a network between multiple buildings since the direct path between them are blocked by
other constructions. NLOS UV can be used in urban areas as a back-up network since it has an
unlicensed spectrum.

An experimental demonstration of a NLOS UV communication system using OOK and PMTs
is reported in [19], but communications is limited to 500 Kb/s and 200 m range. In this work we
propose single-user M-ary modulation and demodulation techniques to combat the channel ISI
degradation and increase the distance-rate product of NLOS UV systems. The distance-rate prod-
uct is an important measure for evaluating the performance of optical communication systems. It
is defined as the product of the transmitter-receiver distance of the optical channel and its maxi-
mum achievable data rate for a predefined maximum acceptable bit error probability. This product
is usually limited by either intersymbol interference (ISI) or low signal to noise ratio (SNR). Error

12

correcting codes, equalization and M-ary transmission are the most common techniques for increasing the distance-rate product in both radio frequency (RF) and optical communications. The maximum data rate versus the distance between the transmitter and receiver has been presented in previous work on NLOS UV communications for on-off keying (OOK) and different system geometries [18], [20].

2.2 Transmitter Structure

In this section we propose two structures for spectrally encoding the UV light. In the first structure, as shown in Figure. 2.2, an array of wide spectrum LEDs is used as the UV source. The output light of the LEDs is collimated upon a diffraction grating. The diffraction grating reflects each wavelength with a specific angle that depends on the physical parameters of the grating and the angle of the incident beam. A lens is placed in front of the grating so that the combination of the grating and lens decomposes the spectral components of the light source and focuses them on an encoder mask. The encoder mask is formed by Q elements, each of which passes or blocks its corresponding wavelength according to the desired codeword. After the encoder mask, another lens and diffraction grating are used to recombine the encoded light. For this structure, a broadband UV source is required, and since high-power broadband UV sources are scarce and
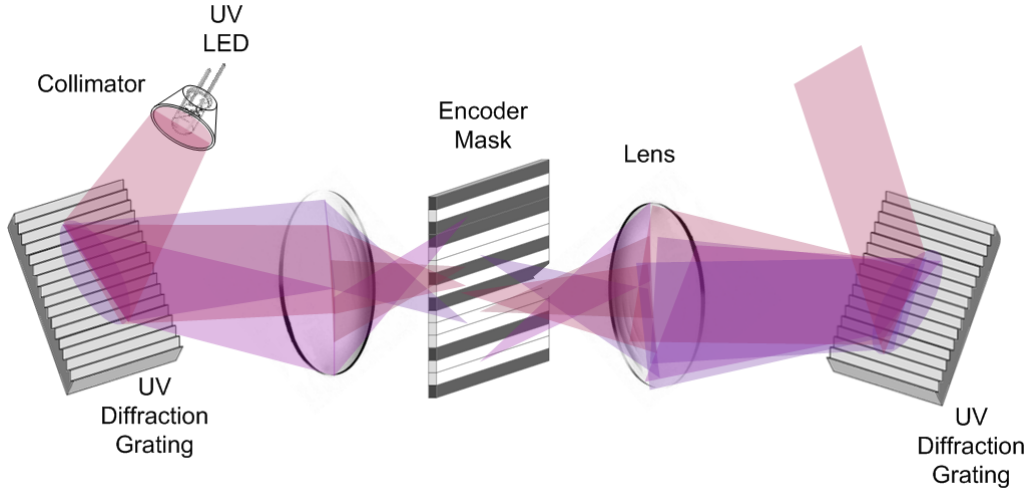
Figure 2.2: Transmitter structure using diffraction gratings for spectral encoding in the UV domain.
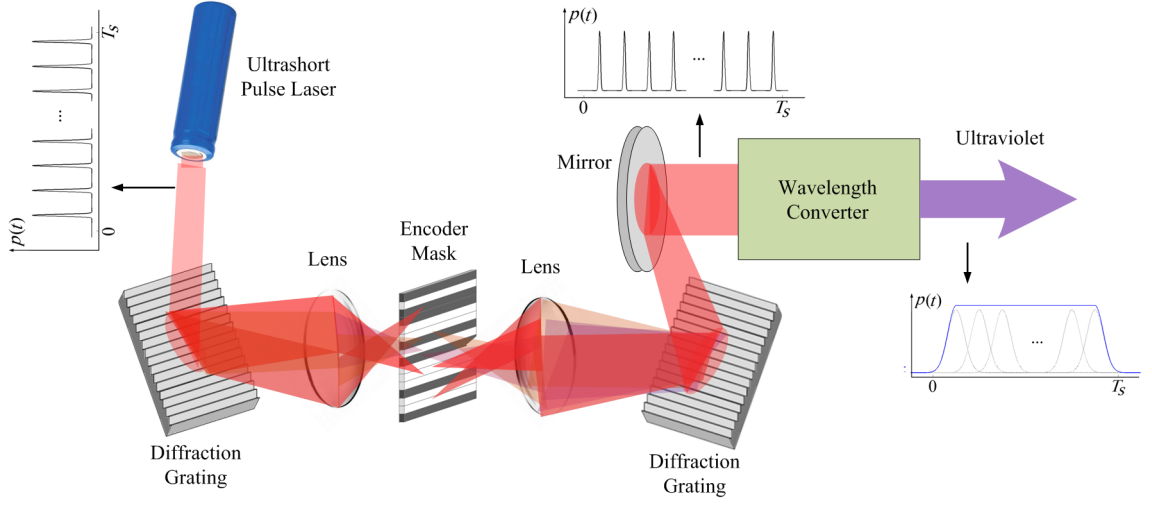
Figure 2.3: Transmitter structure applying spectral amplitude encoding in the visible/IR region and wavelength conversion to the UV band.

expensive, this transmitter is not a good option for encoding data in UV band. On the other hand, broadband spectrum visible lasers are widely-available, and therefore, in the second structure the encoding is proposed to be done in the visible/infrared (IR) region, and then the encoded signal is frequency-doubled (or tripled) to the UV range.

Figure 2.3 illustrates the second proposed structure of the transmitter using spectral encoding. The transmitter is composed of three parts: a wideband optical source in the visible or IR region, an optical encoder, and a wavelength converter, which transforms the encoded light to the UV range. A laser with wide spectrum (~ 20 nm) and subpicosecond pulses[1], such as a Ti-Sapphire laser, is a good option for the source. These lasers are able to generate ultrashort light pulses with high repetition rate (~ 80 M pulses/sec), much more frequent than the symbol rate considered here.

The output light from the wide spectrum source is collimated upon a diffraction grating. The diffraction grating reflects each wavelength with a specific angle, which depends on the physical parameters of the grating and the angle of the incident beam. A lens is placed in front of the grating so that the combination of the grating and lens decomposes the spectral content of the source light and focuses it on an encoder mask. The encoder mask consists of Q elements, each of which passes or blocks its corresponding wavelength according to the desired codeword. The

---

[1]This property is required to achieve higher conversion efficiency in the wavelength converter.

electrically-controlled encoder mask is changed at the start of each symbol period, depending on the symbol that has to be transmitted. After the encoder mask, another set of lens and diffraction grating are used to recombine the components of the encoded light. In this way, we obtain a coded output in the visible or IR light region and, since we apply amplitude encoding but no phase encoding on the ultrashort pulses, the encoded pulses still have sub-picosecond duration.

The last part of the transmitter is a wavelength converter, which uses harmonic generation in a nonlinear crystal, such as β-Barium Borate (BBO), β-BaB$_2$O$_4$ [21], or Lithium Triborate (LBO), LiB$_3$O$_5$ [22], to convert the encoded signal to UV light. The nonlinear crystal is placed inside an optical cavity in order to increase the conversion efficiency. Detailed configurations for using a wavelength converter to generate UV light are described in [23] and [24]. Due to the nonlinear effect and because of the cavity, the ultrashort pulses are broadened at the output of the wavelength converter, so that the rapid pulse-train now appears as an almost-rectangular pulse of duration T_s. Transmit power levels on the order of 1 W are easily attainable using this second technique, and it is therefore the best approach for generating a spectrally encoded UV signal. We assume this transmitter structure for the remainder of the chapter.

In this work, for our M-ary modulation we use the BIBD codes described in Chapter 1 that have been proposed for multiple access in SAC-OCDMA systems [25]. In order to make the control of the encoder and decoder masks simpler, we use cyclic codes, for which the codewords are cyclic shifts of each other [1]. In this case, the number of codewords in one code is equal to the code length ($M = Q$), and the entire code can be characterized by any codeword. The transmitted vector at symbol time k is $\mathbf{s}_k = [s_{k1}, s_{k2}, \ldots, s_{kQ}] \in \{\mathbf{c}_1, \mathbf{c}_2, \ldots, \mathbf{c}_Q\}$.

The linewidth of the source is divided into Q wavelength bins by the encoding mask. We denote the transmitted pulse shape at wavelength bin q, $q = 1, 2, \ldots, Q$, and in symbol interval $k = 0$ by $\mathcal{F}_q(t)$, resulting from the many temporally-dispersed ultrashort pulses in one symbol time. So the transmitted signal intensity at wavelength q is

$$p_T^{(q)}(t) = \sum_{k=-\infty}^{\infty} s_{kq}\, \mathcal{F}_q(t - kT_s), \tag{2.1}$$

where T_s is the symbol time. The total optical intensity transmitted is the sum of these modulated signals at adjacent wavelengths.
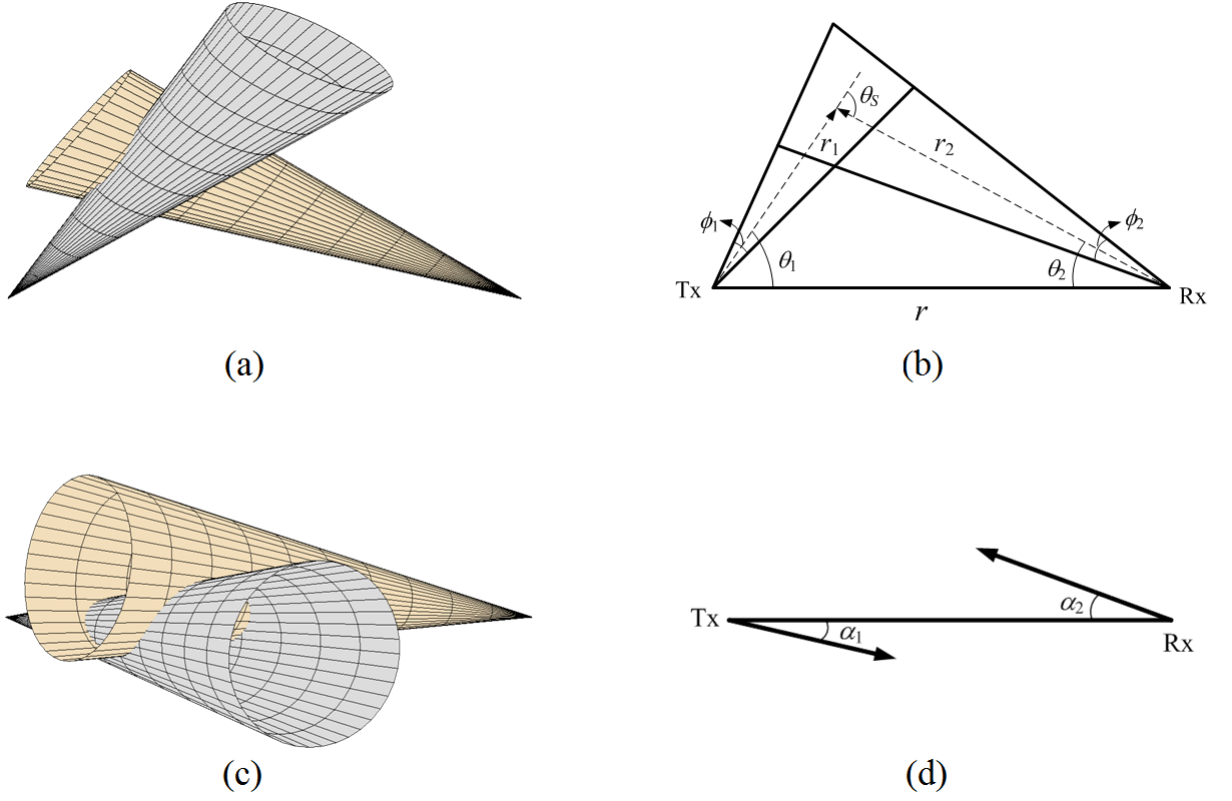
Figure 2.4: Geometry of the NLOS UV link.

2.3 Channel Model

Analyzing the performance of NLOS UV communication systems requires a model of the path loss and the impulse response of the channel. Many techniques have been presented to accurately model the NLOS UV channel. A simulation approach that uses a Monte Carlo method for multiple scattering interactions is presented by Ding et al. [18] and by Drost et al. [26]. An analytical approximation can be remarkably helpful for getting a fast initial scope of the link performance. Luettgen, Shapiro, and Reilly [27] present an analytical model in integral form for the impulse response by considering only the single scatter propagation. Xu [28] analyzes the performance of NLOS UV links using a single scattering approximation. An approximate closed form path loss for NLOS UV links with small transmitted beam-widths and small fields of view (FOV) is calculated [28]. The common volume between the transmitted beam and receiver FOV is approximated by a frustum and, in this way, a closed form expression for path loss is obtained [20]. Recently, another approximate link loss is calculated for noncoplanar geometries [29].

16

Figure 2.4 shows the geometry of the NLOS UV link that we use in this work. Figure 2.4-(a) is the 3D side view of a NLOS UV link, where the violet cone is the transmitted beam, and pink cone indicates the receiver field of view. Figure 2.4-(b) shows the transmitter and receiver axes, the transmitted beam-width, and the receiver field of view. The transmitter and receiver are located at distance r from each other. We denote the transmitter beam full-width divergence by ϕ_1, the receiver field of view (FOV) by ϕ_2, the transmitter elevation angle by θ_1 and the receiver elevation angle by θ_2. Figure 2.4-(c) is the 3D top view of the link, and Figure 2.4-(d) shows the transmitter and receiver axes respectively with azimuth angle α_1 and α_2 from the top view.

In NLOS UV systems, the transmitted pulse is spread in the time domain due to the large scattering volume and the strong atmospheric scattering of the UV band. The received signal at wavelength q, $p_R^{(q)}(t)$, can be obtained by convolving the channel intensity impulse response in wavelength q, $h_q(t)$, with the transmitted signal in that wavelength, $p_T^{(q)}(t)$. So for the received signal intensity we have

$$p_R^{(q)}(t) = \sum_{k=-\infty}^{\infty} s_{kq} \big[\mathcal{F}_q(t - kT_s) * h_q(t) \big], \ q = 1, 2, \ldots, Q. \tag{2.2}$$

In this work we use the impulse-response model presented in [14]. In this model, the common volume between the transmitter and receiver is divided into small cubic volumes, and then numerical integration is used to calculate the impulse response of a NLOS-UV link.

2.3.1 Analytical Approximation for Link Loss

In this section, a closed form analytical approximation for the loss in the NLOS UV channel is presented.

A detailed geometry of a NLOS UV channel is illustrated in Figure 2.5. According to previous work [20], the received energy from volume dV is

$$dE_r \approx \frac{E_t k_s P(\mu) A_r dV \sin^4(\theta_1 + \theta) \exp[-k_e r \frac{\sin\theta_1 + \sin\theta}{\sin(\theta_1 + \theta)}]}{2\pi r^4 \sin^2\theta_1 \sin^2\theta (1 - \cos\frac{\phi_1}{2})}, \tag{2.3}$$

where E_t is the total transmitted energy and θ is the angle between the base line and the line that connects the center of the volume to the receiver, as shown in Figure 2.5. According to Figure 2.5, we divide the receiver FOV into differential angles. We assume that $\phi_1 < \phi_2$, which holds for practical NLOS UV links. In this way, the volume intersecting the transmitted beam and the differential angle $d\theta$ can be approximated as a elliptical-cylinder. The volume of this cylinder is equal to $A_s dx$, where A_s is the area of its elliptical surface, and dx is the thickness of the cylinder

17

given by $dx = r_2'd\theta$. According to Figure 2.6, A_s is equal to $A_s'/\sin\theta_S'$, where $\theta_S' = \theta_1 + \theta$ and A_s' is a surface perpendicular to the transmitter axis, and therefore a circle. Thus A_s' is equal to $r_1^2\phi_1^2\pi/(4\sin(\theta_1 + \theta))$. Using these parameters, dV becomes

$$dV = \frac{\pi}{4\sin(\theta_1 + \theta)} r_1^2 r_2' \phi_1^2 d\theta. \tag{2.4}$$

Using (2.4), (2.3) simplifies to

$$dE_r = \frac{E_t k_s P(\mu) A_r \phi_1^2 d\theta \exp[-k_e r \frac{\sin\theta_1 + \sin\theta}{\sin(\theta_1 + \theta)}]}{8r\sin\theta_1(1 - \cos\frac{\phi_1}{2})}. \tag{2.5}$$

The total received energy can be obtained by integrating over dE_r as

$$E_r = \int dE_r = \int_{\theta_2 - \frac{\phi_2}{2}}^{\theta_2 + \frac{\phi_2}{2}} \frac{E_t k_s P(\mu) A_r \phi_1^2 \exp[-k_e r \frac{\sin\theta_1 + \sin\theta}{\sin(\theta_1 + \theta)}]}{8r\sin\theta_1(1 - \cos\frac{\phi_1}{2})} d\theta, \tag{2.6}$$

where μ is assumed to be $\cos(\theta_1 + \theta_2)$.

Defining the parameter τ as

$$\tau = \frac{1 - \cos(\theta_1 + \theta)}{\sin(\theta_1 + \theta)}, \tag{2.7}$$

we have

$$E_r = X \int_{\tau_1}^{\tau_2} \frac{2}{1 + \tau^2} e^{-B\tau} d\tau, \tag{2.8}$$
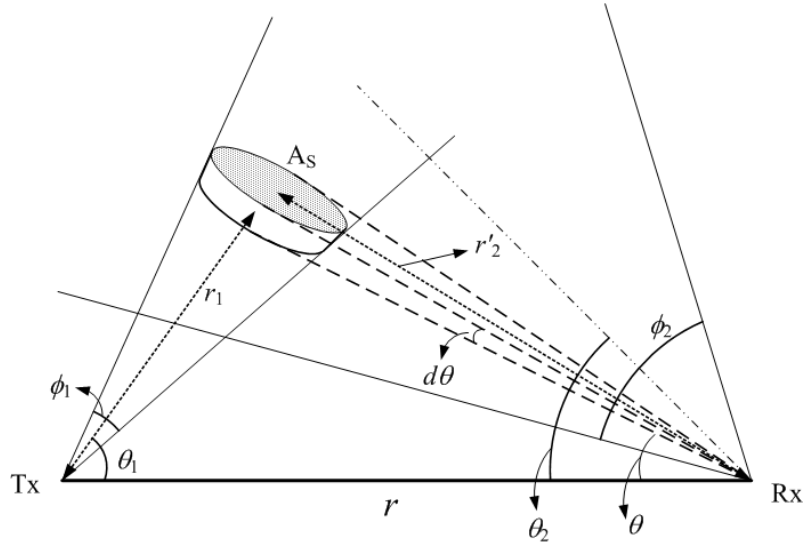
Figure 2.5: The intersection volume between the transmitted beam and differential FOV, $d\theta$.

where

$$X = \frac{E_t k_s P(\mu) A_r \phi_1^2}{8r \sin\theta_1 (1 - \cos\frac{\phi_1}{2})} e^{-k_e r \cos\theta_1}, \tag{2.9}$$

$$\tau_1 = \frac{1 - \cos(\theta_2 - \frac{\phi_2}{2})}{\sin(\theta_2 - \frac{\phi_2}{2})}, \tag{2.10}$$

$$\tau_2 = \frac{1 - \cos(\theta_2 + \frac{\phi_2}{2})}{\sin(\theta_2 + \frac{\phi_2}{2})}, \tag{2.11}$$

and $B = k_e r \sin\theta_1$. In obtaining (2.8), we used

$$\sin(\theta_1 + \theta) = \frac{2}{\tau + 1/\tau}, \tag{2.12}$$

and

$$d\theta = \frac{\sin^2(\theta_1 + \theta)}{1 - \cos(\theta_1 + \theta)} d\tau = \frac{2}{\tau^2 + 1} d\tau. \tag{2.13}$$

Integrating over τ in (2.8) gives us

$$E_r = \left[2X e^{-B\tau} \tan^{-1}\tau \right]_{\tau_1}^{\tau_2} + 2XB \int_{\tau_1}^{\tau_2} \tan^{-1}\tau e^{-B\tau} d\tau. \tag{2.14}$$

We approximate $\arctan\tau$ in the second term of (2.14) by

$$\tan^{-1}\tau = C(\tau_1, \tau_2)\tau + D(\tau_1, \tau_2), \tag{2.15}$$
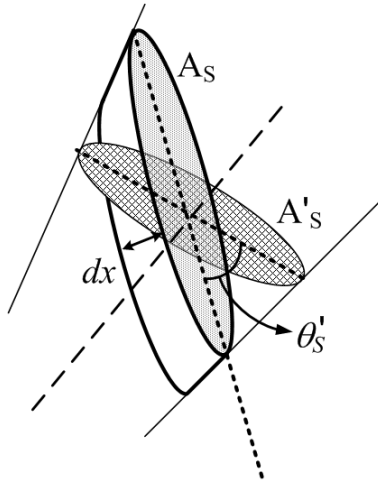
Figure 2.6: The elliptical-cylinder differential volume with thickness dx and surface area A_s.

19

over interval $[\tau_1, \tau_2]$, where $C(\tau_1, \tau_2) = \frac{\tan^{-1}\tau_2 - \tan^{-1}\tau_1}{\tau_2 - \tau_1}$ and $D(\tau_1, \tau_2) = \frac{\tau_2\tan^{-1}\tau_1 - \tau_1\tan^{-1}\tau_2}{\tau_2 - \tau_1}$.
Substituting (2.15) in (2.14) gives us

$$E_r \approx 2C(\tau_1, \tau_2)\frac{X}{B}\left[e^{-B\tau_1} - e^{-B\tau_2}\right]. \tag{2.16}$$

In (2.16) we approximate the received energy by integrating over the differential received energy in the receiver FOV, and therefore, by increasing the FOV, unlike the previously presented closed-form path loss approximations, the path loss presented in (2.16) stays close to the exact value.

2.3.2 Numerical Results

In this section numerical results for the path loss is presented, and the results from different methods are compared.

The path loss of the NLOS UV link is depicted in Figure 2.7 for $\theta_1 = 80°$, $\theta_2 = 60°$, $\phi_1 = 10°$ and $\phi_2 = 30°$. The scattering and extinction coefficients are considered to be $k_s^{Ray} = 0.24\ \text{km}^{-1}$, $k_s^{Mie} = 0.25\ \text{km}^{-1}$ and $k_a = 0.9\ \text{km}^{-1}$. The path loss is plotted for measurement from Xu et al. [20], Luettgen-Shapiro-Reilly method [27], numerical integration method from [14], closed-form
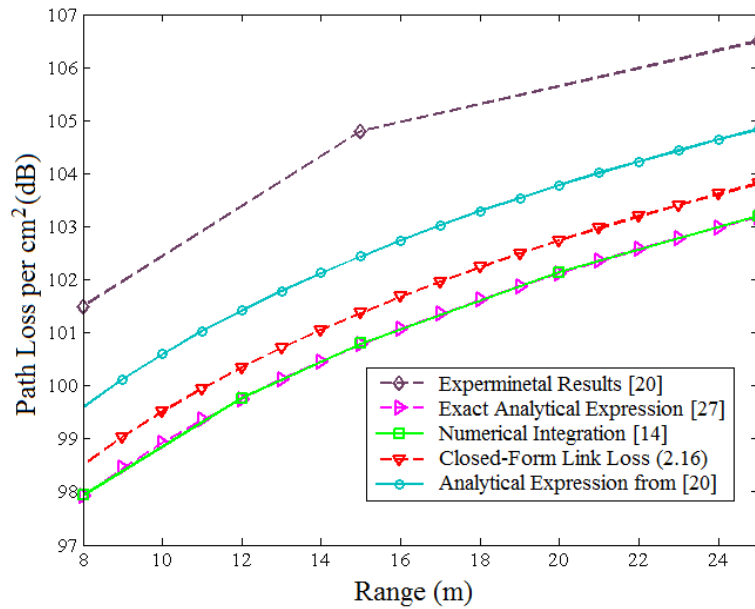
Figure 2.7: Path loss vs. the range for $\theta_1 = 80°$, $\theta_2 = 60°$, $\phi_1 = 10°$ and $\phi_2 = 30°$, using different methods.

20
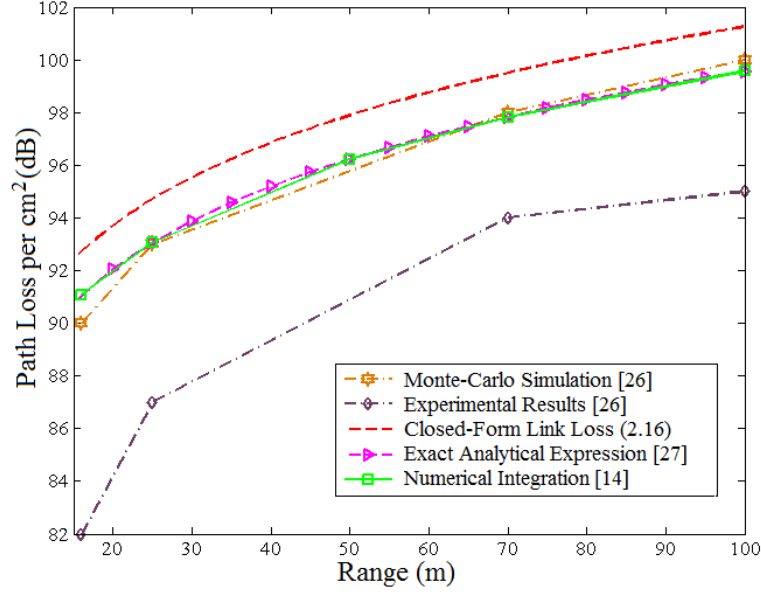
Figure 2.8: Path loss vs. the range for $\theta_1 = 20°$, $\theta_2 = 30°$, $\phi_1 = 17°$ and $\phi_2 = 30°$, using different methods.

expression from (2.16), and the analytical approximation calculated by Xu et al. [20]. As can be seen the path loss using the numerical integration exactly matches the Luettgen-Shapiro-Reilly method plot. Also the proposed closed-form approximation is closer to the Luettgen-Shapiro-Reilly and numerical integration plots than the approximate expression presented by Xu et al. [20]. The difference between the measurement results and the other results in all figures can be because of a difference in the modeling a real situation, or the effect of some un-modeled parameters.

Figure 2.8 shows the path losses for geometry $\theta_1 = 20°$, $\theta_2 = 30°$, $\phi_1 = 17°$ and $\phi_2 = 30°$. The measurement and Monte Carlo results are taken from Drost et al. [26]. In Figure 2.9 the path losses from different methods are plotted for $\theta_1 = 40°$, $\theta_2 = 20°$, $\phi_1 = 10°$, $\phi_2 = 30°$, using the same scattering and extinction coefficient as for Figure 2.8. The path loss results from the numerical integration [14] and the Luettgen-Shapiro-Reilly method [27] matches exactly. The path loss using the Monte Carlo simulation technique, though considering multiple scattering, is remarkably close to these two plots. The approximated link loss from the closed-form expression given in (2.16) also has a reasonable accuracy. The measurement and Monte Carlo path losses are plotted using the results in Ding et al. [18].
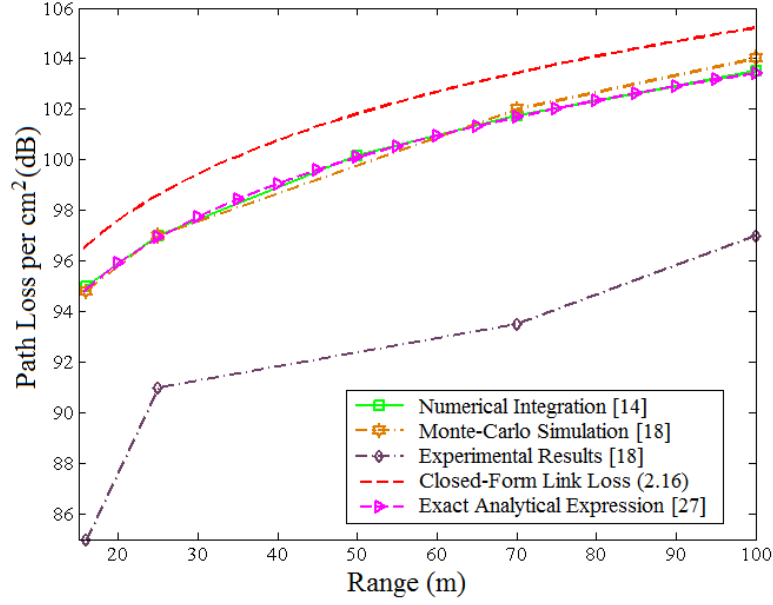
Figure 2.9: Path loss vs. the range for $\theta_1 = 40°$, $\theta_2 = 20°$, $\phi_1 = 17°$ and $\phi_2 = 30°$, using different methods.

2.4 Receiver Structure

In this section we propose two receiver structures. Figure 2.10 shows the first receiver configuration based on an UV APD array. In this structure, similar to the transmitter, the wavelength components of the received signal are separated from each other by using a diffraction grating. They are then detected by an array of APDs independently [30]. We need Q APDs to resolve all of the spectral content of the received signal and make a symbol decision based on these Q variables. As illustrated in Figure 2.11, the outputs of the APDs are fed into the decision circuit, which then estimates the symbol $\hat{m}_k$ for the kth time instance, based on a maximum likelihood (ML) rule. Since the noise of all APDs are equal to each other, the ML criterion can be simplified to a minimum distance rule [31].

In the first structure, an APD array is used for extracting the received signal in each wavelength. However, because of the low gain of the APD arrays in the UV range and the small aperture size of each element of the array, the system is not able to transmit data for distances longer than 100 m. Photomultiplier tubes (PMT) are a better choice for detecting weak signals. The optimum receiver for SAC UV systems requires Q PMTs (one PMT for each wavelength), which, considering the size and price of PMTs, is impractical and not cost effective. Here, we

propose a structure using one or two PMTs, which is sub-optimal but practical.

Our second structure for the UV receiver using two PMTs (e.g. R1584; Hamamatsu[1]) is shown in Figure 2.12. We use a UV filter (e.g. Edmund Optics; 254 nm center wavelength, 40 nm FWHM bandwidth[2]) to limit the background noise on the receiver. Consequently, and considering that the background radiation is extremely low in the UV range wavelengths of 250 nm - 280 nm, we neglect the effect of the background light in this chapter. Because of the high efficiency of the second structure we use it as the receiver in the rest of the chapter and do the analysis only for the second structure.

2.4.1 Spatial Broadening Due to the Wide Receiver FOV

In the receiver, a UV diffraction grating (e.g., 3600 grooves/mm; 0.25 nm/mr dispersion at 250 nm; LaserComponents[3]) and lens are used for decomposing the spectrum of the received beam.

---

[1]http://sales.hamamatsu.com/en/products/electron-tube-division/detectors/photomultiplier-tubes/part-r1584.php

[2]http://www.edmundoptics.com/products/displayproduct.cfm? productID=1903&dc&PageNum=2

[3]http://www.lasercomponents.com/fileadmin/user_upload/home/Datasheets/ optometr/gratings.pdf
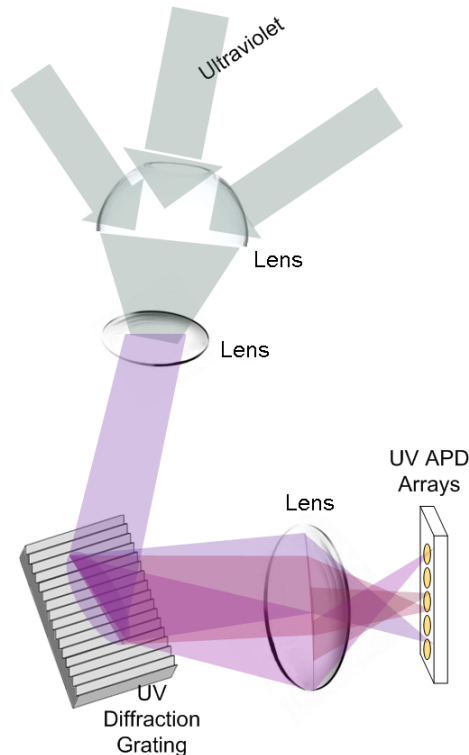
Figure 2.10: Receiver structure for the UV system using an APD array.
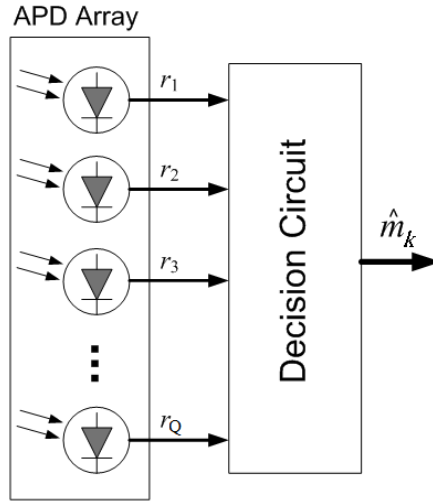
Figure 2.11: Decision circuit based on the maximum likelihood (ML) rule for estimating the received symbol.
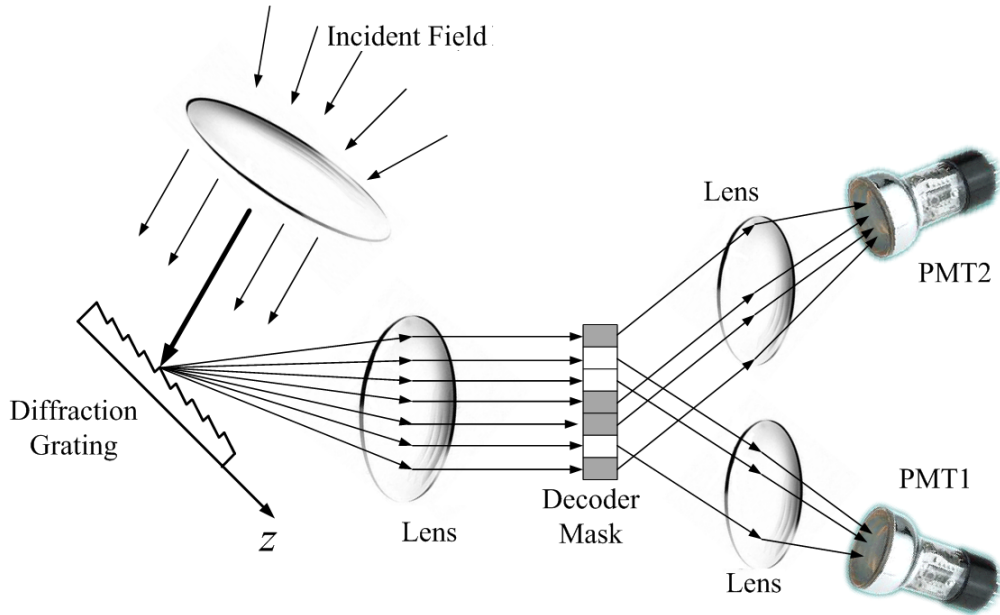
Figure 2.12: Receiver structure for the UV system using two PMTs.

A decoder mask, composed of Q elements, is placed after the diffraction grating to decode the received signal. As shown in Figure 2.12, we assign the z-axis perpendicular to the grooves of the grating.

According to the receiver structure in Figure 2.12, the diffraction grating reflects each wavelength with a specific angle. Thus, divergence of the received beam in the z direction causes the signal of one wavelength to be reflected at a wider angle, causing interference between adjacent wavelengths. As a result, each point in the decoder mask plane receives power from more than one wavelength. This can be interpreted as a transformation of the divergence from the received beam angle into the wavelength domain after the diffraction grating. We denote this effect as spatial broadening, which looks like spectral broadening and causes interference between adjacent spectral bins, as illustrated in Figure 2.13.

We assume that the normalized optical power distribution on the decoder mask plane at point z from wavelength q is denoted by $g(z - z_q)$, where z_q is the center of the bin q, and $z - z_q$ is the distance from the center of the beam, assumed centered on the qth mask element. Furthermore, we assume that $g(z - z_q)$ is the same for all wavelengths. To describe this effect, we define the spatial broadening coefficients as

$$a_i = \frac{1}{\int_{-\infty}^{\infty} g(z)dz} \int_{\frac{2i-1}{2}\Delta L}^{\frac{2i+1}{2}\Delta L} g(z)dz, \tag{2.17}$$

where ΔL is the width of one element of the decoder mask. These spatial broadening coefficients capture the interference that the optical signal in one wavelength bin introduces on its neighboring bins. We define the extent of spatial broadening by the integer Z such that $\sum_{i=-Z}^{Z} a_i = 1$ and $a_i \approx 0$ for $\forall |i| > Z$.

Because of this spatial broadening, the optical power reflected from the diffraction grating in the angle that correspond to the wavelength q can be written as

$$\widetilde{p}_R^{(q)}(t) = \sum_{i=-Z}^{Z} a_i p_R^{(q-i)}(t). \tag{2.18}$$

According to (2.17), the a_i's are functions of $\Delta L = L/Q$, where L is the length of the decoder mask and is assumed to be fixed. As the code length, Q, increases, ΔL decreases and, consequently, Z increases. Thus, by increasing Q the interference between the spectral bins worsens.

2.4.2 Decision Variables

In order to capture as much of the received light as possible to decode the spectrally encoded signal, the decoder mask is a switch that modifies the beam's direction of propagation in each element, unlike the amplitude (on-off) encoder mask used at the transmitter. The elements can
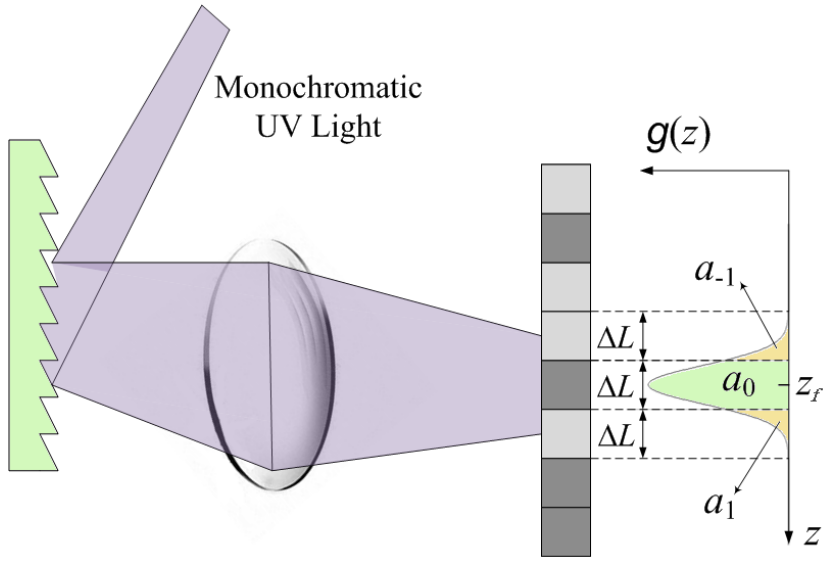
Figure 2.13: Effect of spatial broadening, due to the received beam divergence, on the interference between wavelengths after the diffraction grating.

either be micro-electro-mechanical-system (MEMS)-based mirrors with UV coating, or electro-optic crystals, such as BBO or LBO, which are transparent in the UV range. Each element can be in one of two different states, named u_1 and u_2, and its state can be changed between u_1 and u_2. By changing the state of each element, the beam of the corresponding wavelength can be directed
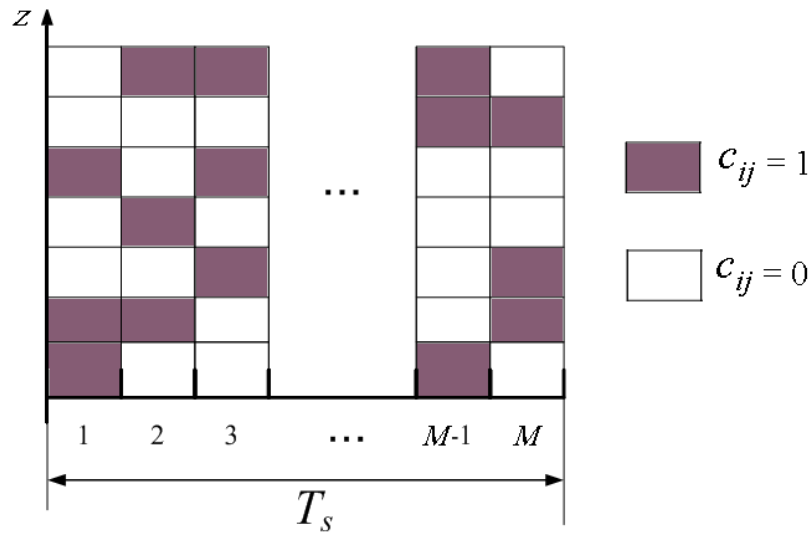
Figure 2.14: The variation of the spectral decoder mask in one symbol period.
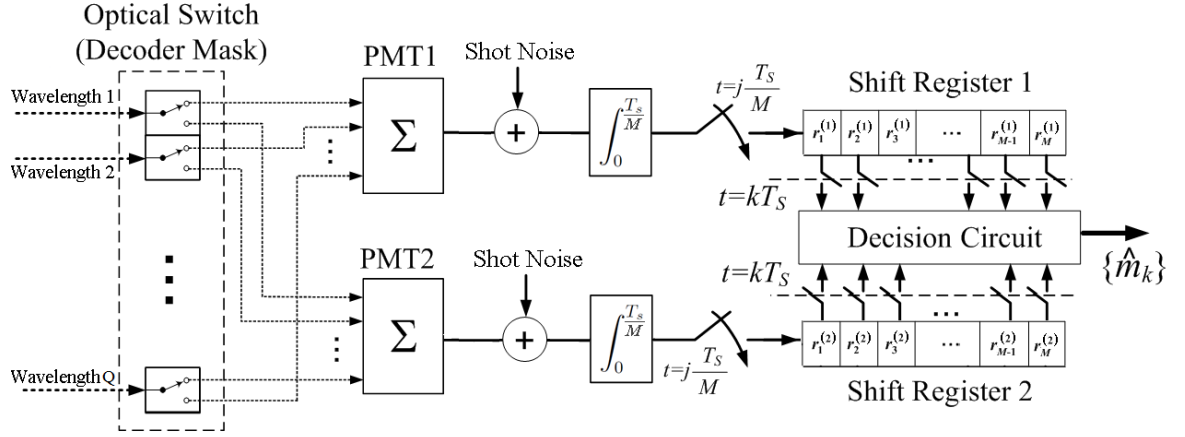
Figure 2.15: Schematic illustration of the receiver, showing the decoder mask, PMTs and decision circuit for symbol $k = 0$. Light paths are indicated by dotted lines and electrical paths are indicated by solid lines.

to one of the two PMTs. The states of the elements of the decoder mask are determined by the codeword that the decoder controller sends to the mask.

As illustrated in Figure 2.14, each symbol period with duration T_s is divided into M equal time slots and the decoder mask is changed in each time slot. Without loss of generality, we consider that the decoder mask matches the mth codeword in the mth time slot. The state of element j of the decoder mask is u_1 in the mth time slot if $c_{mj} = 1$ and is u_2 otherwise. Because of the non-rectangular temporal shape of the received pulse [19], the received energies in the time slots of one symbol period are not equal. Therefore, an interleaver is used to reorder the codes in the decoder mask, so that the average error probability becomes equal for all symbols.

A schematic of the receiver is shown in Figure 2.15. According to (2.18) and the decoder function, the incident signal in wavelength q and time slot j upon PMT1 is $c_{jq}\widetilde{p}_R^{(q)}(t)$ and upon PMT2 is $(1 - c_{jq})\widetilde{p}_R^{(q)}(t)$.

We denote the current generated by PMT1 and PMT2 as $I^{(1)}(t)$ and $I^{(2)}(t)$, and the additive noise at PMT1 and PMT2 as $\nu^{(1)}(t)$ and $\nu^{(2)}(t)$, respectively. Without loss of generality we consider the $k = 0$ symbol time. Let $I_j^{(n)}(t)$ and $\nu_j^{(n)}(t)$ respectively represent $I^{(n)}(t)$ and $\nu^{(n)}(t)$ in time slot j of symbol period $k = 0$, for $n = 1, 2$. Then according to [32], $I_j^{(n)}(t)$ is given by

$$I_j^{(n)}(t) = GR \sum_{q=1}^{Q} \Big((n-1) - (-1)^n c_{jq}\Big)\widetilde{p}_R^{(q)}(t) + \nu_j^{(n)}(t), \quad \frac{(j-1)T_s}{M} \leq t < \frac{jT_s}{M}, \quad (2.19)$$

27

where $n = 1, 2$, $j = 1, 2, \ldots, M$, G is the gain and R is the responsivity of the PMTs.

An integrate-and-dump filter and a sampler are placed after each PMT, and a shift register of length M stores the output samples of all time slots. We represent the stored variables by vector $\mathbf{r}^{(n)} = (r_1^{(n)}, r_2^{(n)}, \ldots, r_M^{(n)})$, $n = 1, 2$, where $r_j^{(n)}$ is

$$r_j^{(n)} = \int_{\frac{j-1}{M}T_s}^{\frac{j}{M}T_s} I_j^{(n)}(t)dt. \tag{2.20}$$

Using (2.1), (2.18) and (2.19), $r_j^{(n)}$ becomes

$$r_j^{(n)} = \Bigg[\sum_{i=-Z}^{Z} GRa_i \sum_{q=1+\frac{i+|i|}{2}}^{Q+\frac{i-|i|}{2}} \Big((n-1) - (-1)^n c_{jq} \Big) \times$$
$$\Bigg(\sum_{m=-\infty}^{\infty} s_{m(q-i)} \int_{\frac{j-1}{M}T_s}^{\frac{j}{M}T_s} \Big[\mathcal{F}_q(t - mT_s) * h_q(t) \Big] dt \Bigg) \Bigg]$$
$$+ \int_{\frac{j-1}{M}T_s}^{\frac{j}{M}T_s} \Big[\nu_j^{(n)}(t) \Big] dt. \tag{2.21}$$

As mentioned above, an interleaver is used to change the order of the codewords of the decoder mask in each symbol period; therefore, for mathematical simplicity, we replace the term $\int_{\frac{j-1}{M}T_s}^{\frac{j}{M}T_s} \big[\mathcal{F}_q(t - mT_s) * h_q(t) \big] dt$ in (2.21) with its mean, $\frac{1}{M} \int_0^{T_s} \big[\mathcal{F}_q(t - mT_s) * h_q(t) \big] dt$. Here, $\int_{\frac{j-1}{M}T_s}^{\frac{j}{M}T_s} \big[\mathcal{F}_q(t - mT_s) * h_q(t) \big] dt$ is the part of the optical energy transmitted in wavelength q of symbol time m and received during time slot j of the symbol at time $k = 0$.

Again for mathematical simplicity, we assume that the received pulse shape, i.e., $\mathcal{F}_q(t) * h_q(t)$, is the same for all wavelengths. We define the ISI coefficients, γ_m, as

$$\gamma_m = \int_0^{T_s} \big[\mathcal{F}_q(t - mT_s) * h_q(t) \big] dt, \qquad -N_s \leq m \leq N_s, \tag{2.22}$$

where $2N_s$ is the number of adjacent symbols influencing the desired symbol, i.e., $\gamma_i \approx 0$ for $\forall |i| > N_s$. Using (2.22), (2.21) becomes

$$r_j^{(n)} = GR \sum_{i=-Z}^{Z} a_i \Bigg(\sum_{m=-N_s}^{N_s} \Big(K(n-1) - (-1)^n \mathcal{S}(\mathbf{s}_m, i) \mathbf{c}_j^{\mathsf{T}} \Big) \frac{\gamma_m}{M} \Bigg) + \int_{\frac{j-1}{M}T_s}^{\frac{j}{M}T_s} \nu_j^{(n)}(t)dt, \tag{2.23}$$

where $\mathcal{S}(\mathbf{s}_m, i)$ is the ith right shift of vector $\mathbf{s}_m$. One last approximation we make for analytical tractability is to overestimate the spatial interference on $\mathbf{s}_m$ by using *cyclic* right shifts of $\mathbf{s}_m$ instead of *linear* right shifts. For the remainder of this dissertation, $\mathcal{S}(\mathbf{y}, i)$ denotes the ith cyclic shift of vector $\mathbf{y}$.

The mean of $r_j^{(1)}$, neglecting ISI, is given by

$$\mu_j^{(1)} = GR\frac{\gamma_0}{M}\sum_{i=-Z}^{Z} a_i \mathcal{S}(\mathbf{s}_0, i)\mathbf{c}_j^{\mathrm{T}}. \qquad (2.24)$$

Let m_k and $\hat{m}_k$ be the transmitted and estimated symbols in the kth symbol period, respectively. We define $\mu_j^{(1)}$ given $m_0 = \ell$ as $\mu_j^{(1|\ell)} = GR\frac{\gamma_0}{M}\sum_{i=-Z}^{Z} a_i\big(\mathcal{S}(\mathbf{c}_\ell, i)\mathbf{c}_j^{\mathrm{T}}\big)$. Since the code is cyclic, we have $\boldsymbol{\mu}^{(1|\ell)} = \mathcal{S}(\boldsymbol{\mu}^{(1|1)}, \ell - 1)$, for $\forall\ell$, where the vector $\boldsymbol{\mu}^{(1|\ell)} = [\mu_1^{(1|\ell)}, \mu_2^{(1|\ell)}, \ldots, \mu_M^{(1|\ell)}]$, $\ell = 1, 2, \ldots, F$. From the receiver structure, letting $\mu_j^{(2|\ell)}$ be the mean of $r_j^{(2)}$ given $m_0 = \ell$, we know $\mu_j^{(1|\ell)} + \mu_j^{(2|\ell)} = GR\frac{\gamma_0}{M}w$; henceforth we use $GR\frac{\gamma_0}{M}w - \mu_j^{(1|\ell)}$ instead of $\mu_j^{(2|\ell)}$.

Because of the high gain of the PMTs, shot noise dominates the thermal noise and, thus, the variance of $r_j^{(n)}$ in (2.23) given $m_0 = \ell$, neglecting other noise sources, can be approximated as

$$\mathrm{Var}\big(r_j^{(n)}|\ell\big) = 2e\Delta\upsilon G\mu_j^{(n|\ell)}, \qquad (2.25)$$

where e is the electron charge ($e = 1.6 \times 10^{-19}$ C) and $\Delta\upsilon$ is the receiver equivalent noise bandwidth. Since in the receiver structure the symbol period is divided into M equal time slots, $\Delta\upsilon$ is proportional to M and increases as M increases. In this study we assume the shot noise can be modeled as Gaussian distributed [33].

2.4.3 Symbol Detectors

At the end of the symbol period, the stored variables in the shift registers are fed into a symbol-by-symbol demodulator, which then estimates the symbol $\hat{m}_k$ for the kth time instant (ignoring ISI). Three different decision rules are considered:

A. Optimum Single-PMT Detector

In this case the decision is made based on a maximum likelihood (ML) rule using only the output of either PMT1 or PMT2. This is the simplest and least expensive option. The decision criterion for this detector can be written as

$$\hat{m}_0 = \arg\max_{1 \le \ell \le M} \Pr(\mathbf{r}^{(n)}|m_0 = \ell), \qquad (2.26)$$

where $n = 1$ or 2, m_0 is the symbol transmitted in the $k = 0$ symbol period and $\Pr(\mathbf{r}^{(n)}|m_0 = \ell)$ is the probability of receiving vector $\mathbf{r}^{(n)}$, given $m_0 = \ell$.

B. Optimum Dual-PMT Detector

Given equally-likely transmitted symbols, the optimum detector can be implemented based on a ML rule using the outputs of both PMT1 and PMT2. For this detector, since the shot noise components in different time-slots have unequal powers, the decision rule in its most simple form is quadratic. Since the noise terms of PMT1 and PMT2 are independent, the decision criterion for this case can be written

$$\hat{m}_0 = \arg \max_{1 \le \ell \le M} \Pr(\mathbf{r}^{(1)} | m_0 = \ell) \Pr(\mathbf{r}^{(2)} | m_0 = \ell). \tag{2.27}$$

C. Optimum Linear Dual-PMT Detector

In linear detectors, the decision statistic, written as a vector $\mathbf{x} = [x_1, x_2, \ldots, x_M]$, is generated from $\mathbf{r}^{(1)}$ and $\mathbf{r}^{(2)}$ as

$$\mathbf{x} = \mathbf{r}^{(1)} \boldsymbol{F} + \mathbf{r}^{(2)} \boldsymbol{F}', \tag{2.28}$$

where $\boldsymbol{F} = [\boldsymbol{f}_1 \ \boldsymbol{f}_2 \ \ldots \ \boldsymbol{f}_M]$ and $\boldsymbol{F}' = [\boldsymbol{f}'_1 \ \boldsymbol{f}'_2 \ \ldots \ \boldsymbol{f}'_M]$ are $M \times M$ matrices, formed by columns $\boldsymbol{f}_\ell = [f_{1\ell} \ f_{2\ell} \ \ldots \ f_{M\ell}]^{\mathrm{T}}$ and $\boldsymbol{f}'_\ell = [f'_{1\ell} \ f'_{2\ell} \ \ldots \ f'_{M\ell}]^{\mathrm{T}}$. Then the decision is made based on the following rule:

$$\hat{m}_0 = \arg \max_{1 \le \ell \le M} x_\ell. \tag{2.29}$$

For the optimal linear detector, $\boldsymbol{F}$ and $\boldsymbol{F}'$ are chosen to minimize the symbol error probability.

Note that if $a_0 = 1$ and $a_i = 0$ for $i \neq 0$, the three detectors described (the optimum dual-PMT detector, optimum linear dual-PMT detector and optimum single-PMT detector using PMT2) all reduce to

$$\hat{m}_0 = \arg \min_{1 \le \ell \le M} r^{(2)}_\ell. \tag{2.30}$$

Since the performance of these detectors is not a function of the Hamming distances between the symbols, the fixed weight and fixed cross-correlation code families proposed here, may not be the optimum codes, i.e., those that have the best performance. Finding the optimum codes for each one of these detectors is beyond the scope of this dissertation.

2.5 Analytical Bit Error Probability Calculation

In this section, we calculate the optimum $\boldsymbol{F}$ and $\boldsymbol{F}'$ of the linear dual-PMT detector, and obtain expressions for the bit error probability of this receiver by considering the shot noise, temporal dispersion and spatial broadening effects. As shown below in Section 2.6, the symbol error rate of the linear dual-PMT detector is close to the error rate of the quadratic optimal dual-PMT detector, and acts as a bound on its performance. Therefore, and for mathematical simplicity, we analyze the bit error probability of only the linear dual-PMT detector in this section.

2.5.1 Optimal Linear Dual-PMT Detector for ISI-Free System

Generally, the symbol error probability can be written as

$$\mathrm{P}_s = \sum_{\ell=1}^{M} \Pr(m_0 = \ell)(1 - \Pr(\ell|\ell)). \tag{2.31}$$

where we define $\Pr(\ell'|\ell) \doteq \Pr(\hat{m}_0 = \ell'|m_0 = \ell)$. Assuming the decision criterion to be as (2.29), an error arises if for at least one ℓ' ($\ell' \neq \ell$) we have $x_{\ell'} > x_\ell$, and therefore, $\Pr(\ell'|\ell) = \Pr(x_{\ell'} > x_\ell|m_0 = \ell)$. The output samples in Figure 2.15 at time slot j are modeled as Gaussian distributed, and denoted as $r_j^{(n)} \sim \mathcal{N}\big(\mu_j^{(n|\ell)}, \mathrm{Var}(r_j^{(n)}|\ell)\big)$. Thus, $x_\ell - x_{\ell'}$ is also a Gaussian random variable with mean $\mu_{(\ell-\ell')} = \sum_{j=1}^{M} \mu_j^{(1|\ell)}(f_{j\ell} - f_{j\ell'}) + \mu_j^{(2|\ell)}(f'_{j\ell} - f'_{j\ell'})$ and variance $\mathrm{Var}_{(\ell-\ell')} = \sum_{j=1}^{M} \mathrm{Var}(r_j^{(1)}|\ell)(f_{j\ell} - f_{j\ell'})^2 + \mathrm{Var}(r_j^{(2)}|\ell)(f'_{j\ell} - f'_{j\ell'})^2$. Then

$$\Pr(\ell'|\ell) = \frac{1}{2}\,\mathrm{erfc}\Big(\frac{\mu_{(\ell-\ell')}}{\sqrt{2\mathrm{Var}_{(\ell-\ell')}}}\Big). \tag{2.32}$$

Let $\boldsymbol{F}^*$ and $\boldsymbol{F}'^*$ be the solutions of the optimum detector in the ISI-free case. Since the symbols are cyclic shifts, $\boldsymbol{F}^*$ and $\boldsymbol{F}'^*$ are circulant matrices, so $\boldsymbol{f}_\ell^* = \mathcal{S}(\boldsymbol{f}_1^*, \ell-1)$ and $\boldsymbol{f}'^*_\ell = \mathcal{S}(\boldsymbol{f}'^*_1, \ell-1)$, for $\forall \ell$. Therefore, $\Pr(\ell'|\ell)$, using (2.25), becomes

$$\Pr(\ell'|\ell) = \frac{1}{2}\mathrm{erfc}\left(\sqrt{\frac{1}{4e\Delta vG}} \frac{\boldsymbol{\mu}^{(1|\ell)}\big(\boldsymbol{f}_\ell^* - \boldsymbol{f}_{\ell'}^*\big) - \boldsymbol{\mu}^{(1|\ell)}\big(\boldsymbol{f}'^*_\ell - \boldsymbol{f}'^*_{\ell'}\big)}{\sqrt{\boldsymbol{\mu}^{(1|\ell)}\widetilde{\boldsymbol{F}}_{\ell,\ell'} + \big(GRw\frac{\gamma_0}{M} - \boldsymbol{\mu}^{(1|\ell)}\big)\widetilde{\boldsymbol{F}}'_{\ell,\ell'}}} \right), \tag{2.33}$$

where $\widetilde{\boldsymbol{F}}'_{\ell,\ell'} = \big[(f_{j\ell}^* - f_{j\ell'}^*)^2\big]_{j=1}^{M}$ and $\widetilde{\boldsymbol{F}}_{\ell,\ell'} = \big[(f'^*_{j\ell} - f'^*_{j\ell'})^2\big]_{j=1}^{M}$ are $M \times 1$ matrices. According to (2.32), adding a constant value to all $f_{j\ell}$'s or $f'_{j\ell}$'s does not change $\Pr(\ell'|\ell)$. On the other hand, for the optimum linear detector $f_{i\ell}^* = f_{j\ell}^*$ and $f'^*_{i\ell} = f'^*_{j\ell}$ if $\mu_i^{(n|\ell)} = \mu_j^{(n|\ell)}$. So, without loss of generality, for time slots j such that $\mu_j^{(n|\ell)} = GR\frac{\gamma_0}{M}\lambda$, $f_{j\ell}^*$ and $f'^*_{j\ell}$ are chosen to be zero.

31

The union bound on the symbol error probability is given by

$$P_{s,UB} = \sum_{\ell=1}^{M} \sum_{\substack{\ell'=1 \\ \ell' \neq \ell}}^{M} \frac{1}{M} \Pr(\ell'|\ell). \qquad (2.34)$$

Since the symbols and the channel action (after interleaving) are symmetric, (2.34) can be simplified to

$$P_{s,UB} = \sum_{\ell'=2}^{M} \Pr(\ell'|1). \qquad (2.35)$$

For high SNRs the largest $\Pr(\ell'|1)$ becomes the dominant term. So, minimizing the maximum $\Pr(l'|1)$, over $2 \leq l' \leq M$, asymptotically minimizes the symbol error probability. Consequently, the solution to the following minimax problem gives us the $\boldsymbol{F}^*$ and $\boldsymbol{F'}^*$ of the asymptotically optimum linear detector:

$$(\boldsymbol{F}^*, \boldsymbol{F'}^*) = \arg\min_{\boldsymbol{F}, \boldsymbol{F'}} \max_{2 \leq \ell' \leq M} \Pr(\ell'|1). \qquad (2.36)$$

In general, (2.36) is not an easy problem to solve. Here, we restrict ourselves to a specific case, which is valid for most practical systems. We assume that the spatial broadening is small enough to neglect a_i for $|i| \geq 2$, i.e., the only nonzero a_i's are a_0, a_{-1} and a_1. We also assume that the spatial broadening is symmetric, i.e., $a_1 = a_{-1}$, and therefore, we have $a_0 + 2a_1 = 1$. In this case, since $\mu_j^{(1|1)} = GR\frac{\gamma_0}{M}\lambda$, for $j = 3, 4, \ldots, M-1$, $f_{j1}^* = f_{j1}'^* = 0$ for $j = 3, 4, \ldots, M-1$. We also have $\mu_1^{(1|1)} = GR\frac{\gamma_0}{M}(a_0 K + 2a_1\lambda)$ and $\mu_2^{(1|1)} = \mu_M^{(1|1)} = GR\frac{\gamma_0}{M}(a_1 K + (a_0 + a_1)\lambda)$, and thus, $f_{21}^* = f_{M1}^*$ and $f_{21}'^* = f_{M1}'^*$. Hence, (2.33) becomes as

$$\Pr(\ell'|1) = \begin{cases} \frac{1}{2}\mathrm{erfc}\left(\sqrt{\frac{R\gamma_0}{4e\Delta\upsilon M}} \frac{(f_{11}^*-f_{21}^*)\zeta_1 + f_{21}^*\zeta_2 - (f'^*_{11}-f'^*_{21})\zeta_1 - f'^*_{21}\zeta_2}{\sqrt{(f_{11}^*-f_{21}^*)^2\xi_1 + f_{21}^{*2}\xi_2 + (f'^*_{11}-f'^*_{21})^2(2K-\xi_1) + f'^{*2}_{21}(2K-\xi_2)}}\right), & \ell'=2, M; \\[3ex] \frac{1}{2}\mathrm{erfc}\left(\sqrt{\frac{R\gamma_0}{4e\Delta\upsilon M}} \frac{f_{11}^*\zeta_3 + f_{21}^*\zeta_2 - f'^*_{11}\zeta_3 - f'^*_{21}\zeta_2}{\sqrt{f_1^{*2}\xi_3 + f_{21}^{*2}\xi_2 + f'^{*2}_{11}(2K-\xi_3) + f'^{*2}_{21}(2K-\xi_2)}}\right), & \ell'=3, M-1; \\[3ex] \frac{1}{2}\mathrm{erfc}\left(\sqrt{\frac{R\gamma_0}{4e\Delta\upsilon M}} \frac{f_{11}^*\zeta_3 + 2f_{21}^*\zeta_2 - f'^*_{11}\zeta_3 - 2f'^*_{21}\zeta_2}{\sqrt{f_{11}^{*2}\xi_3 + 2f_{21}^{*2}\xi_2 + f'^{*2}_{11}(2K-\xi_3) + 2f'^{*2}_{21}(2K-\xi_2)}}\right), & \text{otherwise.} \end{cases} \qquad (2.37)$$

where $\zeta_1 = (a_0 - a_1)(K - \lambda)$, $\zeta_2 = a_1(K - \lambda)$, $\zeta_3 = a_0(K - \lambda)$, $\xi_1 = (1-a_1)K + (1+a_1)\lambda$, $\xi_2 = a_1 K + (2-a_1)\lambda$, and $\xi_3 = a_0 K + (2-a_0)\lambda$.

From Appendix 2.A at the end of this chapter, the minimum of $\Pr(2|1) = \Pr(M|1)$ over all $\boldsymbol{F}$ and $\boldsymbol{F'}$ is

$$\frac{1}{2}\mathrm{erfc}\left(\sqrt{\frac{KR\gamma_0}{2e\Delta\upsilon}}\sqrt{\frac{\zeta_1^2}{\xi_1(2K-\xi_1)} + \frac{\zeta_2^2}{\xi_2(2K-\xi_2)}}\right), \qquad (2.38)$$

32

which is obtained for $f_{11}^* = \frac{\zeta_1}{\xi_1} + \frac{\zeta_2}{\xi_2}$ and $f_{21}^* = \frac{\zeta_2}{\xi_2}$. Substituting these values in (2.37) we get $\Pr(2|1) \geq \Pr(\ell'|1)$ for $3 \leq \ell' \leq M - 1$. For any other f_{11}, f_{21}, f'_{11} and f'_{21}, $\max\limits_{2 \leq \ell' \leq M} \Pr(\ell'|1)$ is larger than (2.38) and thus, (2.38) is the solution of the minimax problem in (2.36).

2.5.2 Symbol Error Probability

To calculate the bit error probability in the presence of ISI, first we obtain an upper bound on the *symbol* error probability and then we calculate a bound on the bit error probability. We assume the detector used is the optimal linear detector ignoring ISI derived above. For the upper bound, we use the union bound in (2.35), where $\Pr(\ell'|1)$, considering ISI, becomes

$$
\Pr(\ell'|1) = \frac{1}{2} \left(\frac{1}{M} \right)^{2N_s} \sum_{m_{-N_s}=1}^{M} \cdots \sum_{m_{-1}=1}^{M} \sum_{m_1=1}^{M} \cdots \sum_{m_K=1}^{M}
$$

$$
\mathrm{erfc}\left(\sqrt{\frac{1}{4e\Delta\upsilon G}} \frac{\left(\sum\limits_{i=-N_s}^{N_s} \frac{\gamma_i}{\gamma_0} \boldsymbol{\mu}^{(1|m_i-1)} \right) \left[(\boldsymbol{f}_1^* - \boldsymbol{f}_{\ell'}^*) - (\boldsymbol{f'}_1^* - \boldsymbol{f'}_{\ell'}^*) \right]}{\sqrt{\left(\sum\limits_{i=-N_s}^{N_s} \frac{\gamma_i}{\gamma_0} \boldsymbol{\mu}^{(1|m_i-1)} \right) \left(\widetilde{\boldsymbol{F}}_{1,\ell'} - \widetilde{\boldsymbol{F}}'_{1,\ell'} \right) + \left(GR\frac{K}{M} \sum\limits_{i=-N_s}^{N_s} \gamma_i \right) \left\| \boldsymbol{f'}_1^* - \boldsymbol{f'}_{\ell'}^* \right\|^2}} \right).
$$

$$(2.39)$$

2.5.3 Bit Error Probability

Having bounded the symbol error probability, we still need the bit error probability in order to be able to compare the system performance with OOK systems. Assume $\boldsymbol{b}_\ell$, a $\log_2 M$ digit binary number, is the binary sequence assigned to symbol ℓ. When $m_0 = \ell$ is transmitted and $\hat{m}_0 = \ell'$ is received, $d(\boldsymbol{b}_\ell, \boldsymbol{b}_{\ell'})$ bits are decoded incorrectly, where $d(\boldsymbol{b}_\ell, \boldsymbol{b}_{\ell'})$ denotes the Hamming distance between the binary vectors $\boldsymbol{b}_\ell$ and $\boldsymbol{b}_{\ell'}$. According to [34], for equally likely symbols we have the following inequality for the bit error probability, P_b,

$$
\mathrm{P}_b \leq \frac{M}{2(M-1)} \mathrm{P}_{s,UB} \doteq \mathrm{P}_{b,UB}, \tag{2.40}
$$

where $\mathrm{P}_{b,UB}$ is an upper bound on P_b.

2.6 Numerical Results

In this section, numerical results are presented to compare the performance of the proposed M-ary transmission for different code-lengths with previously proposed OOK modulation. In this work, the main limiting factor on the bit-rate is inter-symbol interference, and other pulsed modulations,
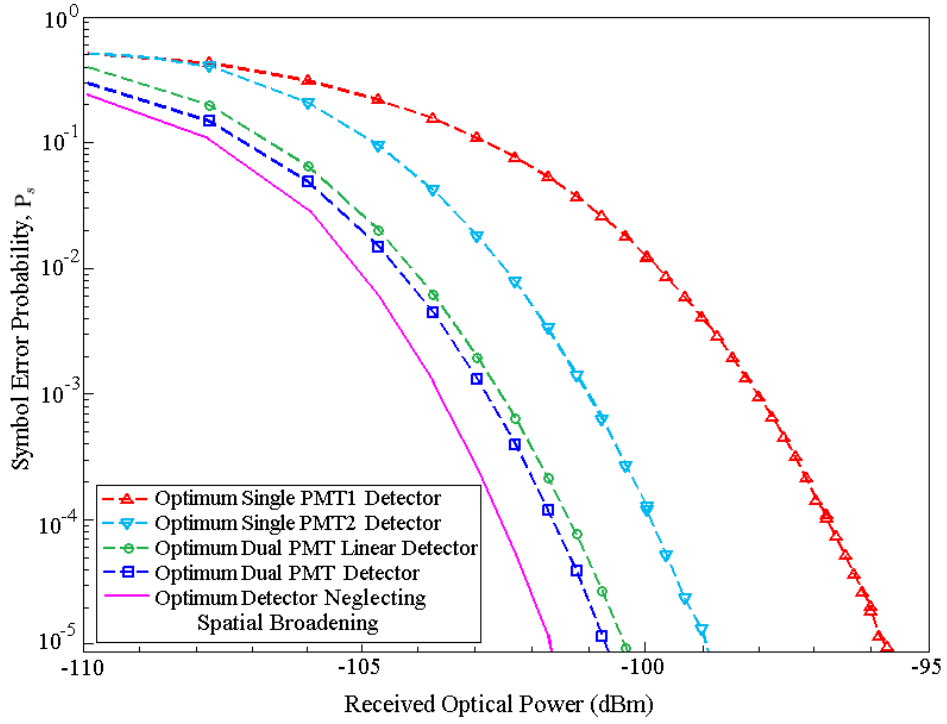
Figure 2.16: Simulated symbol error probability, P_s, versus the received power for OOK and M-ary SAC using an optimum dual PMT detector, optimum single PMT1 detector, optimum single PMT2 detector, optimum linear detector and optimum detector neglecting spatial broadening for case A and Q=23.

such as PPM, perform much worse than OOK, because of their short pulse duration. Hence, in our numerical results we only compare the performance with OOK.

We use Paley, projective geometry (PG) and twin prime power (TPP) difference sets [1] as

Table 2.1: Parameters of three different geometries

	Case A	Case B	Case C
θ_1	75°	60°	40°
θ_2	45°	60°	40°
ϕ_1	10°	2°	5°
ϕ_2	50°	50°	50°
D	400 m	400 m	400 m
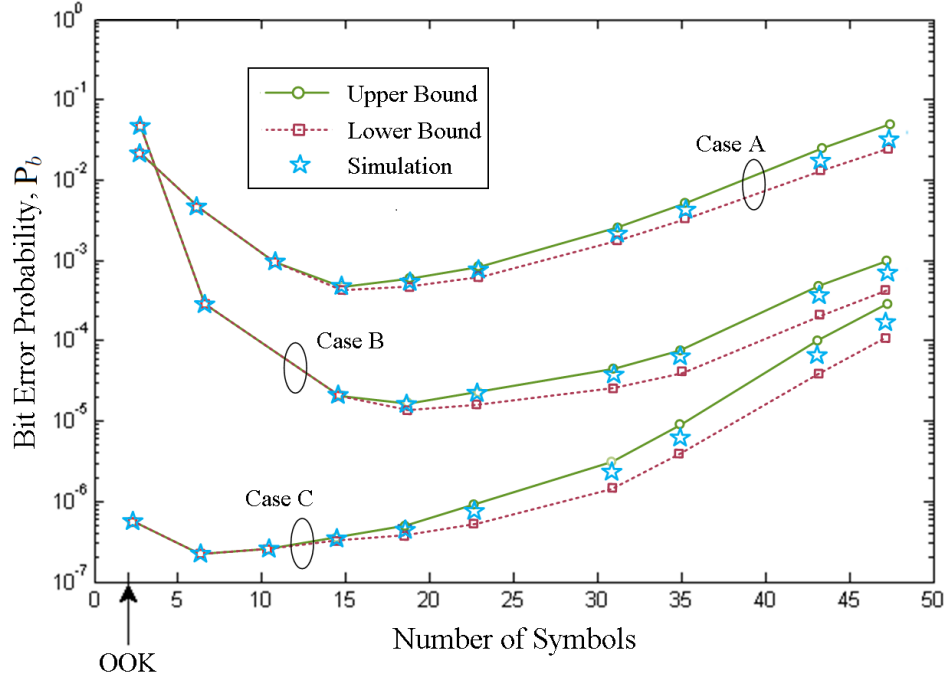
Figure 2.17: P_b of the optimum linear dual-PMT detector versus the code length, Q, for cases A, B and C defined in Table 2.1.

code families in these results. For these code families $Q = 2K + 1$ and $K = 2\lambda + 1$. For the bit-symbol mapping, since the code-lengths are in general not powers of two, we concatenate multiple symbols and assign longer binary sequences to them [35]. The transmitted power is assumed to be 1 W. The gain G of the PMTs is 10^7 and their responsivity R is 0.3 A/W. Three geometries are considered, described in Table 2.1.

For simplicity, the transmitted signal is assumed to have a rectangular pulse shape in time, and the received pulse is obtained by convolving the transmitted signal with the impulse response of the channel, where the impulse response is computed using the numerical integration approach, presented in [14]. In addition, the spatial distribution of the transmitted beam is assumed to be a Gaussian function.

Figure 2.16 compares the symbol error probability of different detectors using simulation results. These results are for case A in Table 2.1 and for $Q = 23$. For these system parameters, $a_0 = 0.78$ and $a_1 = a_{-1} = 0.11$. The simulation result for the optimum detector neglecting spatial broadening, in (2.30), is also plotted. According to these results, for this code the optimum single detector using PMT2 has a better performance compared to the same detector using PMT1.

This means that for the optimum single detector, the lowest error probability is achieved when the decoder mask matches the complements of the codewords. OOK using a single-PMT results in an error rate between the two. The difference between the error rates of the optimum single-PMT2 detector and the optimum dual-PMT detector shows the performance price that is paid for having one PMT instead of two. The performance of the optimum linear dual-PMT detector is close to that of the optimum dual-PMT detector, and since it has a lower complexity, we prefer to use this detector in the receiver. Henceforth all results assume this detector, and assume that similar conclusions hold if another detector is chosen.

Figure 2.17 shows the P_b versus the code length, Q, for the three physical geometries in Table 2.1. The analytical results of the upper bounds are compared with simulation results. The bit-rate is assumed to be fixed for all code lengths ($R_b = 1$ Mb/s). For small Q's, ISI is the main limiting factor on system performance. For a fixed bit rate, however, by increasing the number
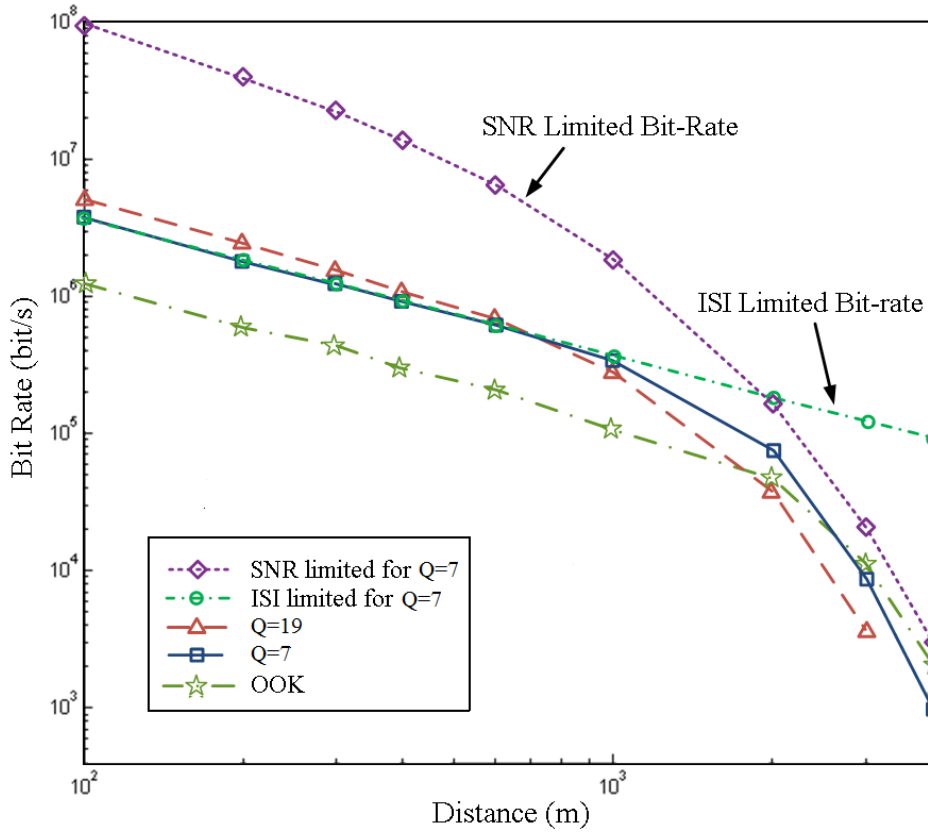
Figure 2.18: Maximum attainable bit-rate versus distance for Q=7 and comparison to the ISI and SNR limited bit-rates, assuming case B for a $P_b = 3 \times 10^{-5}$.
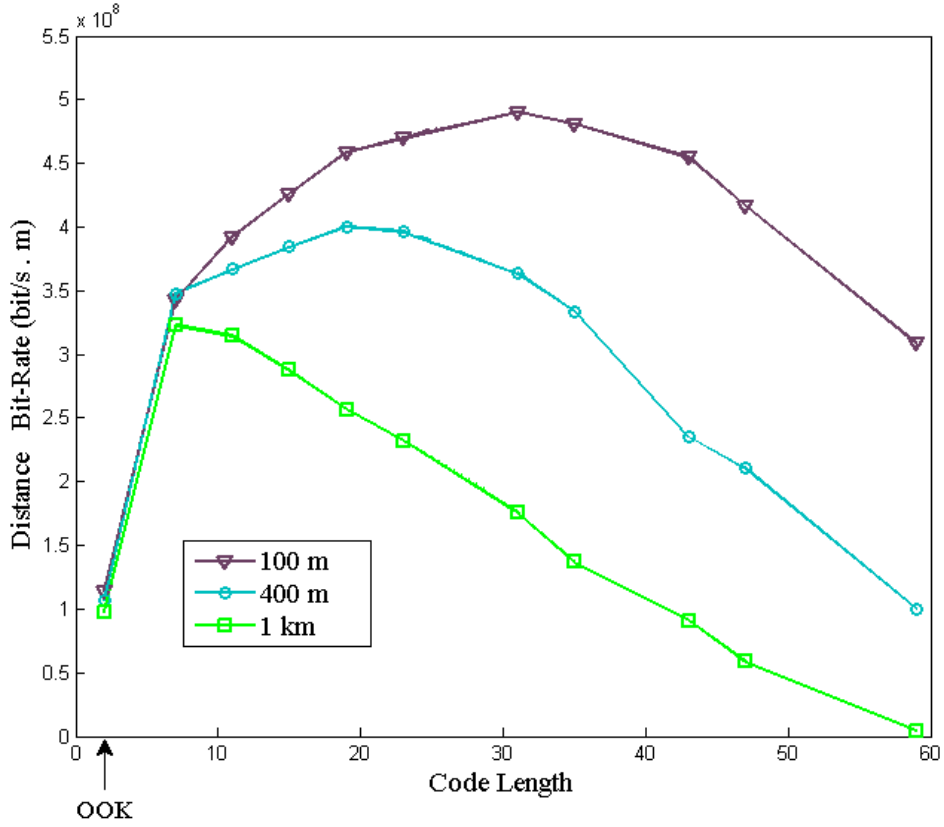
Figure 2.19: Maximum attainable distance bit-rate product for a $P_b = 3 \times 10^{-5}$ versus the number of symbols, Q, for case B and for $D = 100$ m, $D = 400$ m and $D = 1$ km, with and without spatial dispersion.

of symbols (Q), the symbol rate decreases, and, consequently, the ISI effect is reduced. On the other hand, for large Q's the number of time slots is greater, and, therefore, the optical energy in each time slot is reduced, thus, SNR limits the P_b. In addition, according to Section 2.4, the spatial broadening effect increases by increasing Q and becomes another source of degradation for longer code lengths. Therefore, there is an optimum value for Q considering these three factors.

For low transmitter and receiver inclination angles the optimum modulation is OOK, since the ISI is low for these geometries. In Figure 2.17, for cases A and B, defined in Table I, the ISI limits the P_b and the optimum values of Q are 15 and 19, respectively. In case C, since the elevation angle of both the receiver and the transmitter is small, the impulse response is shorter than the former cases and the ISI effect is smaller. Consequently, the optimum value of Q is 7. Also, according to these results the union bound is notably close to the simulation results and can

be used as a good approximation for the P_b.

The maximum achievable bit rate to sustain a P_b of at most 3×10^{-5} is plotted in Figure 2.18 versus the distance between the transmitter and receiver. The parameters of case B in Table 2.1 are assumed to obtain these results. For this P_b and short distances the bit rate is limited by ISI for every constellation size. By increasing the distance, since the loss increases, the performance becomes limited by the SNR. For small distances, larger Qs are able to achieve higher data rates compared to smaller Q's. But, as the distance increases, the SNR affects the P_b, and the optimum Q decreases. So for long ranges, small Q's or OOK become better choices for data transmission.

The tradeoff between SNR and ISI is also illustrated in Figure 2.18, where we use two bounds to approximate the maximum achievable bit rate: the ISI-limited bit rate, and the SNR-limited bit rate. At short ranges the ISI is the main limiting factor for the maximum bit rate, and the bit rate matches the ISI-limited bound. By increasing the range, the SNR limit becomes smaller than the ISI limit and bounds the maximum bit rate. The ISI limit can be obtained by assuming the ISI is the only limiting factor on the bit rate. In this case the P_b depends only on the ISI coefficients; to have a fixed P_b it is essential to fix these coefficients. As seen in (2.22), the ISI coefficients depend on the impulse response and symbol time, T_s. By increasing the distance, D, the time scale of the impulse response is widened proportionally. Hence, T_s is increased proportionally in order to keep the ISI coefficients constant as well. So the ISI-limited symbol rate and, accordingly, the ISI-limited bit rate decreases inversely proportional to D.

In the SNR limit, P_b depends only on the received energy per symbol. According to [20] the received energy per symbol in NLOS UV links can be approximated as

$$E_s(D) = \frac{\alpha T_s}{D} e^{-\beta D},$$

(2.41)

where α and β depend on the system and geometric parameters. Therefore, for longer ranges, T_s needs to increase exponentially as D increases for a fixed $E_s(D)$.

The maximum distance-rate product is presented in Figure 2.19 in terms of the number of symbols, Q, for $P_b = 3 \times 10^{-5}$. The optimum code length is larger for shorter distances and this maximum distance-rate product increases by decreasing the length of the link. Although for OOK and $Q = 7$ this product is similar over a range of distances, for larger code lengths it varies considerably. This is because for smaller symbol sizes, the distance-rate product stays close to the ISI limit even for long ranges, while for a larger number of symbols it separates from the ISI limit at short distances and then decreases exponentially. Using our SAC system increases the distance-

rate product by a factor varying from 3 to 5 compared to OOK, depending on the transmission distance.

In Figure 2.19 the maximum distance-rate product for the optimum linear dual-PMT detector is also plotted neglecting the spatial broadening. Neglecting the spatial broadening decreases the second term inside the erfc(.) function in (2.38). Thus, for a fixed P_b, we need a smaller γ_0, which is proportional to $E_s(D)$. From (2.41), for a fixed D, decreasing $E_s(D)$ decreases T_s, i.e., increases the data-rate. In other words, by neglecting the spatial broadening we can achieve higher data-rates. According to these results, neglecting the spatial broadening affects the maximum distance rate product for Q's larger than 30, while it has little effect for smaller Q's.

2.7 Summary

In this chapter, an M-ary transmission technique using spectral encoding for application in NLOS UV systems is proposed. Two transmitter structures one using LED arrays and the other using lasers are presented. In the first structure the encoding is done in UV domain, while in the second one the signal is encoded in the visible/IR domain and then wavelength conversion from visible/IR to UV is used. Two receiver structures using APDs and PMTs are proposed. In the first structure Q APDs are deployed to detect the received signal and decode the symbols. In the latter one, a decode mask followed by two PMTs is utilized to decompose the spectral components of the received beam. Cyclic code families are used for encoding the data to simplify transmitter and receiver structures. Several symbol detectors differing in performance and complexity are proposed. An upper bound for evaluating the performance of the system is derived and compared with simulation results. The upper bound closely approximates the bit error probability for various geometries. The maximum achievable data rate for different distances and symbol sizes is calculated, and the data rate is shown to be bounded by ISI and SNR limits. Larger constellation sizes reach higher data rates at short ranges, compared to smaller code lengths. In conclusion, the proposed technique has a better performance compared to OOK for practical link distances and geometries. OOK performs better only for distances longer than 2 km, which results in data rates of around a few kb/s.

Appendix 2.A: Finding Optimal Linear Detector

In this appendix, in order to find the coefficients of the optimal linear detector in (2.36), we obtain the optimum values for $y_1, y_2, \ldots, y_n$ to maximize

$$H_n = \frac{\left[\alpha_1 y_1 + \alpha_2 y_2 + \cdots + \alpha_n y_n\right]^2}{\beta_1 y_1^2 + \beta_2 y_2^2 + \cdots + \beta_n y_n^2}. \tag{2.42}$$

Using mathematical induction, we prove that the maximum of H_n in (2.42) is given by

$$\max_{y_1,\ldots,y_n} H_n = \sum_{i=1}^{n} \frac{\alpha_i^2}{\beta_i},$$

and the solution is $y_i = \frac{\alpha_i \beta_1}{\beta_i \alpha_1} y_1$, $i = 1, 2, \ldots, n$, where y_1 can be any value. For the base step of the induction, we verify this statement for $n = 2$. For $H_2 = (\alpha_1 y_1 + \alpha_2 y_2)^2 / (\beta_1 y_1^2 + \beta_2 y_2^2)$, the maximum is $\frac{\alpha_1^2}{\beta_1} + \frac{\alpha_2^2}{\beta_2}$, and it is obtained for $y_2 = \frac{\alpha_2 \beta_1}{\beta_2 \alpha_1} y_1$.

Our inductive assumption is that the statement is true for $n = m - 1$, and then we prove it is also true for $n = m$. In order to maximize H_m, the partial derivative of H_m with respect to y_m should be zero, i.e., $\frac{\partial H_m}{\partial y_m} = 0$. The solution of this equation is

$$y_m = \frac{\alpha_1}{\beta_1} \frac{(\beta_1 y_1^2 + \beta_2 y_2^2 + \cdots + \beta_{m-1} y_{m-1}^2)}{(\alpha_1 y_1 + \alpha_2 y_2 + \cdots + \alpha_{m-1} y_{m-1})}, \tag{2.43}$$

for which H_m becomes

$$H_m = \frac{\alpha_m^2}{\beta_m} + H_{m-1}, \tag{2.44}$$

where

$$H_{m-1} = \frac{\left[\alpha_1 y_1 + \alpha_2 y_2 + \cdots + \alpha_{m-1} y_{m-1}\right]^2}{\beta_1 y_1^2 + \beta_2 y_2^2 + \cdots + \beta_{m-1} y_{m-1}^2}.$$

By maximizing H_{m-1} we maximize H_m in (2.44). According to the inductive assumption, the maximum of H_{m-1} is

$$\max_{y_1,\ldots,y_{m-1}} H_{m-1} = \sum_{i=1}^{m-1} \frac{\alpha_i^2}{\beta_i},$$

which is obtained for $y_i = \frac{\alpha_i \beta_1}{\beta_i \alpha_1} y_1$, $i = 1, 2, \ldots, m - 1$. Substituting these values in (2.43) and (2.44), we get $y_m = \frac{\alpha_m \beta_1}{\beta_m \alpha_1} y_1$ and

$$\max_{y_1,\ldots,y_m} H_m = \sum_{i=1}^{m} \frac{\alpha_i^2}{\beta_i},$$

and this completes the inductive step. Using these results, (2.38) follows from (2.37).

Chapter 3

Generalizations of Pulse Position Modulation

Pulse position modulation (PPM) is an M-ary technique that can be implemented non-coherently, and is therefore useful in impulse radio (IR) ultra wide band (UWB) radio frequency (RF) systems [36], and in free space optical (FSO) communications [37]. Although on-off keying (OOK) is the conventional binary modulation for FSO and UWB communications, PPM is preferred in systems that have weak ISI effects. The advantage of PPM over OOK is evident in fading channels, since it does not need a threshold to make a decision on the received symbol.

In communication systems with peak power limited transmitters, the transmitted energy per symbol in PPM decreases with increasing symbol size, and this decreases the efficiency. Multipulse PPM (MPPM) has been proposed to solve this problem in FSO systems by transmitting pulses in multiple time-slots [38, 39]. This approach is also helpful in IR UWB systems, in which, for a fixed bit-rate, increasing the alphabet size reduces the average transmitted power [40]. But the complexity in encoding the symbols and mapping bits to symbols prevents MPPM from being widely used [41].

The results of this chapter have appeared in [42], [43] and [44]. In this chapter we focus on the design of new modulation schemes based on BIBD codes for pulsed systems, unlike the spectrally-encoded continuous-wave system described in Chaper 2. These schemes are generalizations of PPM. The organization of this chapter is as follows. PPM is introduced in Section 3.1. In Section 3.2, we propose a new pulse position modulation scheme, called expurgated PPM (EPPM), for application in peak power limited communication systems, such as impulse radio (IR) ultra wide

band (UWB) systems and free space optical (FSO) communications. In Section 3.3, two new modulation schemes using multilevel PPM for application in unipolar optical wireless systems are presented. Section 3.4 introduces coded-QPSK, a new modulation technique for application in RF communication systems.

3.1 Introduction to Pulse Position Modulation

In PPM, the symbol time is divided into Q equal time-slots, only one of which contains a pulse, forming a code with cardinality Q. Hence, as shown in Figure 3.1, for symbol m, one pulse is transmitted in the mth time-chip, and nothing is sent in other time-chips. The symbols of PPM
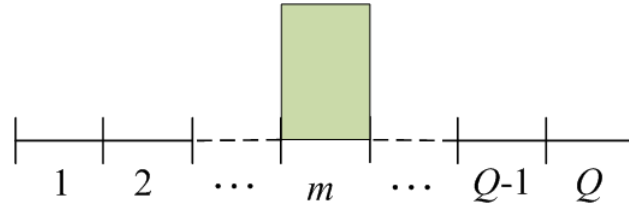
Figure 3.1: Symbol m of a Q-ary PPM.
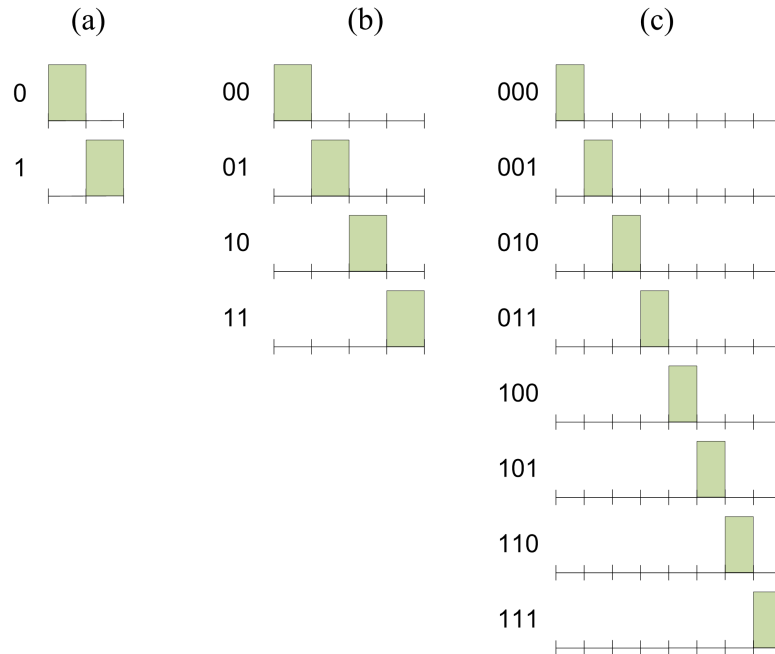
Figure 3.2: Symbols for (a) binary-PPM (BPPM), (b) 4-PPM, and (c) 8-PPM.
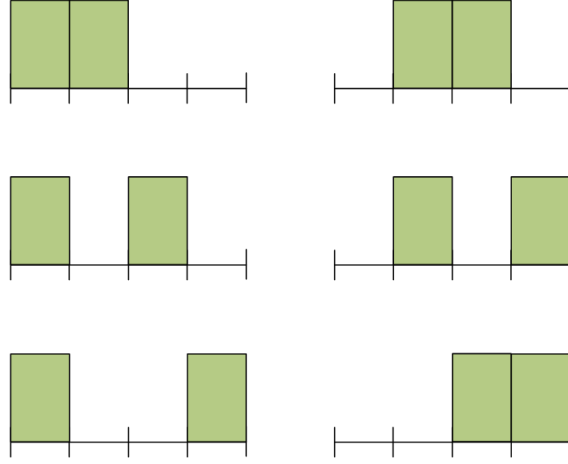
Figure 3.3: Symbols of an MPPM with length 4 and weight 2.

scheme are shown for different constellation sizes in Figure 3.2.

In MPPM, every Q-sequence containing K pulses is considered as a symbol, and so the code cardinality is increased to $\binom{Q}{K}$. Symbols of an MPPM with length 4 and containing two pulses are shown in Figure. 3.3. Yet for a fixed Q the minimum distance between the symbols in MPPM remains the same as for PPM, i.e., it does not increase by increasing K. For large K's the MPPM code size becomes impractically large: the bit-symbol mappings become a problem both at the transmitter and receiver since the complexity grows with the number of symbols.

3.2 Expurgated Pulse Position Modulation

In this section, a new PPM scheme called expurgated PPM (EPPM) using symmetric BIBDs is described. The symbols in this modulation technique are obtained by expurgating the symbols of multipulse PPM. Using the proposed scheme, the constellation size and the bit-rate can be increased significantly in unipolar peak-power limited systems. The symbols are obtained using symmetric balanced incomplete block designs (BIBD), forming a set of pair-wise equidistant symbols. The performance of Q-ary EPPM is shown to be better than any Q-ary pulse position-based modulation scheme with the same symbol length. Since the code is cyclic, the receiver for EPPM is simpler compared to multipulse PPM (MPPM). We show that the minimum error probability is obtained when the symbols are equidistant from each other, which makes the bit-symbol mapping for the EPPM scheme as easy as for PPM and much simpler than for MPPM. We then show that by including the complements of the codewords the number of symbols can be doubled in EPPM,

thereby improving the performance. Although BIBDs have been used in various applications, their optimality as an M-ary constellation has previously not been shown.

3.2.1 Principles of EPPM

The idea in here is to choose Q symbols out of all Q-tuples such that the resulting system has a minimum symbol error probability among all possible Q-tuple choices. We call the new scheme an expurgated PPM (EPPM), since the optimal Q-tuple set turns out to be a subset of the codewords from multipulse PPM.

Consider Q symbols (binary sequences) of length Q with weights $K_1, K_2, \ldots, K_Q$. Denote C as the $Q \times Q$ matrix formed using these symbols as rows. Let the sum of column ℓ of C be W_ℓ, where

$$\sum_{\ell=1}^{Q} W_\ell = \sum_{\ell=1}^{Q} K_\ell = A. \tag{3.1}$$

The sum of all pair-wise distances can be expressed as

$$D = \sum_{i=1}^{Q} \sum_{j=1}^{Q} d_{ij} = 2(QA - \sum_{\ell=1}^{Q} W_\ell^2), \tag{3.2}$$

where d_{ij} is the Hamming distance between symbols i and j. Using the Cauchy Inequality we know that $\sum_{\ell=1}^{Q} W_\ell^2 \geq \frac{1}{Q}(\sum_{\ell=1}^{Q} W_\ell)^2$ and therefore

$$D \leq 2A(Q - \frac{A}{Q}). \tag{3.3}$$

We assume that the error probability between symbols i and j can be written in the form $f(d_{ij})$. Our approach is to minimize the union bound on the symbol error probability [1]

$$P_s^{(U)} = \frac{1}{Q} \sum_{i=1}^{Q} \sum_{\substack{j=1 \\ i \neq j}}^{Q} f(d_{ij}). \tag{3.4}$$

Let $f(.)$ be a convex and monotonically decreasing function, which is true for erfc(.), the complementary Gaussian error function. According to Jensen's inequality [45], $P_s^{(U)} \geq (Q-1)f(d)$, where $d = \frac{D}{Q(Q-1)}$ is the mean of the d_{ij}'s, and equality holds only if $d_{ij} = d$, for $i, j = 1, 2, \ldots, Q$ and $i \neq j$. According to this, the performance is optimized when symbols are pair-wise equidistant. Using (3.3), for fixed A and Q, $P_s^{(U)}$ is minimized when $D = 2A(Q - \frac{A}{Q})$.

---

[1]This is asymptotically optimal but may not provide the optimal solution for finite distances.

Then, d is maximized for $A = Q^2/2$ and its maximum value is $d_{\max} = \frac{Q^2}{2(Q-1)}$. For equidistant codes, d should be an integer, and thus, its maximum is $\frac{Q+1}{2}$, which is $\frac{1}{2(Q-1)}$ smaller than $d_{\max}$; this cost of enforcing the equidistant property decreases as Q increases.

For cyclic codes, each codeword is a cyclic shift of the other codewords, which makes the structure of the transmitter and receiver, and also the encoding of the symbols, simpler. Henceforth, we focus on cyclic codes, which have equal weight codewords, i.e., $K_i = K \; \forall i$. Consequently, the cross-correlation between each pair of symbols is constant and equal to $K - \frac{d}{2}$. This property leads us to symmetric BIBD.

We propose to use a symmetric BIBD as a code and the rows of its incidence matrix as the codewords. Hence, for a design with parameters (Q, K, λ), Q is the number of codewords, which is equal to the code length, K is the code weight, which is defined as the number of 1's in each codeword, and λ is the cross-correlation between each pair of codewords. We denote codeword j by $\mathbf{c}_j$, which is the jth row of matrix C.

Among all available symmetric BIBDs with length Q, we want ones for which the Hamming distance between each pair of codewords is maximum. The distance between the codewords with parameters (Q, K, λ) is $2(K - \lambda)$. Using (1.1), the distance is obtained as $d = 2K(\frac{Q-K}{Q-1})$. The optimum K for maximizing d is $Q/2$. In this work, we choose codes with $Q = 2K + 1$ and $K = 2\lambda + 1$, since they have distance closest to the maximum distance among all known cyclic
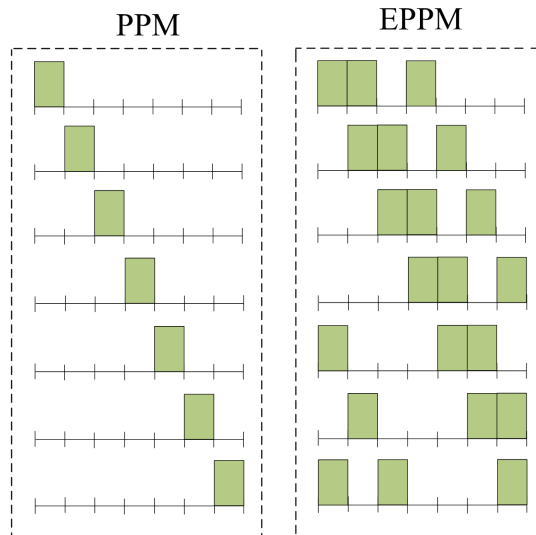
Figure 3.4: Symbols for PPM and EPPM for Q=7.

45
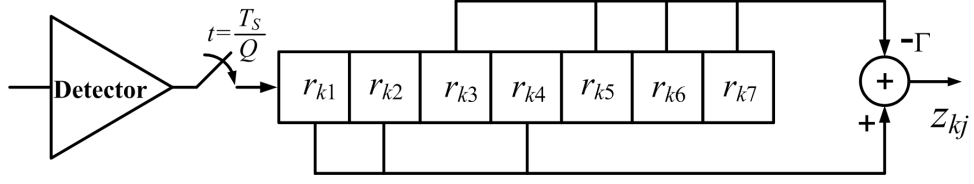
Figure 3.5: Receiver for the EPPM code shown in Figure 3.4. T_s is the symbol period.

codes. According to [1]-[2], cyclic BIBD codes are available when $Q = 2K + 1$ and $K = 2\lambda + 1$, for a vast range of λ. For these codes, the distance between the codewords is $(Q + 1)/2$, and therefore, they are optimal equidistant codes. Figure 3.4 shows the symbols for PPM and this new code, which we call EPPM, for $Q = 7$, $K = 3$ and $\lambda = 1$.

Adding the complement of the codewords as symbols can double the number of symbols. The Hamming distance between $\overline{\mathbf{c}}_j$, the complement of $\mathbf{c}_j$, and $\mathbf{c}_i$ is

$$d(\overline{\mathbf{c}}_j, \mathbf{c}_i) = \begin{cases} Q & ; i = j, \\ 2\lambda + 1 & ; i \neq j \end{cases}.$$

So extending the code size decreases the minimum distance by one. We call this an augmented EPPM (AEPPM).

In our EPPM scheme, we use the Q blocks of a cyclic BIBD as codewords. In this case, the optimal receiver assuming an AWGN channel can be implemented as a shift register followed by a differential circuit, as shown in Figure 3.5 for $Q = 7$. This detector is equivalent to the correlation receiver.

In this figure, $\Gamma = \frac{\lambda}{K - \lambda}$, and $\mathbf{r}_k = \{r_{k1}, r_{k2}, \ldots, r_{kQ}\}$ is the stored vector in the shift-register in symbol-time k with r_{kj} being the received photoelectron-count in time-slot j of symbol-time k. Symbol synchronization is a key issue for EPPM, as for PPM; similar synchronization algorithms can be used for either modulations.

The wires of the lower branch are matched to the first codeword of the BIBD code, $\mathbf{c}_1$, and those of the upper branches are matched to its complement. The differential circuit generates Q variables in each symbol period by circulating $\mathbf{r}_k$ in the shift register. The combination of the shift register and the differential circuit generates the decision statistic vector $\mathbf{z}_k = (z_{k1}, z_{k2}, \ldots, z_{kQ})$, $z_{kj} = \langle \mathbf{r}_k, \mathbf{c}_j \rangle$, $j = 1, 2, \ldots, Q$, where $\langle \mathbf{x}, \mathbf{y} \rangle$ denotes the dot product of the vectors $\mathbf{x}$ and $\mathbf{y}$. Due to the fixed cross-correlation property of the symbols in EPPM, when symbol ℓ is sent the expected value of $z_{k\ell}$, $E\{z_{k\ell}\} = K$, and $E\{z_{kj}\} = 0$ for $j \neq \ell$ [46]. So, in each symbol period, we form

the set $\{z_{k1}, z_{k2}, \ldots, z_{kQ}\}$ and choose in favor of the largest element.

In AEPPM, when we include the complements of the BIBD codewords as symbols, we can use the same receiver structure as in Figure 3.5. In that case, we extend the decision set to $\{z_{k1}, z_{k2}, \ldots, z_{kQ}, -z_{k1}, -z_{k2}, \ldots, -z_{kQ}\}$ and choose in favor of the largest element. The complexity of the decoder in this case is the same as for the EPPM decoder.

3.2.2 Performance Analysis

We assume an additive white Gaussian noise channel with power spectral density $N_0/2$, as typical for RF systems and thermal or background noise limited FSO systems. We model the effect of this noise by adding a Gaussian random variable with variance $\Delta\upsilon N_0$ to the decision statistic z_{kj}, $j = 1, 2, \ldots, Q$, where $\Delta\upsilon$ is the receiver bandwidth. Since all symbols have equal energy, the optimum maximum likelihood (ML) decision rule reduces to the minimum distance criterion, and, therefore, the receiver in Figure 3.5 is optimal. The union bound on the symbol error probability for an M-ary modulation can be expressed as [34]

$$P_s^{(U)} = \frac{1}{2M} \sum_{i=1}^{M} \sum_{\substack{j=1 \\ i \neq j}}^{M} \mathrm{erfc}\left(\sqrt{\frac{d_{ij}\,\gamma\,\eta}{2}}\right). \tag{3.5}$$

For an FSO system with bit-rate R_b, received peak optical power P_0 and photodetector responsivity ρ, the SNR (unmodulated) is $\gamma = \frac{\rho^2 P_0^2}{N_0 R_b}$ and the modulation efficiency is $\eta = \frac{\log_2 M}{Q}$. For an IR UWB system $\gamma = \frac{E_I R_b}{2\Delta\upsilon N_0}$, where E_I is the impulse pulse energy, $\Delta\upsilon$ is independent from the bit-rate, and $\eta = \frac{Q}{\log_2 M}$.

For PPM, $M = Q$ and $d_{ij} = 2$, and so the union bound is

$$P_{s,\mathrm{PPM}}^{(U)} = \frac{Q-1}{2}\,\mathrm{erfc}\left(\sqrt{\gamma\eta}\right). \tag{3.6}$$

For MPPM, M is $\binom{Q}{K}$ and for any symbol j, the number of symbols with distance d to it is $\binom{K}{d/2}\binom{Q-K}{d/2}$. Thus, we have

$$P_{s,\mathrm{MPPM}}^{(U)} = \sum_{k=1}^{K-1} \binom{K}{k}\binom{Q-K}{k}\frac{1}{2}\,\mathrm{erfc}\left(\sqrt{k\,\gamma\eta}\right) \tag{3.7}$$

For high SNRs, the smallest distance between symbols limits P_s, so (3.7) can be approximated as

$$P_{s,\mathrm{MPPM}}^{(U)} \approx \frac{K(Q-K)}{2}\,\mathrm{erfc}\left(\sqrt{\gamma\eta}\right). \tag{3.8}$$

47

Similar to PPM, the union bound for EPPM is

$$P_{s,\text{EPPM}}^{(U)} = \frac{Q-1}{2}\,\text{erfc}\big(\sqrt{(K-\lambda)\gamma\eta}\big).\tag{3.9}$$

EPPM has a $(K-\lambda)$ coding gain advantage over PPM.

To calculate the BER, let $\boldsymbol{b}_\ell$, a $(\log_2 M)$-bit binary number, be the binary sequence assigned to symbol ℓ. When the received symbol ℓ is estimated incorrectly as symbol ℓ', $d(\boldsymbol{b}_\ell, \boldsymbol{b}_{\ell'})$ bits are decoded incorrectly. Thus, for an M-ary modulation scheme, the BER can be upper bounded as [34]

$$P_b^{(U)} = \frac{1}{2M}\sum_{\ell=1}^{M}\sum_{\substack{\ell'=1\\ \ell'\neq\ell}}^{M}\text{erfc}\left(\sqrt{\frac{d_{\ell\ell'}\gamma\eta}{2}}\right)\frac{d(\boldsymbol{b}_\ell, \boldsymbol{b}_{\ell'})}{\log_2 M}.\tag{3.10}$$

For PPM and EPPM, since all symbol pairs are equidistant, the BER is independent of the bit-symbol mapping. Hence, according to (3.6) and (3.9), the BER for these two schemes reduces to $P_b = \frac{M}{2(M-1)}P_s^{(U)}$ [34, p. 399]. For AEPPM, we use the same expression as a worst case [34, p. 397]. For MPPM, unlike PPM and EPPM, the BER depends on the bit-symbol mapping. For larger constellation sizes finding the optimum bit-symbol mapping is a difficult problem for MPPM. Here, we use $P_b = P_s^{(U)}/\log_2 M$ as the best case BER for MPPM.

3.2.3 Numerical Results

In this section, numerical results are presented to compare the performance of EPPM with PPM and MPPM schemes for a constant bit-rate. The BER of 8-ary PPM ($Q = 8$), 64-ary MPPM ($Q = 12$, $K = 2$), 8-ary EPPM ($Q = 11$, $K = 5$), and 16-ary AEPPM ($Q = 11$, $K = 5$) are compared in Figure 3.6 for an FSO link. The parameters are chosen so that the width of the time-slots for all modulation schemes are approximately equal. The simulations are done using a Monte-Carlo method, and for each point at least 10/BER trials are run. The simulation results for MPPM are obtained using the optimal bit-symbol mapping presented in [47]. For all cases, the simulation results match well with the union bound for high SNRs. According to these results, EPPM requires a γ 3.5 dB and 2.3 dB lower than PPM and MPPM, respectively, for a BER=10^{-9}. For AEPPM, since the constellation size is doubled, the BER is improved compared to EPPM.

In Figure 3.7 the BERs for equal receiver complexity (number of correlations computed) are plotted using the union bound for an FSO system. For this case, the performance of the 64-ary EPPM and 128-ary AEPPM are considerably better than PPM and MPPM. EPPM requires a γ

11.7 dB and 4.5 dB lower than PPM and MPPM, respectively, for a BER of 10^{-9}. The symbol rate is the same for all modulation schemes, except for the AEPPM. Figure 3.8 shows the spectral efficiency, which is defined as the ratio of the bit-rate to the required receiver bandwidth, versus the required SNR, γ, for a BER of 10^{-5}, for OOK, PPM, EPPM, AEPPM and MPPM for FSO systems. Each point represents a scheme with different parameters. For PPM we include $Q = 2^i$ for $i = 2, 3, \ldots, 8$, and for EPPM results are obtained for $Q = 7, 11, 19, 35, 67, 131$ and 263. For PPM, EPPM and AEPPM, by increasing Q the spectral efficiency decreases. MPPM is able to achieve higher spectral efficiency since the constellation size is larger compared to other schemes. From these plots, PPM requires higher received peak power for larger Q, while the required γ for EPPM and AEPPM decreases as Q increases. Although MPPM can provide higher spectral efficiency, it needs a higher γ for a fixed BER compared to EPPM. For the same Q, AEPPM provides higher spectral efficiency and requires lower received peak power compared to EPPM. In IR UWB systems, since the receiver bandwidth is determined by the pulse-width of the impulse, for a fixed bit-rate the spectral efficiency of all schemes are equal.
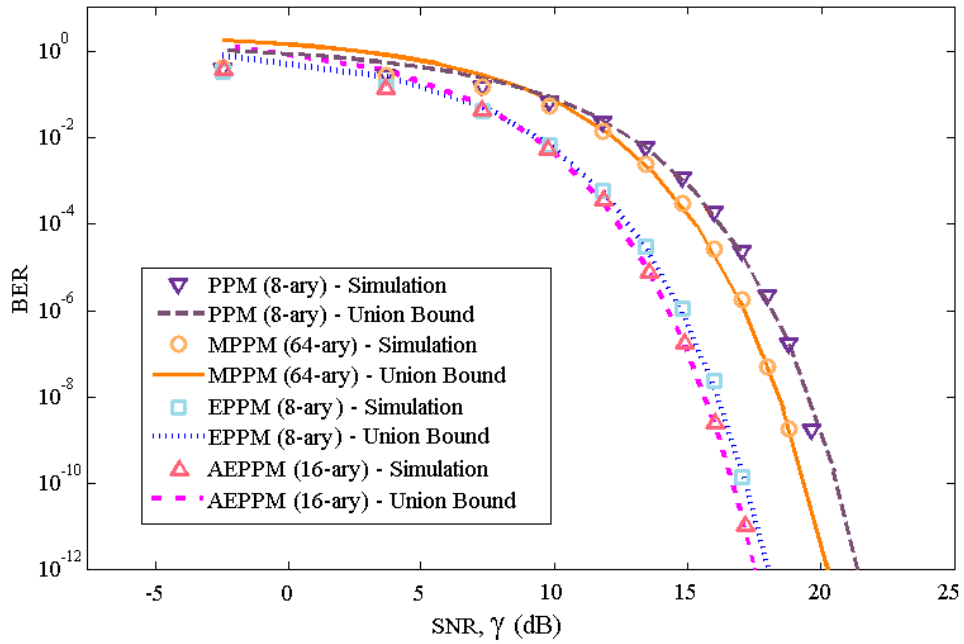
Figure 3.6: BER of an FSO link versus γ for 8-ary PPM, 64-ary MPPM, 8-ary EPPM, and 16-ary AEPPM.
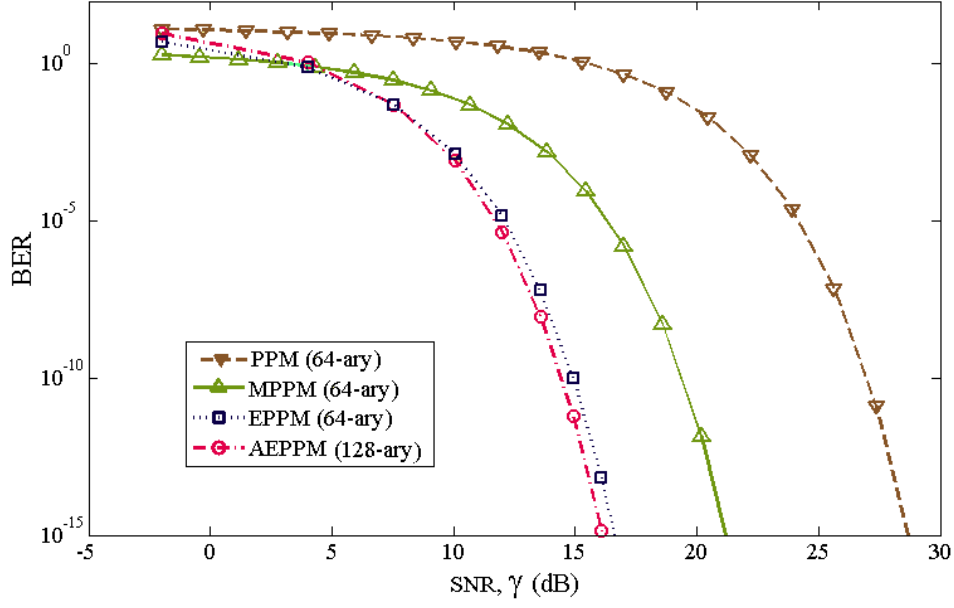
Figure 3.7: Upper bound to BER versus γ for 64-ary PPM, 64-ary MPPM, 64-ary EPPM, and 128-ary AEPPM.

3.3 Multilevel Expurgated Pulse Position Modulation

Because of the low spectral-efficiency of PPM, dispersive channels cause interference between the time-slots. Therefore, low spectral-efficiency is the main limiting factor for PPM, which makes it vulnerable to intersymbol interference (ISI), and prevents it from being used in dispersive channels, such as in the applications mentioned above. MPPM has been proposed [38] to improve the spectral-efficiency of PPM by increasing the constellation size. In this section, we propose two new multilevel pulse-position based modulation schemes to achieve higher spectral-efficiencies while simultaneously enforcing large minimum pairwise Hamming distances between symbols.

Various multilevel modulation schemes using a combination of PPM and pulse-amplitude modulation (PAM) have been proposed in the literature in order to improve the spectral-efficiency of pulse-position based modulations [48], [49], [50]. In these works, all combinations of PPM and PAM are considered as symbols, and therefore, the minimum distance between symbols is small. Moreover, the symbols in these schemes contain different energies, and hence the receiver requires a threshold value to make a decision, which is a disadvantage in fast-fading channels.

In our proposed modulation schemes, the multilevel symbols are obtained as linear combinations of BIBD codewords, and therefore, all symbols have fixed weight. These techniques can
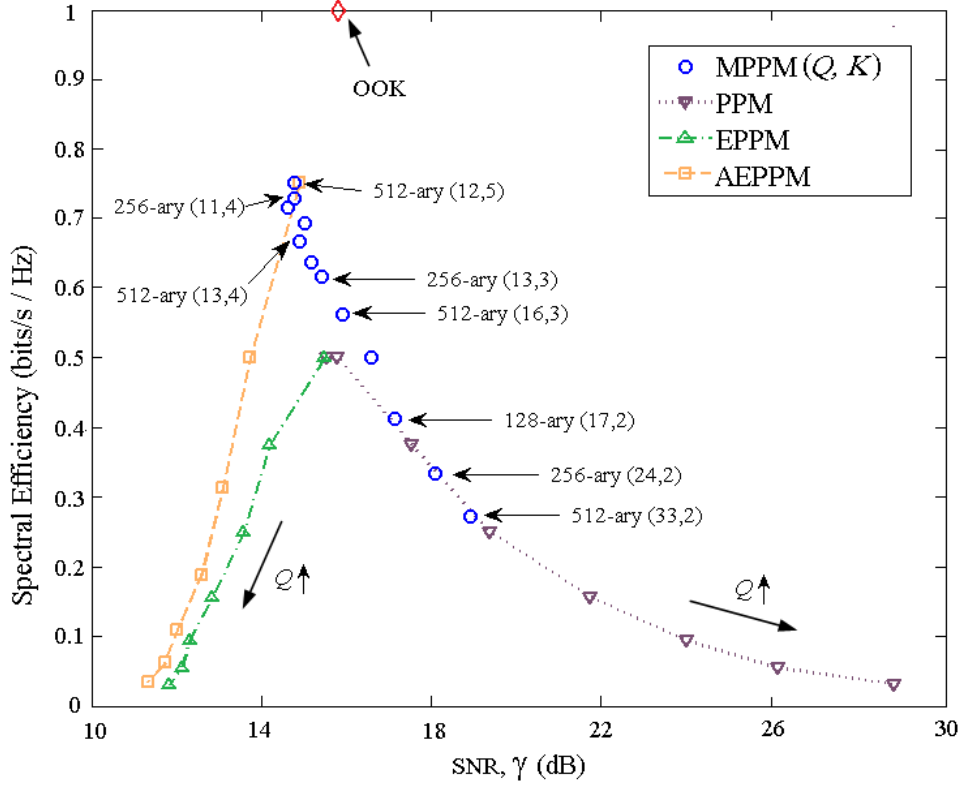
Figure 3.8: Spectral efficiency and required γ for BER of 10^{-5}, for PPM, EPPM, AEPPM, MPPM and OOK.

be considered as multilevel forms of EPPM, and thus, we call them multilevel EPPM (MEPPM). We propose two constructions of MEPPM: one with a simpler decoder and no need for a threshold, and the other with better performance in exchange for a somewhat more complex detector. These schemes can achieve high spectral-efficiencies, and are therefore suitable for systems with band-limited sources or highly dispersive channels, where ISI has a significant impact on the performance. We also show that by including the complements of the BIBD codewords the constellation size can be increased significantly, without any change in the receiver structure. The proposed technique can achieve 75% higher spectral-efficiency compared to MPPM at a BER of 10^{-5}.

3.3.1 Principles of Multilevel EPPM

This section explains the principles of the multilevel EPPM (MEPPM) and its transmitter/receiver structures. In these schemes, similar to PPM, the symbol period is divided into Q equal time-slots.

51
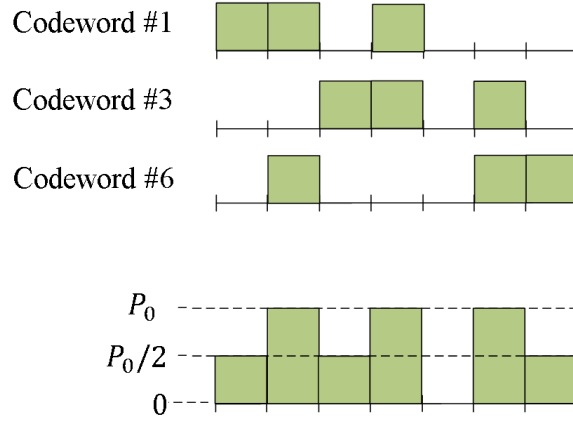
Figure 3.9: A 3-level EPPM symbol constructed using codewords 1, 3 and 6 of a $(7, 3, 1)$-BIBD.

A unipolar L-level encoding is applied on the amplitude of the optical power in each time-slot. Hence, symbol m is denoted by $\mathbf{u}_m = (u_{m1}, u_{m2}, \ldots, u_{mQ})$, where $0 \leq u_{mi} \leq L - 1$.

We use the codewords of a BIBD code to construct the symbols of MEPPM. For our MEPPM, each symbol is obtained as the sum of N BIBD codewords from the same code, resulting in new length-Q codewords. We focus on cyclic BIBDs, for which the codewords are cyclic shifts of each other. To build symbol k, N codewords are chosen, denoted as $\mathbf{c}_{m_n}$, $n = 1, 2, \ldots, N$, $m_n \in \{1, 2, \ldots, Q\}$, resulting in $\mathbf{u}_m = (u_{m1}, u_{m2}, \ldots, u_{mQ})$, where u_{mi} can be obtained as

$$u_{mi} = \sum_{n=1}^{N} c_{k_n i}. \tag{3.11}$$

According to this definition, the symbols of an MEPPM constellation have equal weight, where the weight of each symbol is NK. Figure 3.9 shows the generation of a MEPPM symbol from 3 BIBD codewords ($N = 3$). In this example, codewords $\mathbf{c}_1$, $\mathbf{c}_3$ and $\mathbf{c}_6$ of a $(7, 3, 1)$-BIBD code are added to create a symbol with length 7 and weight 9.

Since the BIBD code used to generate the multilevel symbols is assumed to be cyclic, the symbol generator circuit at the transmitter can be implemented using N shift registers in N branches, as depicted in Figure 3.10. In the general case, the number of branches, N, can be different from the number of levels, L. The optical source in the transmitter can be either a laser or an LED-array. Therefore, there can be two structures for the transmitter. In the first structure, as shown in Figure 3.10-(a), each shift register generates one BIBD codeword, and then the outputs of these N branches are added to generate the corresponding L-level symbol. The symbol generated is applied to an external amplitude modulator, which modulates the output power of the optical source.
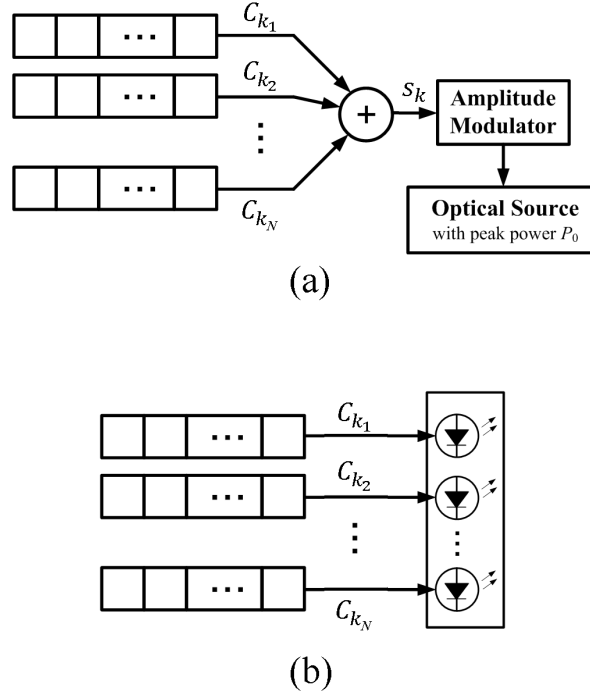
Figure 3.10: Transmitter structure and symbol generation using N shift registers and using (a) a multilevel optical source such as laser, (b) an LED-array.

Lasers used as transmitters of FSO systems are peak power limited sources, and we assume the output optical power can be modulated between 0 and P_0. The number of power levels is flexible. For symbol $\mathbf{u}_m$, the output power of the source in time-slot i is $u_{mi}P_0/(L-1)$.

An LED-array is the other option for an optical source used in FSO links for which accurate pointing is less critical. Ultraviolet (UV) communications [16] and indoor FSO systems [51] are two emerging technologies that can use LED-arrays as optical sources at the transmitter. In an LED-array, each LED can be turned on and off independently, and hence, the whole array can be considered as a multilevel source. Thus, it can be used directly as the optical source in Figure 3.10-(a). Alternatively, the transmitter using an LED-array can be implemented as in Figure 3.10-(b), in which each codeword is directly sent to a subset LEDs in the array, and hence, it is simpler than the structure in Figure 3.10-(a). The array size determines the maximum number of levels, and $L-1$ should be a divisor of the array size.

In MEPPM, each set of N BIBD codewords determines one symbol. Thus, as in EPPM, the front-end of the optimal receiver, assuming an additive Gaussian noise, can be implemented using a shift register with length Q, as shown in Figure 3.5. In this figure, Γ is $\frac{\lambda}{K-\lambda}$. The receiver

generates Q variables in each symbol period at the output of the differential circuit by circulating $\mathbf{r}_k$, the received data stored in the shift register. The combination of the shift register and the differential circuit generates the decision statistic $z_{kj} = \langle \mathbf{r}_k, \mathbf{c}_j \rangle - \Gamma \langle \mathbf{r}_k, \overline{\mathbf{c}}_j \rangle$, for $j = 1, 2, \ldots, Q$. Hence, the z_{kj}'s form a sufficient statistic for detection.

Due to the fixed cross-correlation property of the BIBD codewords, assuming that $\mathbf{c}_\ell$ is transmitted, its contribution in the expected value of $z_{k\ell}$ is $E\{z_{k\ell}\} = \frac{\mathcal{E}}{L-1} K$, and in z_{kj}, $j \neq \ell$, is $E\{z_{kj}\} = 0$ [46], where $\mathcal{E}$ is the received energy in one time-slot for an unmodulated transmitted signal with peak power P_0.

Depending on whether the codewords used in the generation of the symbols must be distinct or not, MEPPM can be categorized into two types, discussed below.

Type I Multilevel EPPM

For this scenario, the N branches generate distinct codewords, and each codeword is used at most once in the generation of each symbol, i.e., $m_i \neq m_j$ for $\forall i \neq j$. Hence, the total number of symbols for type I MEPPM with N branches is $\binom{Q}{N}$. This constellation size is maximized for $N = Q/2$.

For this case, the energy of the symbol $\mathbf{u}_m$ is

$$|\mathbf{u}_m|^2 = \Big| \sum_{i=1}^{N} \mathbf{c}_{m_i} \Big|^2 = \sum_{i=1}^{N} |\mathbf{c}_{m_i}|^2 + \sum_{i=1}^{N} \sum_{\substack{j=1 \\ j \neq i}}^{N} \langle \mathbf{c}_{m_i}, \mathbf{c}_{m_j} \rangle, \tag{3.12}$$

which, using (1.2), becomes $|\mathbf{u}_m|^2 = NK + N(N-1)\lambda$, for $\forall m$. Hence, all symbols have equal energy in type I MEPPM. For the receiver in Figure 3.5, when $\mathbf{u}_m$ is transmitted, we get $E\{z_{kj}\} = \frac{\mathcal{E}}{L-1} K$ for $j \in \{m_1, m_2, \ldots, m_N\}$, and $E\{z_{kj}\} = 0$ for $j \notin \{m_1, m_2, \ldots, m_N\}$. Thus, by finding the N largest z_{kj}'s we make an optimal decision on the received symbol. This detector does not require any threshold or energy compensation to make a decision.

In a (Q, K, λ)-BIBD code, the number of codewords that have "1" in a specific position is K. Therefore, for symbols composed of N different codewords, each element is less than or equal to K, i.e. $u_{mi} \leq K$ for $\forall m, i$. Hence, for type I, we have

$$L - 1 \leq \min\{N, K\}. \tag{3.13}$$

For $N \geq K$, which is typical, we have $L = K + 1$.

For a Gaussian additive noise channel, the symbol error probability is a function of the Euclidean distance between the symbols. Since the Hamming distance between the codewords of a (Q, K, λ)-BIBD code is $2(K - \lambda)$, the minimum Euclidean distance between the symbols of type I MEPPM is

$$d_{\min}^E = \frac{\mathcal{E}}{K} 2(K - \lambda), \tag{3.14}$$

which, using (1.1), becomes

$$d_{\min}^E = 2\mathcal{E}(1 - \frac{K - 1}{Q - 1}). \tag{3.15}$$

This distance takes its maximum value for $K = 1$, which corresponds to using PPM constituent codewords. This means that the minimum error probability is achieved when the generating codewords are the symbols of the PPM scheme. For this case, type I MEPPM reduces to multipulse PPM (MPPM). When spectral-efficiency is important, the $Q = 2K + 1$ case is used since the complements of the codewords can also be included as codewords, but when power-efficiency is important, MPPM is preferred over type I MEPPM.

Type II Multilevel EPPM

In this case, different branches are allowed to have the same codewords, i.e., one codeword can be used more than once in the generation of each symbol. To calculate the constellation size, let $n_{m,j}$ be the number of branches in symbol m that have codeword $\mathbf{c}_j$, where $0 \leq n_{m,j} \leq N$, then we have

$$\sum_{j=1}^{Q} n_{m,j} = N. \tag{3.16}$$

The energy of the symbol $\mathbf{u}_m$ for this type is

$$|\mathbf{u}_m|^2 = \Big| \sum_{j=1}^{Q} n_{m,j} \mathbf{c}_j \Big|^2 = \sum_{j=1}^{Q} n_{m,j}^2 |\mathbf{c}_j|^2 + \sum_{j=1}^{Q} \sum_{\substack{\ell=1 \\ \ell \neq j}}^{Q} n_{m,j} n_{m,\ell} \langle \mathbf{c}_j, \mathbf{c}_\ell \rangle. \tag{3.17}$$

Using (1.2) and (3.16), we get

$$|\mathbf{u}_m|^2 = (K - \lambda) \sum_{j=1}^{Q} n_{m,j}^2 + \lambda N^2. \tag{3.18}$$

As one can see, for type II MEPPM, the symbols do not have equal energies, and therefore, we need an energy compensator to make an optimal decision. For this type, the outputs of the receiver in Figure 3.5 given that $\mathbf{u}_m$ is sent are $E\{z_{kj}\} = \frac{\mathcal{E}}{L-1} n_{m,j} K$. The optimal detector can be implemented as

$$\max_{n_1^*, n_2^*, \ldots, n_Q^*} \sum_{j=1}^{Q} n_j^* \langle \mathbf{r}_k, \mathbf{c}_j \rangle - (K - \lambda) \left(\frac{\mathcal{E}}{L-1} \right)^2 \sum_{j=1}^{Q} n_j^*. \tag{3.19}$$

Using the definition of z_{kj}, the detector becomes

$$\max_{n_1^*, n_2^*, \ldots, n_Q^*} \sum_{j=1}^{Q} \left(z_{kj} - \mathcal{E} \frac{K}{L-1} n_j^* \right)^2 \tag{3.20}$$

We can use an iterative decoder to find the optimal n_j^*'s. In order to make an optimal decision, we define $w_j^{[\ell]}$ as the hypothesized n_j^* at iteration ℓ, with initial value of $w_j^{[0]} = 0$. In each iteration, we update the weights as follows

$$w_j^{[\ell+1]} = \begin{cases} w_j^{[\ell]} + 1 & j = \arg \max_{1 \leq m \leq Q} \left\{ z_{km} - w_m^{[\ell]} \mathcal{E} \frac{K}{L-1} \right\}, \\ w_j^{[\ell]} & \text{otherwise.} \end{cases} \tag{3.21}$$

At step $\ell = N$, we set $n_j^* = w_j^{[N]}$. The most likely symbol sent uses n_j^* copies of $\mathbf{c}_j$, $j = 1, 2, \ldots, Q$, assuming an additive white Gaussian noise (AWGN) channel.

The constellation size is equal to the number of solutions of (3.16), which is equal to $\binom{Q+N}{N}$. As can be seen, the constellation size for type II is larger than that of the type I, leading to a more spectrally efficient design. In contrast, it requires a more complicated receiver compared to type I.

We define M_ℓ as the number of symbols generated from exactly ℓ distinct codewords, which is equal to the number of integer solutions of

$$n_{j_1} + n_{j_2} + \cdots + n_{j_\ell} = N, \tag{3.22}$$

where $j_i \in \{1, 2, \ldots, Q\}$ for $i = 1, 2, \ldots, \ell$. The number of solutions to (3.22) is

$$M_\ell = \binom{Q}{\ell} \binom{N-1}{\ell-1}. \tag{3.23}$$

For type II MEPPM, the number of levels, L, is $N + 1$, independent from K. The minimum Euclidean distance for this case is

$$d_{\min}^E = 2 \frac{\mathcal{E}}{N} K \left(\frac{Q-K}{Q-1} \right). \tag{3.24}$$

As this discussed in Section 3.2, the optimum parameters to maximize $d_{\min}^E$ in (3.24) are $Q = 2K + 1$ and $K = 2\lambda + 1$.

Multilevel Augmented EPPM

Similar to AEPPM scheme in Section 3.2, we can increase the constellation size using these complements in MEPPM. To do this, in Figure 3.10, we first choose N codewords out of Q, and then in each branch we choose between the codeword and its complement. We call this scheme multilevel AEPPM (MAEPPM). In this way the constellation size for type I can be increased to $2^N \binom{Q}{N}$. For type II MAEPPM, using this approach the number of symbol generated from ℓ distinct codewords can be increased from M_ℓ to $2^\ell M_\ell$. So, the total number of symbols for type II MAEPPM is equal to

$$M = \sum_{\ell=1}^{N} 2^\ell \binom{Q}{\ell} \binom{N-1}{\ell-1} = P_N^{(Q-N,-1)}(3), \qquad (3.25)$$

where $P_n^{(\alpha,\beta)}(x)$ is the Jacobi polynomial [52].

For MAEPPM the same receiver as Figure 3.5 is used, and a similar decoding is applied to detect the symbol sent, except that, instead of the set $\{z_{k1}, z_{k2}, \ldots, z_{kQ}\}$, we form the set $\{z_{k1}, z_{k2}, \ldots, z_{kQ}, -z_{k1}, -z_{k2}, \ldots, -z_{kQ}\}$, and make a decision using this set.

3.3.2 Error Performance and Spectral-Efficiency

In this section we obtain expressions for the symbol error probability for the modulation schemes described above. We use the resulting expressions to derive to derive the spectral-efficiency of the various schemes. We assume an additive white Gaussian noise channel with power spectral density $N_0/2$, as appropriate for thermal or background noise limited FSO systems. We model the effect of this noise by adding a Gaussian random variable with variance $\Delta \upsilon N_0$ to the decision statistic z_{kj}, $j = 1, 2, \ldots, Q$, where $\Delta \upsilon$ is the receiver bandwidth. Therefore, the optimum maximum likelihood (ML) decision rule reduces to the minimum distance criterion. For type I, since the energies of the symbols are the same, the performance of the correlation receiver in Figure 3.5 is optimal. The union bound on the symbol error probability for an M-ary modulation can be expressed as [53, p. 334]

$$P_s^{(U)} = \frac{1}{2M} \sum_{i=1}^{M} \sum_{\substack{j=1 \\ i \neq j}}^{M} \text{erfc}\left(\sqrt{\frac{d_{ij}^H \gamma}{2(L-1)} \frac{\log_2 M}{Q}} \right). \qquad (3.26)$$

where d_{ij}^H is the Hamming distance between symbols i and j. For an FSO system with bit-rate R_b, received peak optical power P_r (unmodulated) and photodetector responsivity ρ, we define

the SNR as $\gamma = \frac{\rho^2 P_r^2}{N_0 R_b}$. For high SNRs, the smallest Hamming distance between symbols, $d_{\min}^H$, limits P_s, so (3.26) is approximated by

$$\mathrm{P}_s^{(U)} \approx \frac{M'}{2M} \mathrm{erfc}\left(\sqrt{\frac{d_{\min}^H \gamma}{2(L-1)} \frac{\log_2 M}{Q}}\right), \tag{3.27}$$

where M' is the number of symbol pairs with Hamming distance $d_{\min}^H$.

For type I MEPPM, we have $M = \binom{Q}{N}$ and, therefore, its spectral-efficiency is

$$\eta_{1,\mathrm{MEPPM}} = \frac{\log_2 \binom{Q}{N}}{Q}. \tag{3.28}$$

The smallest Hamming distance between symbols is $d_{\min}^H = 2(K-\lambda)$ and $M' = \frac{N(Q-N)}{2}\binom{Q}{N}$. MPPM is a special case with $K = 1$ and $\lambda = 0$.

For type II MEPPM, the constellation size is $M = \binom{Q+N}{N}$, and hence, we have

$$\eta_{2,\mathrm{MEPPM}} = \frac{\log_2 \binom{Q+N}{N}}{Q}. \tag{3.29}$$

For this type, $d_{\min}^H = 2(K-\lambda)$ and, for a symbol composed of ℓ distinct codewords, the number of pairs of symbols with Hamming distance $2(K-\lambda)$ is $\ell(Q-\ell)$. Hence, the total number of symbol pairs with distance $2(K-\lambda)$ is

$$M' = \frac{1}{2}\sum_{\ell=1}^{N} \ell(Q-\ell)M_\ell = \frac{Q(Q-1)}{2}\binom{Q+N-3}{N-1}. \tag{3.30}$$

For type I and type II MAEPPM, the minimum Hamming distance decreases to $d_{\min}^H = 2\lambda+1$, and the spectral-efficiencies are

$$\eta_{1,\mathrm{MAEPPM}} = \frac{N + \log_2 \binom{Q}{N}}{Q}, \tag{3.31}$$

and

$$\eta_{2,\mathrm{MAEPPM}} = \frac{\log_2 P_N^{(Q-N,-1)}(3)}{Q}, \tag{3.32}$$

respectively.

To calculate the BER, we denote the assigned $(\log_2 M)$-bit binary sequence to symbol k by $\boldsymbol{b}_k$. When the transmitted symbol k is estimated incorrectly as symbol k', $d(\boldsymbol{b}_k, \boldsymbol{b}_{k'})$ bits are decoded incorrectly. Hence, for an M-ary modulation scheme, an upper bound on the BER is given by [53]

$$\mathrm{P}_b^{(U)} = \frac{1}{2M}\sum_{k=1}^{M}\sum_{\substack{k'=1 \\ k'\neq k}}^{M} \mathrm{erfc}\left(\sqrt{\frac{d_{kk'}^H \gamma}{2(L-1)} \frac{\log_2 M}{Q}}\right)\frac{d(\boldsymbol{b}_k, \boldsymbol{b}_{k'})}{\log_2 M}. \tag{3.33}$$
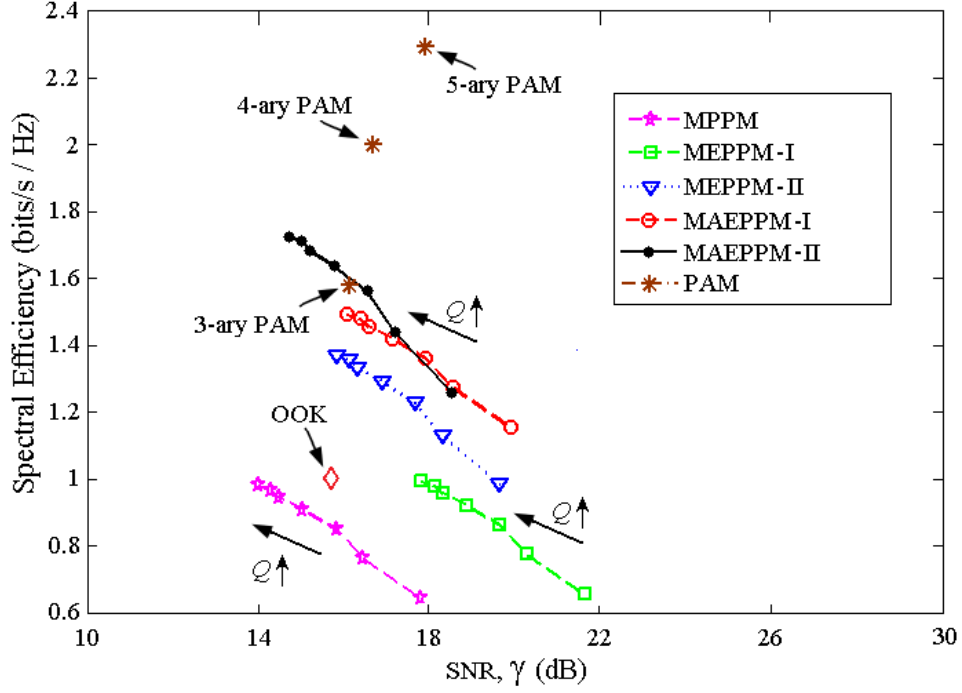
Figure 3.11: Analytical spectral-efficiency and required γ for BER of 10^{-5}, for OOK, PAM, MPPM, type I and type II MEPPM, and type I and type II MAEPPM .

For all proposed multilevel schemes, the optimum bit-symbol mapping is similar to MPPM, and is a difficult problem. Hence, in our work, we use a random bit-symbol mapping, for which the BER is $P_s^{(U)}/2$.

3.3.3 Numerical Results

In this section, numerical results are presented to compare the performance of MEPPM and MAEPPM with other schemes. We use Paley, projective geometry (PG) and twin prime power (TPP) difference sets [1] as BIBD code families in these results, as for these code families $Q = 2K + 1$ and $K = 2\lambda + 1$.

Figure 3.11 shows the spectral-efficiency from (3.28)-(3.32) versus the required SNR, γ, for a BER of 10^{-5}, for OOK, PAM, MPPM, type I and II MEPPM, and type I and type II MAEPPM from (3.27) and (3.33). Each point represents a scheme with different parameters. For all multilevel modulation schemes, $N = (Q - 1)/2$ and Q is $7, 11, 19, 35, 67, 131$ and 263. MPPM, MEPPM and MAEPPM are able to achieve high spectral-efficiencies since their constellation sizes

are large. From these plots, the spectral-efficiency is the same for MPPM and type I MEPPM, but MPPM requires a lower γ. Among all pulse-position based schemes type II MAEPPM is the most efficient modulation for spectrum usage. Type II MAEPPM is able to achieve 75% higher spectral-efficiency compared to MPPM with only a small SNR penalty.

The symbol error probability of PPM, EPPM, MPPM, MEPPM and MAEPPM are compared for a fixed bit-rate in Figure 3.12 for an FSO link. For all these schemes $Q = 19$ and $N = 9$, and for MEPPM and MAEPPM a (19,9,4)-BIBD code is used. According to these results, EPPM has the best performance among all techniques.

To test the performance of our modulation scheme in a dispersive environment in the absence of an equalizer, the BER of on-off keying (OOK), PAM, EPPM and type II MAEPPM schemes are compared in Figure 3.13 for a dispersive FSO link. A practical example of a dispersive FSO link is NLOS-UV channel. For this FSO link, the channel impulse response is assumed to be Gaussian with broadening factor σ, i.e. $h(t) = \frac{1}{\sqrt{2\pi}\sigma} \exp(-t^2/2\sigma^2)$. Here we assume γ is 16 dB. For EPPM
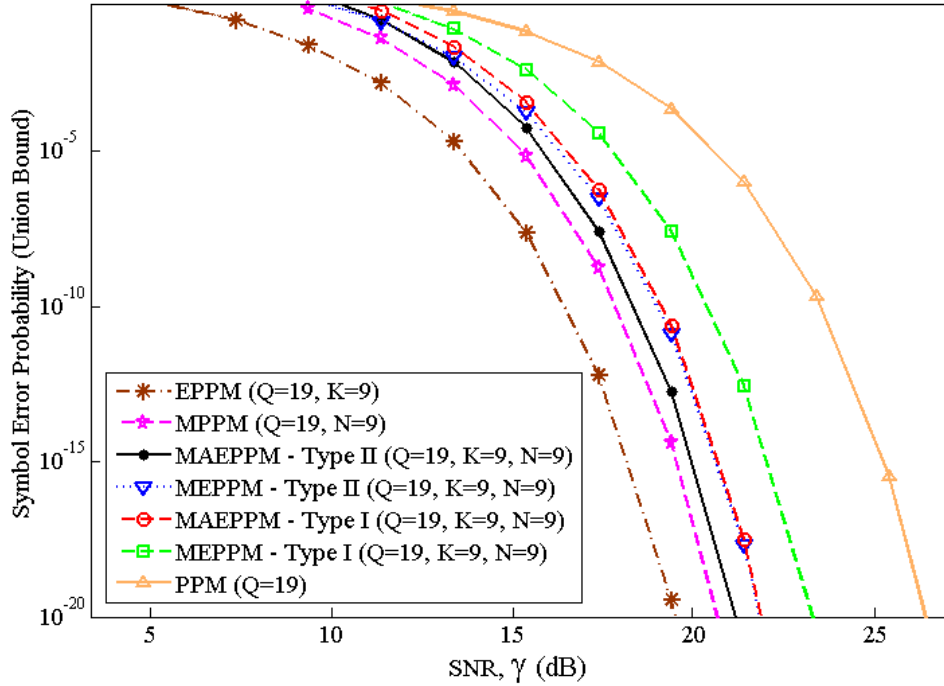
Figure 3.12: Union bound on symbol error probability of an FSO link versus γ for PPM, EPPM, MPPM ($N = 9$), type I and type II MEPPM ($N = 9$), and type I and type II MAEPPM ($N = 9$). For all these schemes $Q = 19$.
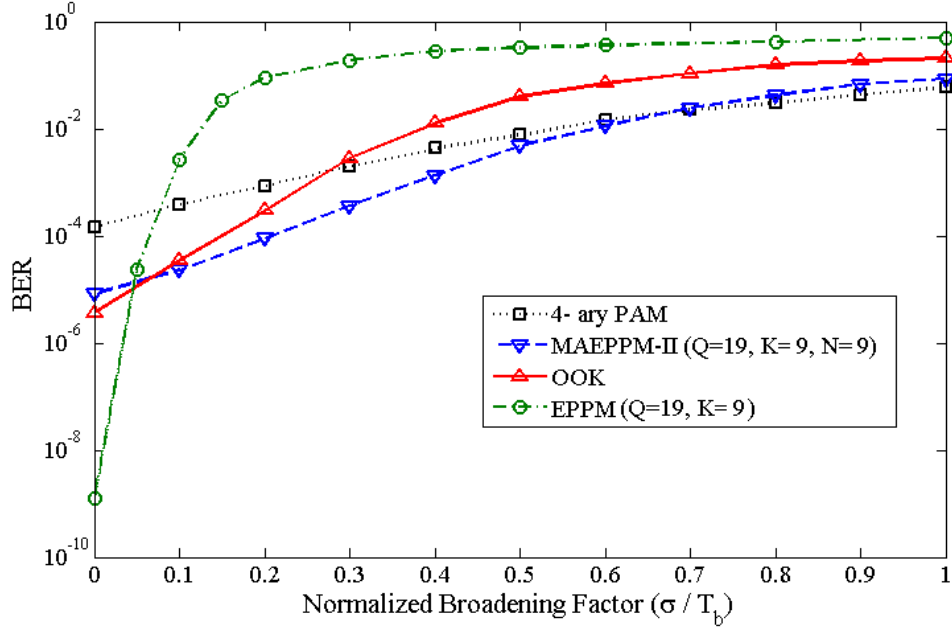
Figure 3.13: Simulated BER vs. normalized broadening factor for a FSO link for OOK, EPPM, type I MAEPPM and 4-ary PAM.

and type II MAEPPM, a BIBD code with $Q = 19$, $K = 9$ and $\lambda = 4$ is used. The BERs are plotted versus the normalized broadening factor, σR_b, where R_b is the bit-rate. The transmitted signal is assumed to have a non-return-to-zero rectangular pulse shape, and the received pulse is obtained by convolving the transmitted signal with the channel impulse response. By increasing σR_b, the ISI effect becomes the dominant limit, and, therefore, schemes with higher spectral-efficiencies perform better. Although EPPM has the lowest BER for non-dispersive channels, it is the most vulnerable scheme to ISI since it has the lowest spectral-efficiency. On the other hand, while 4-ary PAM has the best performance in high dispersive channels, because of its low BER at $\sigma = 0$, it is not the best technique for low dispersive channels. Type II MAEPPM has the best performance for medium dispersion cases, and suffers only a small performance penalty compared to 4-PAM in high dispersion cases.

3.4 Coded Quadrature Phase Shift Keying

In this section, a new M-ary modulation scheme based on quadrature phase shift keying (QPSK) for application in RF energy constrained communication systems is presented. Balanced incom-
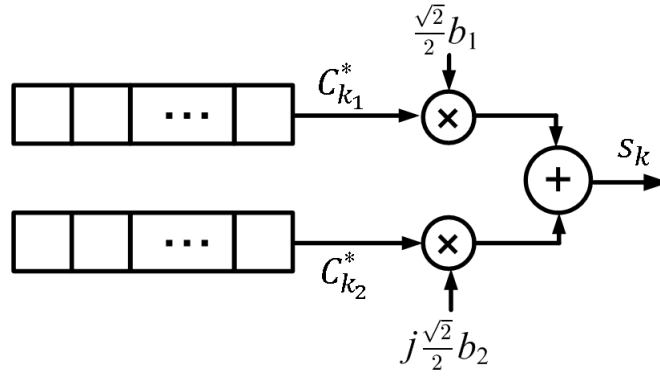
Figure 3.14: Transmitter structure and symbol generation using two shift registers.

plete block designs (BIBD) are used for constructing the symbol alphabets. Each symbol is obtained by combining two bipolar BIBD codewords, one in-phase and the other quadrature-phase. Simple transmitter and receiver structures using shift registers are proposed. Due to the fixed cross-correlation property of BIBD codes, symbols have equal energies, and therefore, no threshold is needed to make a decision on the received signal. Because of the large distance between symbols, this scheme is more power efficient than standard QPSK. The performance of various modulation schemes are compared using numerical results for an additive white Gaussian noise (AWGN) channel and a bandwidth limited channel.

3.4.1 Principles of Coded QPSK

PPM is considered as the primary M-ary transmission technique in impulse-radio ultra-wide-band (IR-UWB) systems, since it has a simple transmitter/receiver structure, and does not need a threshold at the receiver to make an optimum decision. Except for IR-UWB systems, the application of PPM has not been extended to radio-frequency (RF) systems, where phase-encoded modulations are preferred since they have higher spectral efficiency. In Section 3.2, we propose EPPM as an alternative technique to PPM to improve the performance of peak-power limited M-ary communication systems, and in Section 3.3 MEPPM is introduced to increase the spectral efficiency of pulse-position based modulations, and achieve spectral efficiencies larger than unity. In order to extend these modulation techniques to RF communication systems, we combine these techniques with quadratic phase shift keying (QPSK). BIBD codes are the basis for the symbol construction in this modulation scheme. In order to have simple transmitter and receiver structures, cyclic BIBD codes are used in this work.

In our proposed M-ary modulation scheme, similar to PPM, the symbol period is divided into Q equal time-slots, and then phase modulation is applied in each time-slot. Hence, symbol m is denoted by $\mathbf{u}_m = (u_{m1}, u_{m2}, \ldots, u_{mQ})$, where $|u_{mi}| = 1$. We use the codewords of a BIBD code to construct the symbols. We define bipolar BIBD codes as $\mathbf{c}_i^* = \mathbf{c}_i - \overline{\mathbf{c}_i}$, where $\overline{\mathbf{c}_i}$ is the complement of $\mathbf{c}_i$. For this scheme, each complex-valued symbol is obtained by combining two bipolar BIBD codewords from the same code, resulting in new length-Q codewords. To build symbol k, two codewords (not necessarily distinct) are chosen, denoted as $\mathbf{c}_{m_n}^*$, $n = 1, 2$, $m_n \in \{1, 2, \ldots, Q\}$, resulting in $\mathbf{u}_m = (u_{m1}, u_{m2}, \ldots, u_{mQ})$, where u_{mi} can be obtained as

$$u_{mi} = \frac{\sqrt{2}}{2}\Big(b_1(c_{m_1 i} - \overline{c_{m_1 i}}) + jb_2(c_{m_2 i} - \overline{c_{m_2 i}})\Big), \tag{3.34}$$

where $j = \sqrt{-1}$, and $b_1, b_2 \in \{-1, 1\}$. The total number of symbols for this scheme is $4Q^2$. This constellation has Q dimensions, each with biorthogonal components.

In this system the minimum Euclidean distance between each two symbols in (3.34) is

$$d(\mathbf{u}_m, \mathbf{u}_\ell) = 2\sqrt{(K - \lambda)}, \tag{3.35}$$

for $m \neq \ell$ and $\forall m, \ell \in \{1, 2, \ldots, Q\}$. As is shown in Section 3.2, BIBD codes with $Q = 2K + 1$ and $K = 2\lambda + 1$ have the largest Hamming distance than any other code with Q codewords of length Q, and therefore, in this work we use these families to generate the symbols.

Since the BIBD code used to generate the symbols is assumed to be cyclic, the symbol generator circuit at the transmitter can be implemented using two shift registers in two branches, as depicted in Figure 3.14. In this transmitter, each shift register generates a BIBD code, and then the output is multiplied by, b_i, $i = 1, 2$.

According to (3.34), symbols have equal energies, and therefore, as in EPPM, the optimal receiver, assuming an AWGN channel, can be implemented using a shift register with length Q, as shown in Figure 3.5.

For this receiver, when symbol m is transmitted, we observe $\big|E\{z_{ki}\}\big| = \frac{\sqrt{2}}{2}\sqrt{\mathcal{E}}$ for $i \in \{k_1, k_2\}$, where $\mathcal{E}$ is the received energy per symbol, and $E\{z_{ki}\} = 0$ for $i \notin \{m_1, m_2\}$. Thus, by choosing the two largest $|z_{ki}|$'s we make a maximum likelihood decision on the codewords sent. Then, by applying independent phase decodings on each z_{ki} we can find b_1 and b_2, and make an optimal decision on the received signal. This detector does not require any threshold or energy compensation to make a decision.

3.4.2 Performance Analysis

A upper bound on the symbol error probability of coded-QPSK in an AWGN channel is obtained using a union bound, which is defined as

$$P_s^{(U)} = \frac{1}{2M} \sum_{m=1}^{M} \sum_{\substack{\ell=1 \\ \ell \neq m}}^{M} \text{erfc}\left(\frac{d(\mathbf{u}_m, \mathbf{u}_\ell)}{2} \sqrt{\frac{\gamma}{2}} \right), \tag{3.36}$$

where $M = 4Q^2$, $\gamma = \frac{\mathcal{E}}{2QN_0}$, N_0 is the noise power, and erfc(.) is the complementary Gaussian error function. According to (3.34), the union bound can be expressed as

$$
\begin{aligned}
P_s^{(U)} =& (Q-1)\text{erfc}\left(\sqrt{\frac{\gamma}{2}} \sqrt{(K-\lambda)} \right) \\
& + (Q-1)\text{erfc}\left(\sqrt{\frac{\gamma}{2}} \sqrt{\frac{Q}{2} - (K-\lambda)} \right) \\
& + ((Q-1)^2 + 1)\text{erfc}\left(\sqrt{\frac{\gamma}{2}Q} \right) \\
& + \frac{(Q-1)^2}{2}\text{erfc}\left(\sqrt{\gamma}\sqrt{(K-\lambda)} \right) + \frac{1}{2}\text{erfc}\left(\sqrt{\gamma Q} \right) \\
& + \frac{(Q-1)^2}{2}\text{erfc}\left(\sqrt{\frac{\gamma}{2}} \sqrt{Q - 2(K-\lambda)} \right) \\
& + (Q-1)\text{erfc}\left(\sqrt{\frac{\gamma}{2}} \sqrt{\frac{Q}{2} + (K-\lambda)} \right) \\
& + (Q-1)\text{erfc}\left(\sqrt{\frac{\gamma}{2}} \sqrt{Q + (K-\lambda)} \right).
\end{aligned}
\tag{3.37}
$$

For a high signal to noise ratio (SNR), the dominant terms are the ones that correspond to symbols with minimum distance. Hence, the union bound is approximated as

$$P_s^{(U)} \approx (Q-1)\text{erfc}\left(\sqrt{\frac{\gamma}{2}} \sqrt{(K-\lambda)} \right). \tag{3.38}$$

Then an upper bound on the BER can be calculated as

$$P_b^{(U)} = \frac{1}{2M} \sum_{k=1}^{M} \sum_{\substack{\ell=1 \\ \ell \neq k}}^{M} \frac{d\mathbf{b}_k, \mathbf{b}_\ell)}{\log_2 M}\text{erfc}\left(\frac{d(\mathbf{s}_k, \mathbf{s}_\ell)}{2} \sqrt{\frac{\gamma}{2}} \right), \tag{3.39}$$

where $\mathbf{b}_k$ is the binary sequence assigned to symbol k.

3.4.3 Numerical Results

In this section, numerical results are presented in order to compare the performance of coded-QPSK with other modulation schemes. We use Paley difference sets with $Q = 2K + 1$ and
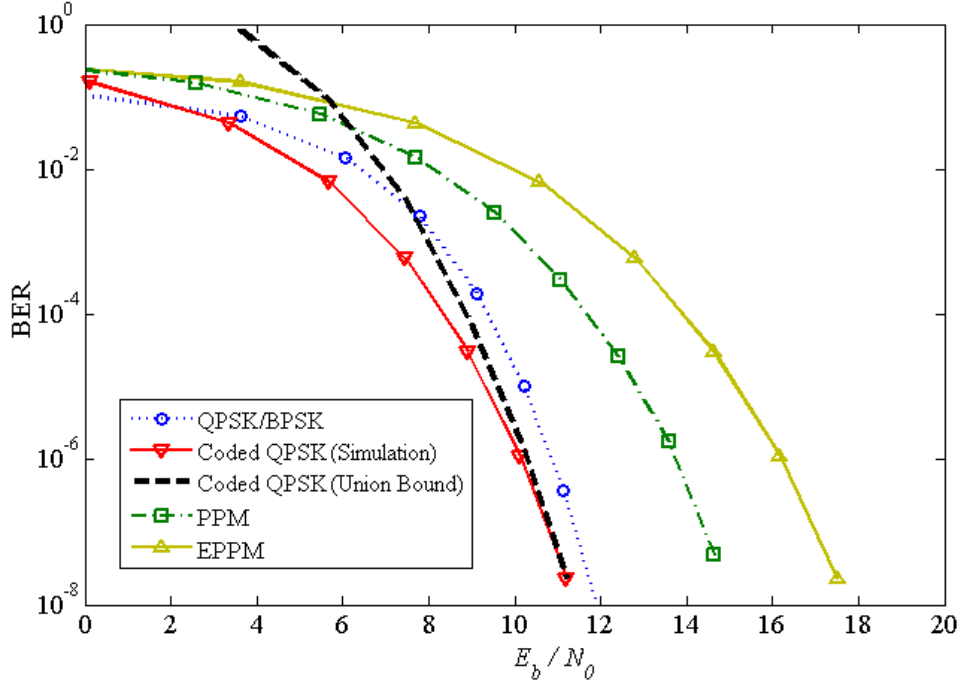
Figure 3.15: Simulation results for BER of an IR-UWB link versus E_b/N_0 for 64-ary PPM, 64-ary EPPM, 2^{14}-ary BIBD coded QPSK, QPSK and BPSK. An ideal AWGN channel is assumed.

$K = 2\lambda + 1$ [1] as BIBD codes in these results. These results are obtained from simulations using Monte-Carlo approach, and for each point a confidence level of 95% is considered.

Figure 3.15 shows a comparison between the BER of 64-ary PPM, 64-ary EPPM ($Q = 67$, $K = 33$), 2^{14}-ary BIBD coded QPSK ($Q = 67$, $K = 33$), QPSK, and binary phase shift keying (BPSK) versus the SNR, E_b/N_0, for an IR-UWB system over an AWGN channel. In this plot, E_b is the received energy per bit. The parameters are chosen so that the number of the time-slots for BIBD coded QPSK, EPPM and PPM are approximately equal. The bit-rate is assumed to be equal for all modulation schemes. According to these results, BIBD coded QPSK requires lower E_b/N_0 compared to EPPM, PPM and QPSK. In these results, a random bit-symbol mapping is used to map $\lfloor (\log_2 Q) \rfloor$ bits to the BIBD codewords in each branch, where $\lfloor n \rfloor$ is the largest integer smaller than n. The union bound is also plotted in this figure for coded-QPSK using the same bit-symbol mapping.

The performances of different modulation schemes for a dispersive channel are shown in Figure 3.16 in the absence of an equalizer. For this link, the channel impulse response is assumed to be Gaussian with broadening factor σ, i.e., $h(t) = \sqrt{\frac{1}{2\pi\sigma}} \exp(-\frac{t^2}{2\sigma^2})$. We assume an integrate
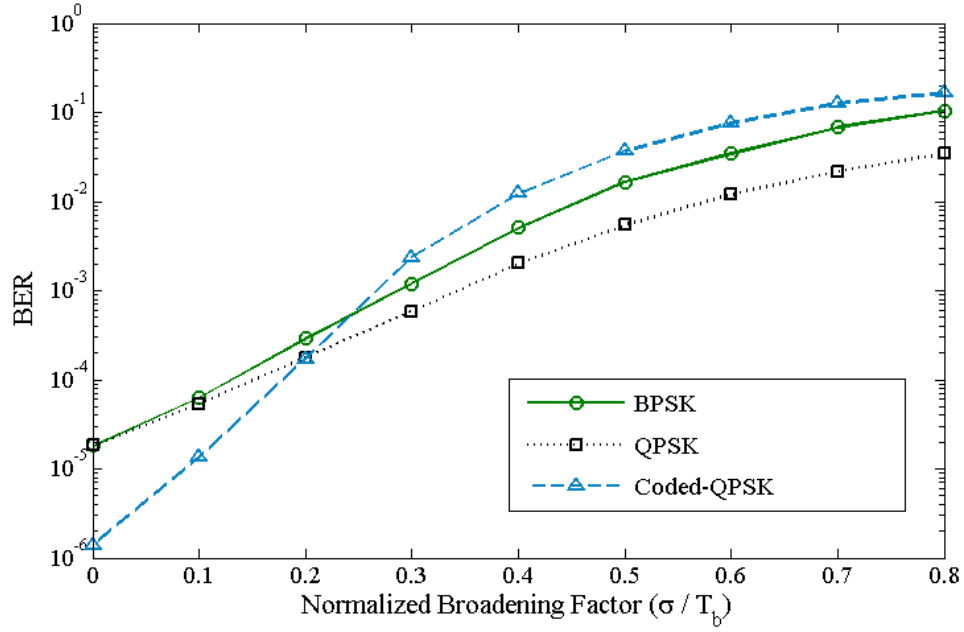
Figure 3.16: Simulation results for BER of a Gaussian dispersive channel versus the normalized broadening factor, σR_b, for QPSK, BPSK and 2^{14}-ary BIBD coded QPSK.

and dump filter over each pulse at the receiver. Here we assume the SNR is 16 dB. The BERs are plotted versus the normalized broadening factor, σR_b, where R_b is the bit-rate. The transmitted signal is assumed to have a non-return-to-zero rectangular pulse shape, and the received pulse is obtained by convolving the transmitted signal with the channel impulse response. By increasing σR_b, the ISI effect becomes the limiting degradation, and therefore, schemes with higher spectral-efficiencies perform better.

3.5   Summary

In this chapter, a novel modulation scheme, called expurgated PPM, using the symmetric BIBD is introduced, and its advantages over PPM and MPPM schemes are described. Our new proposed approach is efficient for peak power limited communication systems and, therefore, can be used in FSO links and IR UWB communications. The bit-symbol mapping for EPPM is similar to PPM and can be easily implemented since all symbols are pair-wise equidistant. The symbols in EPPM can be cyclic shifts of each other, which simplifies the transmitter and receiver structures.

Novel modulation schemes called multilevel expurgated PPM are proposed. The symbols are

constructed by combining several BIBD codewords. Indeed, the symbols of these schemes can be considered as a subset of combined PPM-PAM symbols. Because of the large constellation sizes that can be achieved, the proposed schemes are more spectrally efficient than MPPM, PPM and EPPM. Simple transmitter and receiver structures using shift registers are presented. MEPPM is divided into two types, based on the variety of the codewords that can be considered in the generation of the symbols. It is shown that by adding the complements of the BIBD codewords, a larger constellation size can be attained for the same transmitter/receiver structures. Analytical symbol error probabilities and spectral-efficiencies are calculated, and numerical results are presented to compare the performance of the proposed schemes with other modulation techniques. The application of MEPPM and MAEPPM in dispersive FSO channels is also discussed, and their performances are compared with OOK and PAM. The proposed schemes are shown to outperform existing techniques over dispersive channels.

A new modulation scheme suitable for RF systems called coded-QPSK is introduced, which is shown to be more energy-efficient compared to PPM, QPSK and BPSK, and requires a lower SNR for the same performance at the expense of a larger required bandwidth for the same bit-rate. According to the simulation results, coded-QPSK achieves a lower BER compared to QPSK in low and medium dispersive channels.

Chapter 4

Application to Indoor Optical Wireless Networks

Optical wireless communications (OWC) has been recently proposed for indoor networks in order to provide high-speed access for phones, PCs, printers and digital cameras in offices, shopping centers, warehouses and airplanes [54]. The integrability of visible light communications (VLC) with the illumination system and its RF interference-free nature are the main factors that make this technique appealing for indoor applications. These systems must not only fulfill the requirements of the communication systems, but should also be able to support the indoor lighting needs. Yet the low-bandwidth optical sources used and dispersive channels encountered limit the throughput.

Integrating VLC networks with illumination systems imposes limitations on the modulations and networking techniques that can be used. White LED are the most common optical sources that are used in VLC systems, and modulation schemes that can be used with these devices are limited. Because of the structure of these LEDs and their inherent nonlinearity, implementing modulation and multiple-access approaches that require a frequency-domain processing is expensive and complicated. Therefore, time-based modulations, specially pulsed techniques, are the preferred modulation technique in LED-based VLC systems. Dimming is an important feature of indoor lighting systems through which the illumination level can be controlled. The dimming level of the lighting systems corresponds to the peak to average power (PAPR) of the modulation technique, and hence, the more PAPRs a modulation scheme operates with, the wider the range of dimming levels that are supported. Including dimming in VLC system requires further constraints on the multiple-access schemes that can be used.

In this chapter, new modulation and networking techniques using BIBDs are proposed for VLC systems. Section 4.2 proposes to apply EPPM and MEPPM to indoor VLC systems. These two modulations enable the system to operate over a wide range of PAPRs by controlling the ratio of the code-weight to the code-length of the generating code. They are able to provide high data-rates in VLC system, while having a lower flicker effect compared to other modulation techniques.

In Section 4.4, two networking methods are proposed based on MEPPM to provide multiple access for simultaneous users in a VLC system. These two techniques, which can be considered as synchronous OCDMA methods, enable users in a VLC network to have high-speed access to the network. In the first method we assign one OOC codeword to each user in order to encode its M-ary data and transmit the cyclic shifts of the assigned OOC codeword as symbols. For each user, every bit of this encoded binary sequence is multiplied by a BIBD codeword, and then the OOC-encoded BIBD codewords are added to generate a multilevel signal. Hence, the PAPR of the transmitted data can be controlled by changing the code-length to code-weight ratio of the BIBD code. In the second technique, a subset of BIBD codewords is assigned to each user, and then the MEPPM scheme is used to generate multi-level symbols using the assigned codewords. In this approach, users can have different bit-rates by partitioning the BIBD code into unequal-size subsets.

The results of this chapter have been published in four papers [55], [56], [57] and [58].

4.1   System Description

We focus on indoor optical systems comprising LED optical sources, a diffuse channel, and a p-i-n photodetector, as described in this section. LEDs are the preferred light sources for indoor communication applications due to eye-safety regulations, low cost, and high reliability compared to lasers, incandescent and fluorescent sources [54]. Using LEDs, both lighting and communications needs can be fulfilled at the same time. In a VLC system, where arrays of white LEDs are used as sources, the downlink configuration is as shown in Figure 4.1. One or several sources are placed on the ceiling, and receivers are situated within the room, usually on desks. In our system, VLC is used only for the downlink, and for the uplink channel infrared (IR) communications can be used. In this way full-duplex communication does not cause self-interference. The standard office illuminance determined by the Illuminating Engineering Society of North America at a distance of 0.8 m from the ceiling is 400 lx [59]. For a detector with 1 cm^2 effective area, 1 lx generates
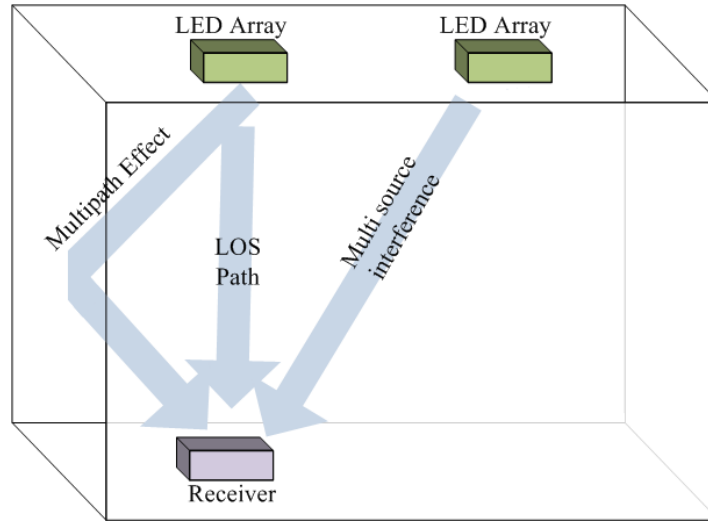
Figure 4.1: The configuration of a VLC system with two lighting sources and two users.

10^{-4} mW optical power.

There are severe limitations on the modulation schemes that can be used in VLC systems, imposed by either illumination features or the devices that are used for simultaneous lighting and communication purposes. Figure 4.2 depicts the components of a typical downlink VLC system and their corresponding challenges. An appropriate modulation technique should be able to provide solutions for these issues and fulfill the required constraints. In this section we outline the main design considerations that are required for modulations in VLC.

4.1.1 White LEDs

LEDs are the most likely optical sources for a dual-use lighting and communication application, and thus form the central component of the VLC system transmitter. They are preferred over other lighting sources, such as incandescent and fluorescent sources, since they can respond to faster modulations and support higher data-rates. LEDs are preferred over laser diodes (LD) due to safety regulations, as LDs in the visible range can be harmful to the eyes. White LEDs are used as arrays to provide the required illuminance in indoor lighting. There are two type of LEDs that use different technologies to generate white light by combining several colors. In the first technique, an LED emitting blue light is embedded in a layer of yellow phosphor that converts some of the light to longer wavelengths, yellow and red; the result is seen as white light to the human eye. The second type is a trichromatic LED, in which green, blue and red LEDs are integrated into a single

70

device to emit white light. This kind of LED enables easy color rendering by adjusting each color independently. Despite the phosphorescent LEDs having a lower price compared to trichromatic LEDs, the latter are preferred for dual-use since they have a faster rise-time and each color can be modulated independently, tripling the total throughput.

High-speed communications require either high bandwidths (fast rise-times) and/or the use of spectrally-efficient modulation schemes. Commercially viable VLC systems must use LEDs, yet the bandwidth of the existing low-cost devices is limited to a few MHz for phosphor-based LEDs
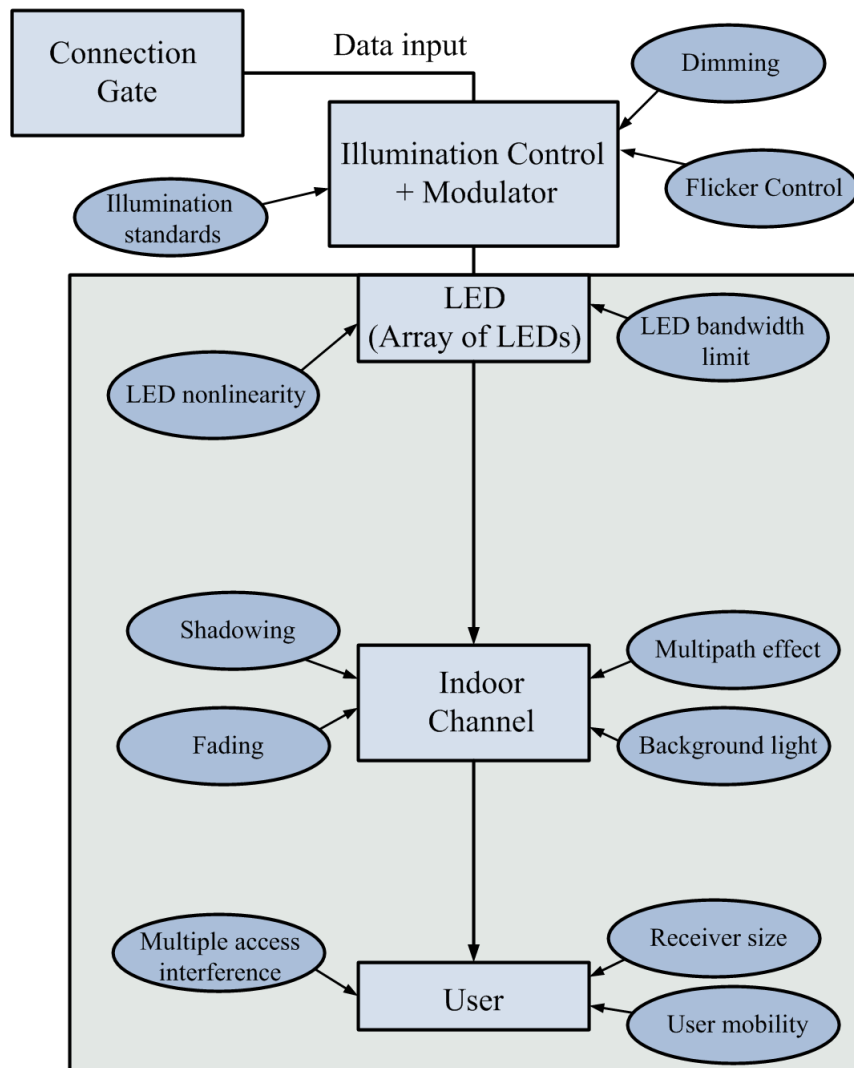
Figure 4.2: Configuration of a downlink VLC system using LED arrays, and challenges affecting each component.

and a few tens of MHz for trichromatic LEDs. In [51], blue-filtering is introduced as an efficient technique for increasing the modulation bandwidth in phosphor-based LED. Also, Le-Minh [60] has proposed an equalization technique at the transmitter to considerably increase the net bandwidth of LEDs. Still the source rise-time is insufficient for binary high-speed transmission, requiring the use of higher-order modulation.

As shown in Figure 4.2, the other major limitation imposed by LEDs is their nonlinear transfer function, through which the output power of the LED changes nonlinearly with the modulated input current. This nonlinearity introduces a distortion on the transmitted signal, and this may degrade the performance of the system. Analog or subcarrier modulation schemes suffer from this nonlinear behavior the most. Among the multiple solutions that have been proposed to mitigate this problem, the most efficient is to limit the modulation index so that high peak amplitudes are avoided, which forces the LED to operate in the linear regime and circumvents the problem. Unfortunately this approach also lowers the effective SNR. Commercially available LED lamps are composed of an array of LEDs, so that they can provide high illumination levels. Below we describe how to use this structure to avoid some of the nonlinear distortion of single LED transmitters in multi-amplitude modulation schemes.

Note that transmitter rise-time and amplifier nonlinearity are likely to be encountered by any technology attempting high throughput communications. However, the limits seen by white LEDs are particularly severe, making the design of high-speed modulation schemes especially challenging.

4.1.2   Features of the Lighting System

One of the attractive aspects of VLC is the possibility to design dual-use systems satisfying both indoor illumination and communications needs. While this approach saves energy, requirements of the lighting system impose extra requirements on the communication system.

Dimming is an important feature of indoor lighting systems through which the illumination level can be controlled by the user. To support dimming, a practical VLC system should be able to operate at various optical peak to average power ratios (PAPR) so that, for a fixed peak power LED, the average power, which is proportional to the illumination, can be regulated. Continuous current reduction (CCR) and pulse-width modulation (PWM) are two techniques that have been proposed for dimming in indoor VLC systems [61]; these techniques require large bandwidths, and are therefore not suitable for high-rate systems. Dimming to low light-levels also reduces

the power received at the mobile, potentially affecting the data-rate that is achievable. Dimmable VLC systems must be adaptive, adding complexity to the entire system.

Flicker is a fluctuation of the illumination that can be perceived by human eyes and must be avoided. After long-term exposure, flicker can be harmful to the eye and affect eyesight. In VLC systems, since the lighting is integrated with the communication system, an inappropriate modulation scheme can cause variations in the average transmitted power, and impose fluctuations on the brightness of the LEDs. Therefore, constraints need to be applied to modulation techniques that are aimed at dual-use VLC systems. The flicker becomes important when the data-rate is low, or the lights are dimmed to a low illumination level. Even though the IEEE 802.15.7 standard has devised some techniques to alleviate flicker in VLC, suitable modulation schemes are still required to have a constant average power over several symbols.

4.1.3   Indoor VLC Channel

The channel impulse response of a VLC system is composed of two parts: a line-of-sight (LOS) part that is the response received from the direct path to the closest light source, and a non-line-of-sight (NLOS) part that is the response received after reflection from walls and other objects. The latter can also be considered as multipath. The LOS part of the impulse response is usually short and sharp, and the NLOS part is instead broad, depending of the reflectivity of the walls and the size of the room. This broad response causes an intersymbol interference (ISI) effect on a high-speed transmitted data stream and degrades the quality of the received signal. Therefore, modulations that are less susceptible to ISI are of interest in VLC.

Another important channel effect in VLC is shadowing, which is a blocking of the direct path from the lighting source to the photodetector. According to the results of [62] and [63] the impulse-response of a single-source VLC channel, $h(t)$, is composed of two parts as shown in Figure 4.3, i.e., $h(t) = h_{\text{LOS}}(t) + h_{\text{NLOS}}(t)$. The first term, $h_{\text{LOS}}(t)$, is a short pulse with a large peak power, and is received from the LOS path. This short pulse is followed by a broad pulse with low peak power, $h_{\text{NLOS}}(t)$, that corresponds to the multipath effect. In VLC systems, the LOS part has a high blocking probability because visible light radiation does not penetrate opaque objects, unlike RF waves. Shadowing can be caused by obstructions in the indoor environment or by people moving, making the channel time-varying. As is shown in Figure 4.4, in the shadowed situations the impulse response of the channel has only the NLOS part, i.e., $h(t) = h_{\text{NLOS}}(t)$, and data is retrieved using this part. Since the VLC channel response can change very fast, modulation

schemes that do not require a threshold to make decision are preferred.

Both of these channel effects are present to some extent in RF communications. The added problem of fading due to multipath-wave cancelation so prevalent in RF is not experienced in VLC since the optical sources are intensity modulated (IM) and incoherent.

The width of the LOS and NLOS impulse-responses and the time delay between them, τ, is determined by the room geometry. The second term of the impulse-response causes inter-symbol interference (ISI) in VLC systems. In this work we assume that the duration of the LOS part is short compared with the pulse-width, i.e. $h_{\text{LOS}}(t) \sim \delta(t)$, and we approximate $h_{\text{NLOS}}(t)$ as a Gaussian function with width σ. This approximation is accurate for indoor environments with many reflecting surfaces. In a multi-source VLC system, we assume that the data transmitted from all LED arrays in a room are the same and synchronous. For each receiver, the closest LED array is considered as the main data source, and the signal received from the direct path of that source is assumed as the main signal. The other signals from other sources that are far from the receiver and the signals reflected from the walls contribute to $h_{\text{NLOS}}(t)$.

The last problem encountered in VLC is potentially strong background light, especially if direct sunlight is in the FOV of the photodetector. Illumination levels are strong enough that in the absence of background light the SNR is quite high. Unlike RF where interference can be mitigated by using MIMO processing, background light increases the shot noise of the system irreparably.
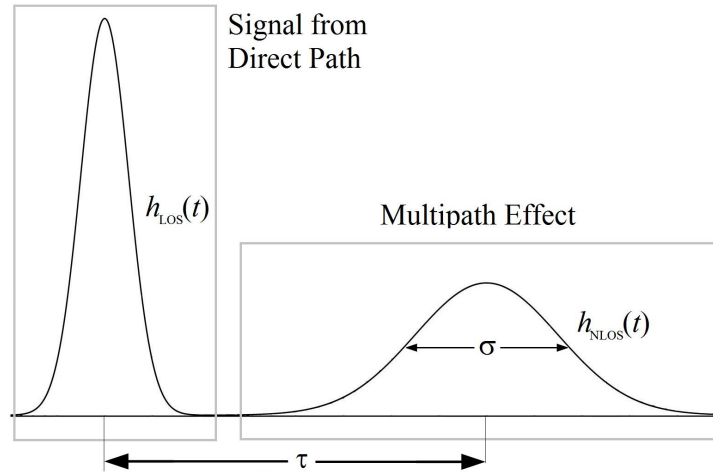
Figure 4.3: The impulse-response of a VLC channel that is composed of the LOS and NLOS parts.

74
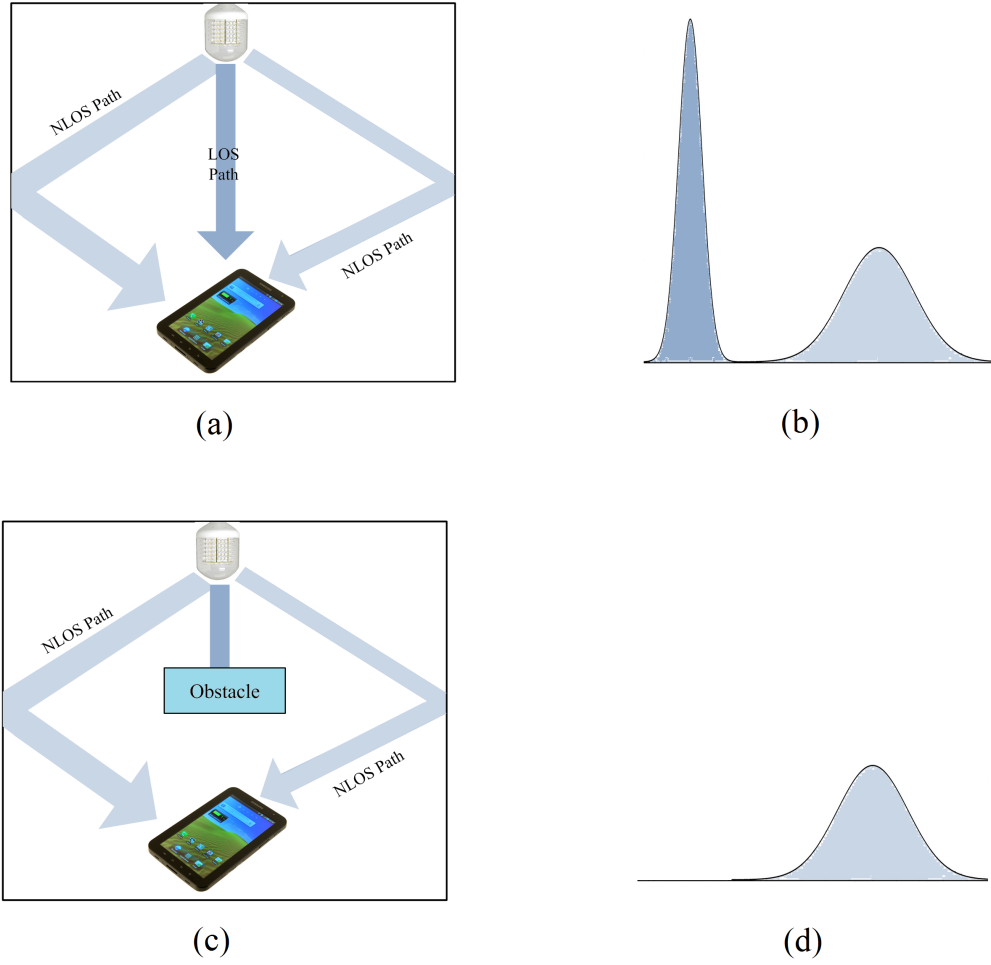
Figure 4.4: (a) A VLC system that receives data from both LOS and NLOS paths, and (b) its corresponding impulse response. (c) Shadowing effect in VLC when the direct path is blocked, and (d) the impulse response in the shadowing case.

4.2   Modulation for VLC

In VLC systems, white LED are used as sources, and modulation schemes that can be used in these systems are limited. Optical frequency division multiplexing (OFDM) and PPM have been proposed for indoor wireless communications [54]. OFDM is a spectrally efficient technique able to provide high-speed data transmission in dispersive communication systems. The application of OFDM to VLC systems with white LEDs is presented in [64]. For a practical systems, the nonlinearity of the LEDs limits the performance of OFDM [54], and, moreover, the possibility of controlling the PAPR in OFDM systems remains unanswered.

Table 4.1: Different BIBD Codes with Various Weight to Length Ratio

(Q,K,λ)	PAPR (Q/K)	(Q,K,λ)	PAPR (Q/K)
(35,17,8)	2.058	(21,5,1)	4.2
(11,5,2)	2.2	(31,6,1)	5.167
(7,3,1)	2.33	(57,8,1)	7.125
(40,13,4)	3.077	(91,10,1)	9.1
(13,4,1)	3.25	(183,14,1)	13.07
(109,28,7)	3.89	(381,20,1)	19.05

In order to achieve a data-rate higher than 100 Mbits/s with these LEDs, appropriate coding and modulation must be used. Modified forms of OFDM have been used to achieve a high-speed transmission [61]. In [65] discrete multitone (DMT) OFDM is used to modulate a trichromatic LED with a bandwidth of 180 MHz; for a illumination of 320 lx, data-rates of 397 Mbit/s, 132 Mbit/s and 171 Mbit/s are reported for the red, green and blue channels, respectively. PPM is another alternative to modulate white LEDs in indoor wireless systems [66], [67]. PPM is an appealing modulation scheme for optical communications since it requires simple transmitter/receiver structures and is easy to implement. However, it introduces several weaknesses in free-space optical systems, such as low PAPR and low spectral efficiency. To alleviate these weaknesses, generalized forms of PPM have been proposed to improve its performance in optical systems. Overlapped-PPM (OPPM) is used to increase the data-rate of PPM in communication systems with bandwidth limited sources [68]. The application of OPPM to VLC systems is discussed in [67], where it is also used in combination with PWM to satisfy the average power constraint.

In this chapter we use EPPM to modulate trichromatic LEDs. EPPM is introduced in Section 3.2 as an alternative technique to PPM to improve the performance of peak-power limited communication systems. We propose to modulate each of the spectral components of a trichromatic LED independently, and at the receiver side we use three photo-detectors to detect the three modulated signals.

Let $\mathbf{s}_k = (s_{k1}, s_{k2}, \ldots, s_{kQ}) \in \{\mathbf{c}_1, \mathbf{c}_2, \ldots, \mathbf{c}_Q\}$ be the symbol sent in the kth symbol-time. The signal transmitted by the LED has intensity proportional to $\sum_k \sum_{j=1}^{Q} s_{kj} p(t - kT_s - jT_s/Q)$, where T_s is the symbol time and $p(t)$ is the transmit pulse shape.

One of the advantages of EPPM for application in indoor optical wireless systems is its capability of controlling the PAPR. The PAPR of a (Q,K,λ)-EPPM is Q/K, and this ratio can be controlled by choosing an appropriate BIBD code. There are a vast number of BIBD families with various code-weight to code-length ratios, and they provide a broad range of dimming levels. Table 4.1 lists Q/K ratios for some known BIBD codes [1] with PAPR larger than 2. The complement of a (Q,K,λ)-BIBD code is also a BIBD code, with PAPR of $Q/(Q-K)$, and thus these can be used to achieve a PAPR smaller than 2.

In Section 3.3, a multilevel form of EPPM is introduced, and four different modulation schemes are proposed that have a significantly larger spectral efficiency than EPPM due to their large symbol cardinality. Two of these schemes, called type-I multilevel EPPM (MEPPM) and type-II MEPPM, use BIBD codewords to build symbols, and also have a PAPR of Q/K. Therefore, similar to EPPM, the PAPR can be controlled in these schemes by using different BIBD codes.

4.3 Detection and Demodulation

At the receiver, one photodetector is used for each wavelength. An integrate and dump filter is used to sample the received signal after photodetection. Let $\mathbf{r}_k = (r_{k1}, r_{k2}, \ldots, r_{kQ})$ be the received photon-count in the Q time-slots of symbol k. We assume that given a sampling period T_s/Q, the VLC channel has an equivalent discrete impulse-response of h_ℓ, for $\forall \ell \in \mathbb{Z}$, including the effects of the bandwidth-limited transmit pulse-shape and the diffuse multipath channel for a given geometry, calculated from $p(t) * h(t)$. The output of the decoder looks like PPM, and hence, the same analysis as for PPM can be used for EPPM.

In indoor VLC systems, due to the short distance between transmitter and receiver, the received power is high, and hence, the receiver is shot noise limited. We show that for ideal nondispersive channels the receiver in Figure 3.5 is optimum for shot noise limited Poisson-distributed systems with a fixed background light. Letting $h_0 = 1$ and $h_j = 0$ for $j \neq 0$, the mean of the received photon-count in symbol-time k can be written as $E\{\mathbf{r}_k\} = \Lambda_0 \mathbf{s}_k + \Lambda_b$ in the symbol-time k, where Λ_0 is the total received photoelectron-count from the lighting source in one time-chip, Λ_b is the received photoelectron-count due to the background radiation in one time-chip. The received photoelectron-count can be expressed as $\Lambda_0 = \eta \frac{P_0}{h\upsilon} \frac{T_s}{Q}$, where P_0 is the peak received power, h is Planck's constant, υ is the central optical frequency, and η is the efficiency of the photodetector.
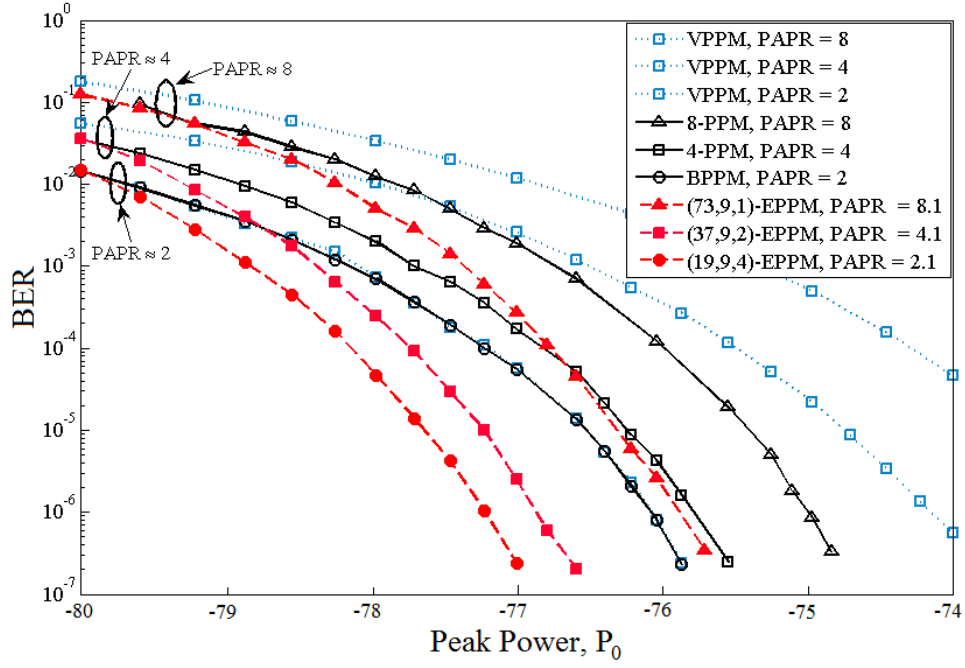
Figure 4.5: Simulated BER versus the received peak power, P_0, for EPPM and PPM for different PAPRs.

Then the symbol decision in symbol-time k, $\hat{m}_k$, using maximum likelihood (ML) is

$$\hat{m}_k = \arg \max_{1 \leq m \leq Q} \Pr(\mathbf{r}_k | \mathbf{s}_k = \mathbf{c}_m)$$

$$= \arg \max_{1 \leq m \leq Q} \left(\sum_{j=1}^{Q} r_{kj} \log(c_{mj}\Lambda_0 + \Lambda_b) - \sum_{j=1}^{Q} (c_{mj}\Lambda_0 + \Lambda_b) \right). \tag{4.1}$$

Because of the fixed weight of the EPPM symbols, $\sum_{j=1}^{Q} c_{mj} = K$, and, since $c_{mj} \in \{0, 1\}$, the ML decoder reduces to

$$\hat{m}_k = \arg \max_{1 \leq m \leq Q} \sum_{j=1}^{Q} r_{kj} c_{mj}. \tag{4.2}$$

As a result, the correlation receiver is the optimum decoder for EPPM in shot-noise limited Poisson-distributed systems.

The simulated bit error rates (BER) of EPPM and PPM are compared in Figure 4.5 for a PAPR of 2, 4 and 8 at a bit-rate of 200 Mbits/s for a single color assuming a rectangular transmitted pulse-shape (ideal LED) and an ideal VLC channel without ISI. The shot noise is assumed to be the dominant noise, and the background light is set to 0.1 μW. According to these results, for
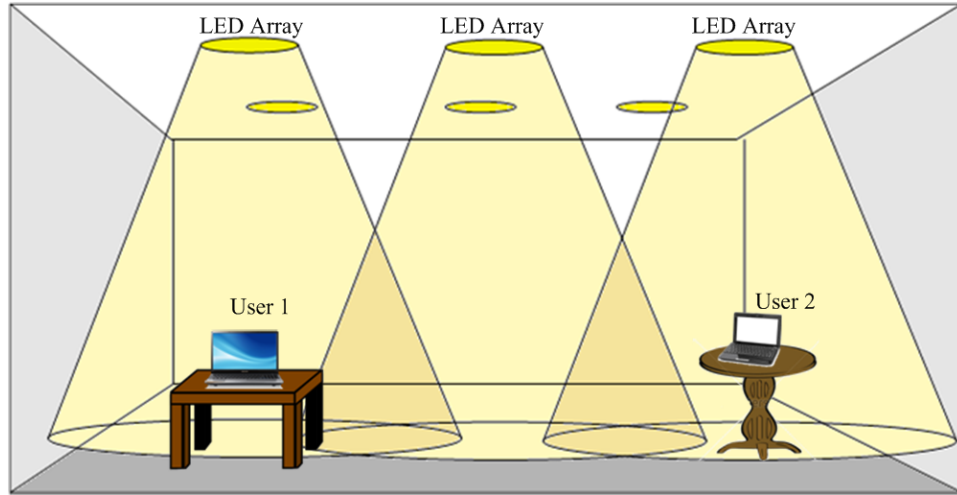
Figure 4.6: The configuration of a VLC network with LED arrays and two users.

peak-power limited systems, the performance of EPPM surpasses that of PPM for all three PAPR levels, since it transmits more than one pulse in each symbol period.

4.4 Multiple Access for Indoor Optical Networks

Visible light communications (VLC) is an appealing technology for network access in indoor environments since it is immune to radio-frequency (RF) interference, has low impact on human health, and is able to provide high data-rate connection [54]. It is proposed as an alternative to WiFi to provide high-speed access for tablets, phones, laptops and other devices in many indoor spaces, such as offices, homes, airplanes, hospitals and convention centers.

Indoor optical networks must be able to provide simultaneous access for multiple users. OCDMA, which is a networking technique that provides multiple access by assigning binary signature patterns to users [25], can be used to fulfill this need. Among various OCDMA forms that have been proposed, direct-sequence OCDMA is of most interest for indoor VLC system, since it can simply be implemented by turning the LEDs on and off [69]. In this type of OCDMA, binary sequences with special cross-correlation constraints, such as optical orthogonal codes (OOC), are used to encode the data of users in the time-domain [70]. Codewords of an OOC are binary sequences that meet a given correlation constraint [71]. The application of OOCs to VLC networks requires codes with a wide range of parameters for different dimming levels, which may not be practical for a network with a fixed number of users.

The downlink configuration of a VLC system is shown in Figure 4.6, where arrays of white LEDs are used as sources. Here, we consider LED arrays as access points, and we assume that all LED arrays in a room are synchronous and transmit the same data. For each user, usually the strongest received power is the one that corresponds to the signal received from the direct path of the closest LED array, and therefore, it is considered as the main signal and the main data source. In situations where the direct path to the main source is blocked, the data can be retrieved using the multipath signals received from non-line-of-sight (NLOS) paths. In this work, VLC is assumed to be used only for the downlink, and another independent system, such RF or infrared (IR) communications, is used for the lower data-rate uplink channel to avoid self-interference from the full-duplex communication.

In VLC systems, since the access points are illumination sources and are the same for all users, synchronous OCDMA techniques can be used for the downlink. In [69], synchronous time-spreading OCDMA using optical orthogonal codes (OOC) and on-off keying (OOK) was studied. For this case, because of the bandwidth limit of LEDs and the long length of OOCs needed, the data-rate for each user is limited. An efficient technique to increase the data-rate in OOC-based OCDMA systems is M-ary modulation using cyclic shifts of the OOC codewords, which is called code cycle modulation (CCM) in [72]. In this modulation, any cyclic shift of an OOC codeword with length L_{ooc} is considered as a symbol, and therefore, the bit-rate is increased by a factor of $\log_2 L_{\text{ooc}}$. This technique is highly susceptible to synchronization errors.

A limitation of using OOCs in VLC systems is their incompatibility with the dimming feature. For a CCM OCDMA system that uses an OOC with length L_{ooc} and weight w, the PAPR is L_{ooc}/w. Furthermore, for an OOC code with length L_{ooc}, weight w, and cross-correlation α, the number of codewords, which is equal to the number of users, N_{U}, is bounded by the Johnson bound [71]

$$N_{\text{U}} \leq \left\lfloor \frac{1}{w} \left\lfloor \frac{L_{\text{ooc}} - 1}{w - 1} \left\lfloor \frac{L_{\text{ooc}} - 2}{w - 2} \ldots \left\lfloor \frac{L_{\text{ooc}} - \alpha}{w - \alpha} \right\rfloor \ldots \right\rfloor \right\rfloor \right\rfloor. \tag{4.3}$$

Changing the pulse duty-cycle is not possible for bandwidth-limited sources, while changing the pulse amplitude requires a complex tuner circuit due to the source nonlinearity. Therefore, in an OCDMA network with a given number of users, changing the PAPR requires employing a new OOC code, which, considering (4.3), may not be possible for low PAPRs. As an example, for a PAPR of 2, we should have $L_{\text{ooc}} = 2w$, which implies that $a > w^2/L_{\text{ooc}} = w/2$ and corresponds only to systems with large N's. Codes with these parameters are not only difficult and highly
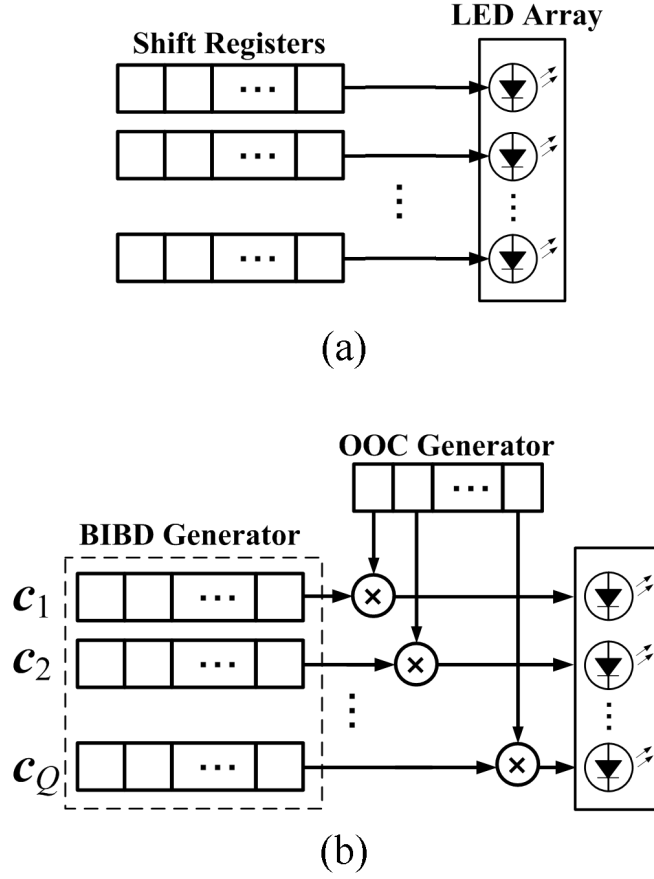
Figure 4.7: Transmitter structure and symbol generation using shift registers for (a) MEPPM, and (b) coded-MEPPM.

complicated to design, but also have high interference collision probability and poor performance. Furthermore, to change either the number of user or the dimming level it is necessary to change the OOC code, which requires a large database of OOC codes.

In this section, two networking methods based on MEPPM are introduced in order to not only provide multiple access for different users in an indoor VLC network, but also provide M-ary transmission for each user so that a higher data-rate can be achieved.

4.4.1 Networking Using Coded-MEPPM

OOCs are used in OCDMA networks to provide simultaneous access for users by assigning signature pattern to each user [71]. In our proposed technique that we call coded-MEPPM (C-MEPPM), we combine OOCs with MEPPM to provide multi-access and high data-rate for each user. Un-

like traditional OCDMA systems where OOCs are applied in the time domain, in our approach the OOC codewords are implemented in the code domain, and are applied on the codewords of a BIBD code in code-space.

Let $\mathbf{e}_n = [e_{n1}, e_{n2}, \ldots, e_{nL_{\mathrm{OOC}}}]$, $n = 1, 2, \ldots, N_{\mathrm{U}}$, $e_{n\ell} \in \{0, 1\}$, be the nth codeword of an OOC with length L_{OOC}, weight w, and cross-correlation α. By assigning the nth OOC codeword to user n and assuming N_{U} active users, its transmitted signal for the mth symbol in the M-ary constellation is given by

$$\mathbf{u}_{m,n} = \frac{1}{N_{\mathrm{U}} w} \sum_{\ell=1}^{L} e_{n\ell} \, \mathcal{S}(\mathbf{c}_\ell, m). \tag{4.4}$$

where $\mathcal{S}(\mathbf{c}_\ell, m)$ denotes the mth cyclic shift of vector $\mathbf{c}_\ell$. In this manner, the symbols of user n are cyclic shifts. The factor $\frac{1}{N_{\mathrm{U}} w}$ in (4.4) guarantees a PAPR of Q/K for LED arrays. From (4.4), the length of the OOC should be no longer than the number of BIBD codewords, i.e., $L_{\mathrm{OOC}} \leq Q$. In this work, for a fixed Q we use an OOC with $L_{\mathrm{OOC}} = Q$, since the larger the OOC-length, the higher performance it can achieve. Figure 4.7(b) shows the transmitter structure using shift-registers for coded-MEPPM. To illustrate the concept, Figure 4.8 shows the multilevel symbol generated using a (13,3,1) OOC codeword and a (13,4,1) BIBD code. The first four symbols of CCM-OCDMA using the OOC codeword and coded-MEPPM described in Figure 4.8 are shown in Figure 4.9. Note that CCM-OCDMA is two-level while C-MEPPM is multilevel.

Using the C-MEPPM technique, the dimming level can be controlled by changing the BIBD code as discussed in Section 4.2, and the maximum number of users can be increased by switching the OOC code. Therefore, a significantly smaller code database is needed compared to the case when only OOCs are used for networking in VLC systems.

4.4.2 Optimum Single-User Decoder for Shot-Noise Limited Scenario

In a VLC system, due to the short range of the channel, the received power is usually high, and therefore, the system is limited by shot-noise. In Section 4.3 we show that the optimum decoder for EPPM in a shot-noise limited regime is a correlation receiver, and hence, C-MEPPM symbols can be decoded using two successive shift registers. Both consider a single-user environment ignoring the multiple-access interference. Here we obtain the optimum receiver for coded-MEPPM when the system performance is limited by shot-noise where we consider the mean of the interference as a constant background light, since considering it as a modulated signal would require a multiuser detector. Hence, the optimum decoder for user n assuming a background photon-count of $\Lambda_b' =$
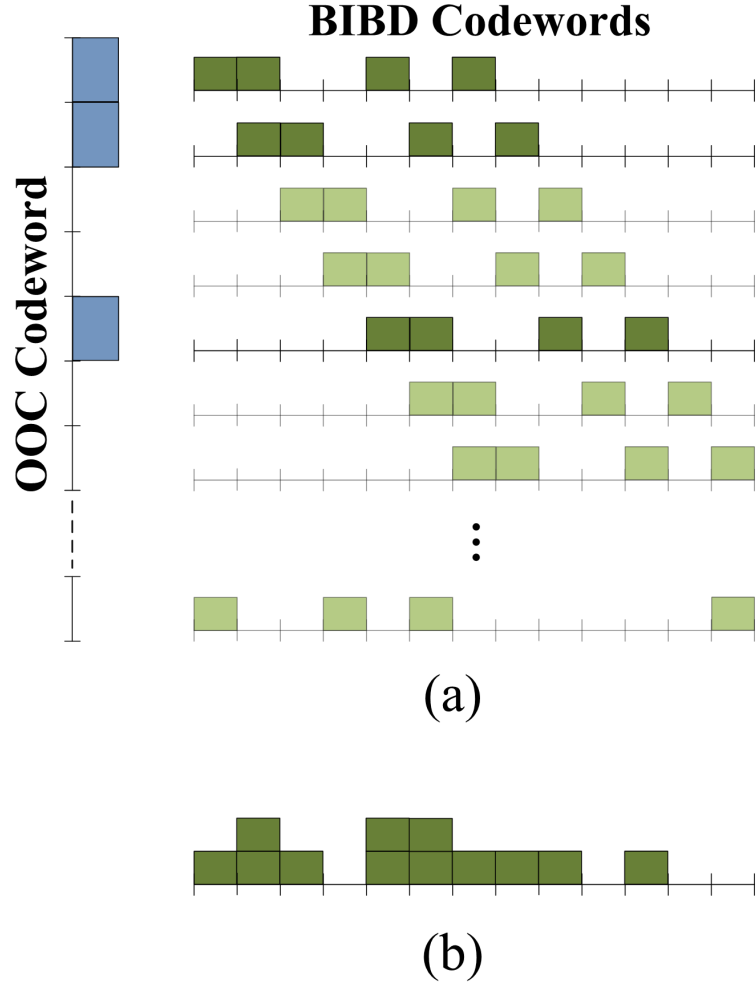
Figure 4.8: (a) Symbol generation for coded-MEPPM using the (1100100000000) OOC codeword and a (13,4,1)-BIBD, and (b) resulting symbol.

$\Lambda_b + \frac{N_U - 1}{N_U Q} \Lambda_0 K$ in each time-slot is

$$\hat{m}_k = \arg \max_{1 \le m \le Q} \left(\sum_{j=1}^{Q} r_{kj} \log \left(\Lambda_0 \mathbf{u}_{m,n}(j) + \Lambda_b' \right) - \sum_{j=1}^{Q} \left(\Lambda_0 \mathbf{u}_{m,n}(j) + \Lambda_b' \right) \right). \qquad (4.5)$$

where $\mathbf{u}_{m,n}(j)$ is component j of vector $\mathbf{u}_{m,n}$. Considering that both OOC and BIBD are fixed-weight codes, the optimum decoder can be simplified to

$$\hat{m}_k = \arg \max_{1 \le m \le Q} \left(\sum_{j=1}^{Q} r_{kj} \log \left(N_U \mathbf{u}_{m,n}(j) + N_U \frac{\Lambda_b}{\Lambda_0} + (N_U - 1) \frac{K}{Q} \right) \right). \qquad (4.6)$$

Defining $\mathbf{v}_n := (v_{1,n}, v_{2,n}, \ldots, v_{Q,n})$ as

$$v_{j,n} := \log\left(\frac{1}{w}\sum_{\ell=1}^{L_{\text{OOC}}} e_{n\ell}c_{\ell j} + N\frac{\Lambda_b}{\Lambda_0} + (N_{\text{U}} - 1)\frac{K}{Q}\right), \tag{4.7}$$
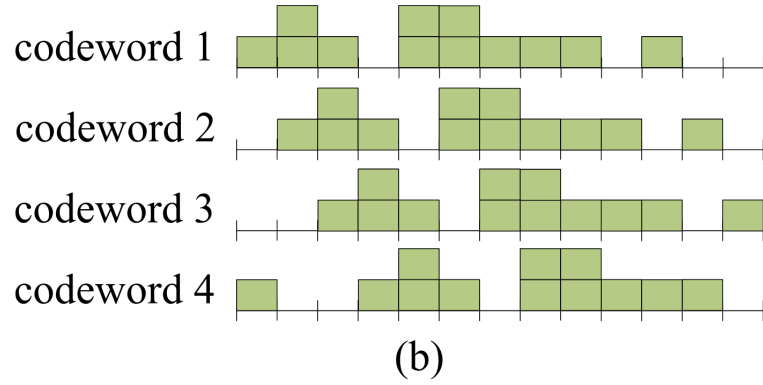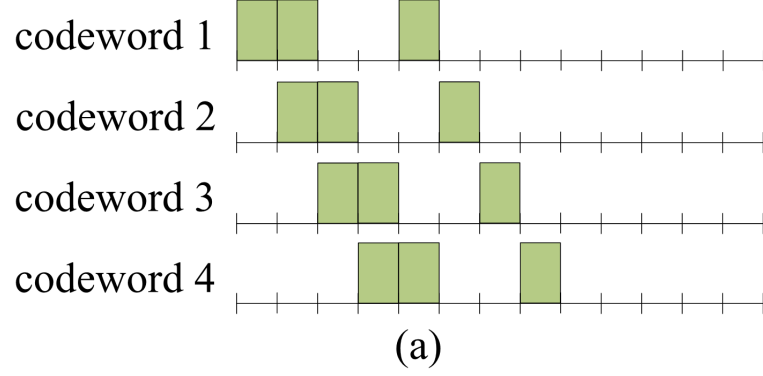
Figure 4.9: First four symbols of one user for (a) CCM-OCDMA using the (1100100000000) OOC codeword, and (b) coded-MEPPM using the same OOC codeword and the (13,4,1)-BIBD shown in Figure 4.8
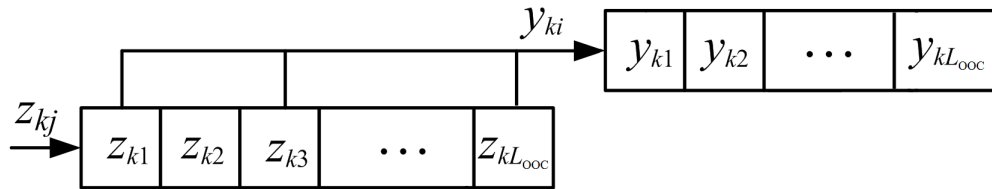
Figure 4.10: OOC decoder using two shift registers.
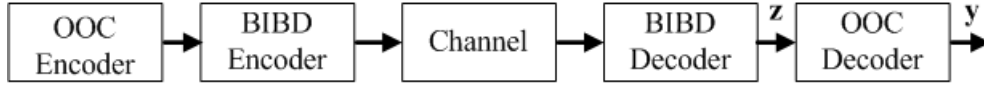
Figure 4.11: Schematic view of a code-MEPPM system using OOC.

for $j = 1, 2, \ldots, Q$ and $n = 1, 2, \ldots, N_{\mathrm{U}}$, the optimum detector for user n can be written as

$$\hat{m}_k = \arg \max_{1 \leq m \leq Q} \langle \mathbf{r}_k, \mathcal{S}(\mathbf{v}_n, m) \rangle, \tag{4.8}$$

and therefore, the optimum single-user decoder is also a correlation detector that can be implemented using a shift-register. To implement this, at the receiver side a BIBD-correlator (Figure 3.5) is followed by a OOC-correlator (Figure 4.10) to decode the received signal. The output vector of the OOC-correlation decoder, $(y_{k1}, y_{k2}, \ldots, y_{kL_{\mathrm{OOC}}})$, resembles the received signal of an CCM-OCDMA system using OOC. The decision is made in favor of the symbol that has the largest corresponding output of the OOC-decoder, i.e.,

$$\hat{m}_k = \arg \max_{1 \leq m \leq L_{\mathrm{OOC}}} y_{km}. \tag{4.9}$$

4.4.3 Error Probability for Correlation Receiver

We derive an approximate mathematical expression for the error-probability of this receiver. The performance of the receiver can be evaluated in three cases: 1) Shot noise limited case, 2) weak MAI scenario, and 3) strong MAI. For the first case we consider a high SNR regime and calculate an upper bound on the symbol error probability. For the second and third cases, MAI is the main limiting factor, and the effect of the shot-noise is less important. Therefore, the performance of C-MEPPM is similar to CCM-OCDMA, and the analytical error probability presented in [72] can be used to calculate the BER. For $\alpha = 1$, which corresponds to the weak interference case, the approximation given in [72] is not accurate. In order to get a more accurate analysis for this scenario, we model the interference as a Bernoulli trial, which has binomial distribution.

For the first case, without loss of generality we assume that the desired user is user 1 and it transmit $\mathbf{s}_{k,1}$ at symbol-time k. The overall system using OOC and MEPPM encoders and decoders is depicted in Figure 4.11. Then the symbol error probability, P_s, is bounded by

$$P_s \leq \sum_{m_1=1}^{Q} \Pr(\mathbf{s}_{k,1} = \mathbf{u}_{m_1,1}) \sum_{m' \neq m_1} \Pr(y_{km'} > y_{km_1} | \mathbf{s}_{k,1} = \mathbf{u}_{m_1,1}), \tag{4.10}$$

85

which derived using the union bound. Here,

$$y_{km'} - y_{km_1} = \sum_{j=1}^{Q} r_{kj} \Big(\sum_{\ell=1}^{L_{\text{OOC}}} e_{1\ell}(c_{(m'\oplus\ell)j} - c_{(m_1\oplus\ell)j}) \Big), \qquad (4.11)$$

and, since r_{kj}'s are Poisson distributed random variables, $y_{km'} - y_{km_1}$ is the sum of weighted Poisson random variables, and according to [73], its probability distribution function (pdf) can be approximated by a Gaussian distribution. For an equiprobable transmission,

$$\Pr(y_{km'} > y_{km_1} | \mathbf{s}_{k,1} = \mathbf{u}_{m_1,1}) =$$
$$\frac{1}{L_{\text{OOC}}^{N_{\text{U}}-1}} \sum_{m_2=1}^{L_{\text{OOC}}} \cdots \sum_{m_{N_{\text{U}}}=1}^{L_{\text{OOC}}} \Pr\Big(y_{km'} > y_{km_1} | \mathbf{s}_{k,n} = \mathbf{u}_{m_n,n}, n = 1, \ldots, N_{\text{U}} \Big).$$
$$(4.12)$$

Given that $\mathbf{s}_{k,n}$ is transmitted for user n, $n \in \{1, 2, \ldots, N_{\text{U}}\}$, in symbol-time k, the mean value of the output of the OOC-correlator that matches the OOC-codeword $\mathbf{e}_1$ in symbol-time k, $y_{km'}$ $i = 1, 2, \ldots, L_{\text{OOC}}$, is

$$E\Big\{ y_{km'} \Big| \mathbf{s}_{k,n} = \mathbf{u}_{m_n,n}, n = 1, 2, \ldots, N_{\text{U}} \Big\} =$$
$$\Big(\frac{\Lambda_0 K}{N_{\text{U}} w} \Big) \langle \mathcal{S}(\mathbf{e}_1, m_1), \mathcal{S}(\mathbf{e}_1, m') \rangle + \underbrace{\Big(\frac{\Lambda_0 K}{N_{\text{U}} w} \Big) \sum_{n=2}^{N_{\text{U}}} \langle \mathcal{S}(\mathbf{e}_n, m_n), \mathcal{S}(\mathbf{e}_1, m') \rangle}_{\text{MAI}}. \quad (4.13)$$

In high SNR regimes, an approximate value can be calculated for $\Pr(y_{km'} > y_{km_1} | \mathbf{s}_{k,1} = \mathbf{u}_{m_1,1})$ by only considering the largest terms in (4.12) which correspond to smallest $E[y_{km_1} - y_{km'} | \mathbf{s}_{k,1} = \mathbf{u}_{m_1,1}]$'s. On the other hand, $E[y_{km_1} - y_{km'} | \mathbf{s}_{k,1} = \mathbf{u}_{m_1,1}]$ takes its minimum value for the symbols m' that satisfies $\langle \mathcal{S}(\mathbf{e}_1, m_1), \mathcal{S}(\mathbf{e}_1, m') \rangle = 0$ and $\langle \mathcal{S}(\mathbf{e}_1, m_1), \mathcal{S}(\mathbf{e}_n, m') \rangle = \alpha$, $n = 2, \ldots, N_{\text{U}}$. For each n at most w^2/α m''s exists that satisfies the above two conditions. Defining $\alpha_{ij} := \langle \mathcal{S}(\mathbf{e}_1, i), \mathcal{S}(\mathbf{e}_1, j) \rangle$, in the worst case we have

$$E[y_{km_1} - y_{km'} | \mathbf{s}_{k,1} = \mathbf{u}_{m_1,1}] \geq \Big(\frac{\Lambda_0 K}{N_{\text{U}} w} \Big) (w - \alpha_{m_1 m'} + \alpha - \alpha N_{\text{U}}), \qquad (4.14)$$

and this is minimized when $\alpha_{m_1 m'} = \alpha$. Define

$$\mu := \max E[y_{km_1} - y_{km'} | \mathbf{s}_{k,1} = \mathbf{u}_{m_1,1}] = \Big(\frac{\Lambda_0 K}{N_{\text{U}} w} \Big) (w - \alpha N_{\text{U}}). \qquad (4.15)$$

The variance of $y_{km_1} - y_{km'}$ can be calculated as

$$\mathrm{Var}\big[y_{km'} - y_{km_1} | \mathbf{s}_{k,1} = \mathbf{u}_{m_1,1}\big]$$

$$= \sum_{j=1}^{Q} \mathrm{Var}[r_{kj}]\Big(\sum_{\ell=1}^{L_{\mathrm{OOC}}} e_{1\ell}(c_{(m'\oplus\ell)j} - c_{(m_1\oplus\ell)j})\Big)^2$$

$$= \sum_{j=1}^{Q} \frac{\Lambda_0}{N_{\mathrm{U}}w} \sum_{n=1}^{N_{\mathrm{U}}} \sum_{\ell'=1}^{L_{\mathrm{OOC}}} e_{n\ell'} c_{(\ell'\oplus m_n)j}\Big(\sum_{\ell=1}^{L_{\mathrm{OOC}}} e_{1\ell}(c_{(m'\oplus\ell)j} - c_{(m_1\oplus\ell)j})\Big)^2 \qquad (4.16)$$

The maximum of $\mathrm{Var}\big[y_{km'} - y_{km_1} | \mathbf{s}_{k,1} = \mathbf{u}_{m_1,1}\big]$ can be written as follows

$$\sigma^2 := \max \mathrm{Var}\big[y_{km'} - y_{km_1} | \mathbf{s}_{k,1} = \mathbf{u}_{m_1,1}\big]$$

$$= \Lambda_0 2\lambda w(w-1) + \mu. \qquad (4.17)$$

Assuming a high SNR regime, we get

$$P_s \leq \frac{L-1}{2}\mathrm{erfc}\Big(\frac{\mu}{\sigma}\Big). \qquad (4.18)$$

where erfc(.) is the Gaussian error function. This approximation is not valid when $\alpha N < w$ since in that case $E[y_{km_1} - y_{km'}]$ can be smaller than zero, which means $\Pr(y_{km'} > y_{km_1} | \mathbf{s}_{k,1} = \mathbf{u}_{m_1,1})$ becomes close to 1. This corresponds to the second and third cases, where MAI is the main limiting factor.

As mentioned before, for the second scenario we use a Bernoulli model to approximate the symbol error probability. In this model the probability that a pulse from an interfering users overlaps with one of the pulses of symbol m' and not with any pulses from symbol m_1 is $p := w(w-\alpha)/L$. Hence, $\Pr(y_{km'} > y_{km_1} | \mathbf{s}_{k,1} = \mathbf{u}_{m_1,1})$ can be written as

$$\Pr(y_{km'} > y_{km_1} | \mathbf{s}_{k,1} = \mathbf{u}_{m_1,1}) =$$

$$\sum_{j=0}^{N_{\mathrm{U}}-w} \binom{N_{\mathrm{U}}-1}{j} p^j (1-p)^{N_{\mathrm{U}}-1-j}$$

$$\times \sum_{i=w-1+j}^{N_{\mathrm{U}}-1} \binom{N-1}{i} p^i (1-p)^{N_{\mathrm{U}}-1-i}, \qquad (4.19)$$

which, for $p \ll 1$, becomes

$$\Pr(y_{km'} > y_{km_1} | \mathbf{s}_{k,1} = \mathbf{u}_{m_1,1}) \approx$$

$$\binom{N_{\mathrm{U}}-1}{w-1} p^{(w-1)} (1-p)^{(N_{\mathrm{U}}-w)}. \qquad (4.20)$$
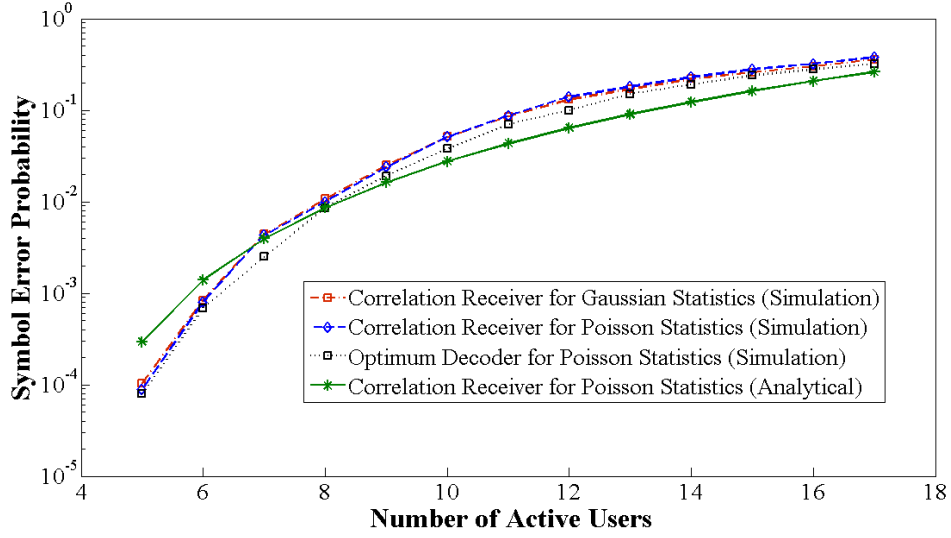
Figure 4.12: BER versus the number of active interfering users for optimum detector from (4.8) for Poisson statistics, and correlation receiver for both Poisson and Gaussian statistics. (4.18) and (4.21) are used for analytical result.

As mentioned before, at most w^2 symbols of user 1 can have a cross-correlation of 1 with symbol m_1. Thus,

$$P_e \approx w^2 \binom{N_U - 1}{w - 1} p^{(w-1)} (1 - p)^{(N_U - w)}. \tag{4.21}$$

The simulated BERs of the correlation receiver in Figure 4.7 with different statistics and the optimum detector derived in (4.8), and also the analytical BER expression from (4.21) are plotted in Figure 4.12 versus the number of active users, N, for a coded-MEPPM using a (341,5,1)-OOC code [71] and a (341,85,21)-BIBD [2], which can support up to 17 simultaneous users. In these results, both the background light power and the peak received power are assumed to be $0.1 \, \mu W$, and the data is assumed to be transmitted using ideal LEDs with central wavelength of 650 nm at a bit-rate of 200 Mb/s through an ideal channel. According to these results, the BER of the optimum detector is slightly lower than that of the correlation receiver. According to this figure, the Gaussian approximation for the statistics of the received photoelectron count has a good accuracy, and the simulated BERs of the correlation receiver for the Poisson and Gaussian statistics are shown to be close. As it can be seen, the analytical results calculated in this section provide good approximations to the BER of this C-MEPPM system.

88

4.4.4 Networking Using Divided-MEPPM

In the second proposed technique, which we call divided-MEPPM (D-MEPPM), the generating BIBD code is divided into several smaller codes, and a different set of codes is assigned to each user. Then, similar to the MEPPM scheme, each user uses its codeword set to generate multilevel symbols. Let q_n be the number of BIBD codewords that are assigned to user n, such that $q_1 + q_2 + \cdots + q_N = Q$, and let $\mathcal{C}_n$, $|\mathcal{C}_n| = q_n$, be the set of codewords that are assigned to user n, such that $\mathcal{C}_n \cap \mathcal{C}_m = \emptyset$ for any $n \neq m$, and $\mathcal{C}_1 \cup \mathcal{C}_2 \cup \cdots \cup \mathcal{C}_N = \{\mathbf{c}_1, \mathbf{c}_2, \ldots, \mathbf{c}_Q\}$. This can be considered as a kind of CDMA, where distinct codeword sets with cross-correlation λ are assigned to users. Using this definition, user n can utilize an ℓ_n-branch MEPPM, $1 \leq \ell_n < q_n$, for M-ary transmission using $\mathcal{C}_n$. It can use either MEPPM type-I or type-II, yielding a constellation of size $\binom{q_n}{\ell_n}$ for type-I and $\binom{q_n+\ell_n}{\ell_n}$ for type-II MEPPM. The symbol m of user n can be expressed as

$$\mathbf{u}_{m,n} = \frac{1}{Q} \sum_{\ell \in \mathcal{C}_{m,n}} \mathbf{c}_\ell, \tag{4.22}$$

where $\mathcal{C}_{m,n}$ is the set of ℓ_n codewords assigned to symbol m of user n. As discussed in Section 3.3, for type-I MEPPM, all ℓ_n elements of $\mathcal{C}_{m,n}$ are distinct, and for type-II, a codeword can be repeated more than once in $\mathcal{C}_{m,n}$. The smallest distance between two symbols of user n is $\Lambda_0 2(K - \lambda)/w$. Each user can generate these symbols using the transmitter shown in Figure 4.7-(a).

An advantage of this networking technique over the one presented in Section 4.4.1 is its potential to provide different data-rates for different users, which can be done by assigning unequal size subsets to users. Thus, we provide a larger number of BIBD codewords to users requiring a higher bit-rate. Table 4.2 shows different allocation of codewords in a VLC network with 5 users. Data-rates of users can be changed by assigning code sets with different sizes. In case (a) a (63,31,15) BIBD code which has a PAPR of 2 is used to connect 5 users, and in case (b) this is done using a (57,8,1) BIBD code which has a PAPR of 7.125.

Similar to the C-MEPPM case, an analytical expression for the BER can be calculated for D-MEPPM. Without loss of generality we calculate the symbol error probability for the first user given that $\mathbf{s}_{k,n} = \mathbf{u}_{m_n,n}$ is sent for user n. In this case, the variance of z_{ki} is

$$Var\{z_{ki}\} = \sum_{i=1}^{Q} c_{ij} Var\{r_{kj}\} + \Gamma^2 \sum_{i=1}^{Q} (1 - c_{ij}) Var\{r_{kj}\}$$

$$= \sum_{i=1}^{Q} c_{ij} E\{r_{kj}\} + \Gamma^2 \sum_{i=1}^{Q} (1 - c_{ij}) E\{r_{kj}\}. \tag{4.23}$$

Table 4.2: Different Allocation of Codewords to Provide Different Data-rates in a VLC Network

(a)

User	1	2	3	4	5
Number of Codes	13	13	13	12	12
Data Rate (Mb/s)	26	26	26	24	24
Number of Codes	21	21	7	7	7
Data Rate (Mb/s)	43.3	43.3	13.3	13.3	13.3
Number of Codes	35	9	9	5	5
Data Rate (Mb/s)	73.7	17.6	17.6	9.2	9.2

(b)

User	1	2	3	4	5
Number of Codes	12	12	11	11	11
Data Rate (Mb/s)	26.5	26.5	24.1	24.1	24.1
Number of Codes	18	18	7	7	7
Data Rate (Mb/s)	40.7	40.7	14.8	14.8	14.8
Number of Codes	33	8	8	4	4
Data Rate (Mb/s)	76.6	17.1	17.1	7.8	7.8

Since $\mathcal{C}_{m_n,n}$'s are distinct sets we have

$$Var\{z_{ki}\} = \frac{\Lambda_0}{N}\Big[(\ell_1 - n_1 + \ell_2 + \ldots \ell_N)(\lambda + \Gamma^2(k - \lambda)) + n_j K\Big]. \tag{4.24}$$

Here we approximate $Var\{z_{ki}\}$ with $\Lambda_0(\ell_1 + \ldots \ell_N)(\frac{\lambda K}{K-\lambda}) + \frac{(K-2\lambda)K}{K-\lambda}$, and we use the following expressions to approximate the BER

$$P_b \approx M' \operatorname{erfc}\left(\sqrt{\frac{(K - \lambda)^2 \Lambda_0/N}{(\ell_1 + \ldots \ell_N)\lambda K + (K - 2\lambda)K}}\right). \tag{4.25}$$

where $M' = \frac{\ell_1(q_1 - \ell_1)}{8}$ for type-I and $M' = \frac{\ell_1 q_1^2 (q_1-1)^2}{8(q_1+\ell_1)(q_1+\ell_1-1)(q_1+\ell_1-2)}$ for type-II.

4.5   Numerical Results

In this section numerical results using the analytical BER expression derived above are presented to compare the performance of the proposed networking techniques to each other, and also to that of a CCM-OCDMA system. Figure 4.13 compares the BER of a CCM-OCDMA system using

a (101,25,7)-OOC to that of the coded-MEPPM using a (101,11,2)-OOC and (101,25,6)-BIBD for different number of active users up to 10 users. For both systems, the PAPR is 4 and the constellation size is 101. Since the parameters of an OOC should satisfy $\alpha > w^2/F$ [71], for a CCM-OCDMA with $L = 101$ and $w = 25$, $\alpha = 7$ is the smallest cross-correlation that can be chosen. For C-MEPPM, the BIBD code is chosen to satisfy the PAPR condition, and OOC is chosen to provide the lowest collision probability between users. As shown in the figure, C-MEPPM can achieves lower BERs compared to CCM-OCDMA. Similarly, for all PAPRs the best OOC with a given length can be employed to minimize the MAI effect. In Figure 4.13, the BER of a CCM-OCDMA using (83,41,21)-OOC is compared to that of a C-MEPPM using (83,41,20)-BIBD and a (83,15,3)-OOC for different number of active users up to 13 users, and the C-MEPPM is shown to have a better performance compared to the latter one.

A comparison between the analytical BER of the coded-MEPPM using a (63,31,15)-BIBD and a (63,9,2)-OOC, and divided-MEPPM using the same BIBD code is shown in Figure 4.14. In this figure the BER is plotted versus the number of users for three different peak received power levels and for a PAPR of 2. For C-MEPPM, a (63,31,15)-BIBD code is used to construct the symbols, and a (63,31,15)-OOC is used to encode the users' data. On the other hand, for divided-MEPPM, distinct sets of 4 BIBD codewords are assigned to users, and therefore, the maximum
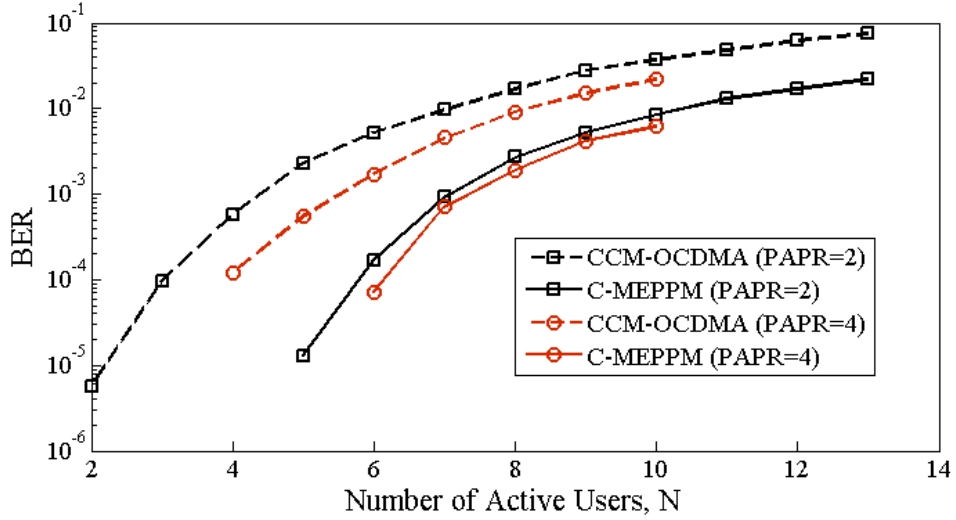
Figure 4.13: A comparison between the BERs of C-MEPPM and CCM-OCDMA versus the number of active users for PAPR of 2 and 4, peak received power $P_0 = 0.1\,\mu W$ and background power $P_b = 0.1\,\mu W$.
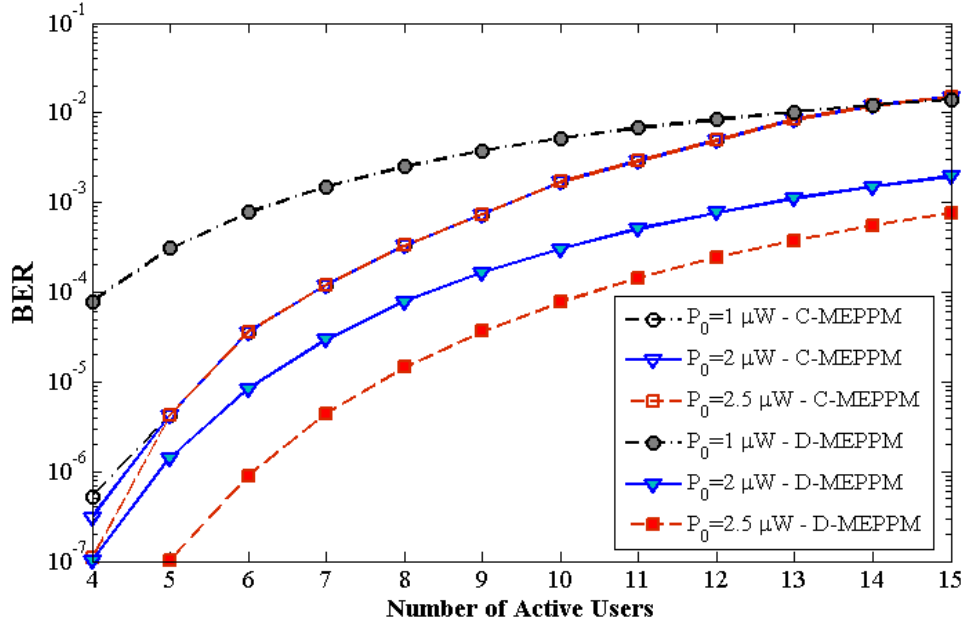
Figure 4.14: BER versus the number of active interfering users for coded-MEPPM (C-MEPPM) and divided-MEPPM (D-MEPPM) with different peak power levels for $\eta = 0.8$, central wavelength $\lambda = 650$ and background power $P_b = 0.1\ \mu W$.

number of users is again 16. For this technique, each user utilizes 4-level type-II MEPPM and has 70 symbols. According to these results, for weak peak powers the error probability of coded-MEPPM is lower than divided-MEPPM since it has larger distance between its symbols and its performance is only limited by multiple access interference (MAI), while the performance of divided-MEPPM is limited by the shot noise.

4.6   Summary

In this chapter EPPM and MEPPM are proposed to be used in VLC systems. They are shown to have the potential to support a variety of PAPRs, which corresponds to a wide range of dimming levels. The correlation receiver is shown to be the optimal single-user detector. Two multiple-access methods, are introduced and compared. The first method, using both OOC and BIBD codes to encode the user data, is shown to have a large distance between symbols. Despite CCM-OCDMA systems, the parameters of the OOC that is used in C-MEPPM can be chosen independent from the given PAPR, and hence, C-MEPPM is able to provide a lower BER compared to

CCM-OCDMA when MAI is the dominating factor. The second technique only uses BIBD codes to construct MEPPM symbols, and, therefore, can have a large constellation size and consequently high bit-rate for each user. It is also able to provide flexible and unequal data-rates to users. According to the numerical results, for low SNR cases the coded-MEPPM technique achieves a lower BER compared to divided-MEPPM, while the latter is preferred in high SNR regimes since it has a lower MAI effect.

Chapter 5

Approaches for Band-limited Sources and Channels

In this chapter, we propose techniques to provide high-speed communications for systems with restricted channel or source bandwidth. Interleaving is applied on EPPM, MEPPM and coded-QPSK to reduce the interference between the adjacent time-slots in dispersive channels and increase the data-rate. A lower bound is presented to show the performance limit of the best interleaver. Overlapping the pulses in EPPM, MEPPM and coded-QPSK can provide high transmission-rates for band-limited sources such as LEDs.

5.1   Increasing Data-Rate in Band-limited Channels

In a dispersive channel each pulse is broadened over its neighboring time-slots, and causes interference, as shown in Figure 5.1 for an indoor visible light communication system. In mildly dispersive channels, the main interference on a symbol is caused by its own pulses. Therefore, and for mathematical simplicity, we ignore the interference between adjacent symbol-times here. Also for mathematical convenience, we use cyclic shifts of transmitted vectors instead of their right shifts in our analysis. With these assumptions, ignoring the background light and given symbol $\mathbf{s}_k$ is sent, the mean of the received photoelectron-count at symbol-time k is approximated by the vector $\Lambda_0 \sum_\ell h_\ell \mathcal{S}(\mathbf{s}_k, \ell)$, where $\Lambda_0 = \eta \frac{P_0}{h\upsilon} \frac{T_s}{Q}$, P_0 is the peak received power, υ is the optical frequency, η is the efficiency of the photodetector.

Given codeword $\mathbf{c}_m$ is sent, in the absence of noise and background light, a signal proportional
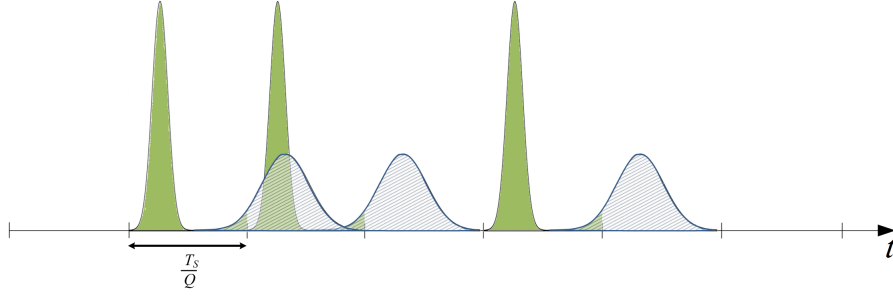
Figure 5.1: Received signal in a dispersive VLC indoor channel. Solid colored areas are the main received signals, and shaded areas are interference signals.

to $\sum_\ell h_\ell \mathcal{S}(\mathbf{c}_m, \ell)$ is received at the output of the channel. Since the symbols of EPPM are cyclic shifts, $\mathcal{S}(\mathbf{c}_m, \ell) = \mathbf{c}_{m+\ell}$, and hence, the received signal can be represented as $\sum_\ell h_\ell \mathbf{c}_{m+\ell}$. This means that the expected jth output of the decoder, z_{kj}, in Figure 3.5 ignoring background light is

$$E\{z_{kj}|\mathbf{s}_k = \mathbf{c}_m\} = \Lambda_0 \left(\left\langle \mathbf{c}_j, \sum_\ell h_\ell \mathbf{c}_{m+\ell} \right\rangle - \Gamma \left\langle \overline{\mathbf{c}_j}, \sum_\ell h_\ell \mathbf{c}_{m+\ell} \right\rangle \right)$$

$$= \Lambda_0 K h_{m-j}. \tag{5.1}$$

Thus the distance between adjacent symbols decreases at the output of the channel and this increases the error probability.

Instead of relying on an equalizer at the receiver, in this work we propose techniques to reduce the ISI effect, and increase the minimum distance in dispersive channels. We propose two solutions to diminish the interference effect. In both of the proposed techniques, the interference effect is spread over the all symbols in order to achieve a larger minimum distance.

5.1.1 Codes with Non-Fixed Cross-Correlation

Figure 5.2 illustrates the distance between symbols with and without temporal dispersion. The first solution that we propose to deal with this problem is to use codes with non-fixed cross-correlation instead of BIBD codes. As shown in Figure 5.3, a code that has a smaller cross-correlation for adjacent codewords is less vulnerable to ISI compared to BIBD codes. In order to find the optimum cross-correlation pattern $\{\lambda_1, \lambda_2, \ldots, \lambda_{Q-1}\}$, the distances between the symbols at the output of the channel need to be calculated for a given channel response, $\underline{\mathbf{h}}$, in terms of $\lambda_1, \lambda_2, \ldots, \lambda_{Q-1}$, and then a minimax problem has to be solved.

This solution is not efficient since finding optimum $\lambda_1, \lambda_2, \ldots, \lambda_{Q-1}$ for a given channel response $\underline{\mathbf{h}}$ is time-consuming. Moreover, finding codes from the cross-correlation pattern $\{\lambda_1, \lambda_2,$
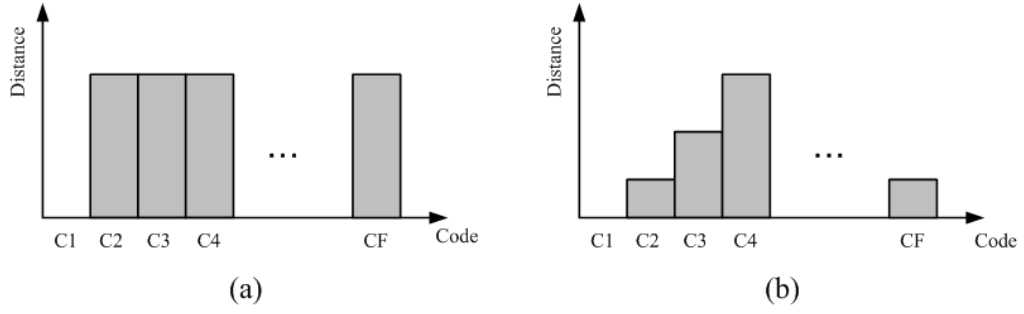
Figure 5.2: Illustration of the Euclidean distance between the first symbol and other symbols in (a) a non-dispersive channel, and (b) a dispersive channel.
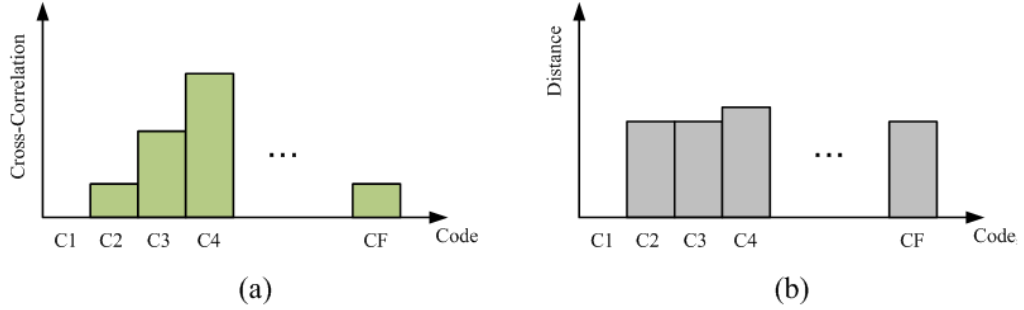
Figure 5.3: (a) The cross-correlation between the first codeword and other codewords of a code with non-fixed cross-correlation pattern, and (b) the Euclidean distance between the symbols of that code in a dispersive channel.

$\ldots, \lambda_{Q-1}\}$ requires complicated optimization, and even the existence problem of a code for a given cross-correlation pattern is unknown. The other problem with this solution is its dependance on the channel response, $\underline{h}$, which may change over the time, and therefore, a large set of codes is needed to have the an acceptable performance. These problems led us to the another approach, which is significantly more efficient than the first one.

5.1.2 Interleaving

The second solution is based on the idea that non-cyclic codes have better performances in dispersive channels. Interleaving is introduced here as a technique to improve the performance of EPPM in multipath channels, which makes EPPM an appealing alternative to PPM for dispersive communication systems.

96
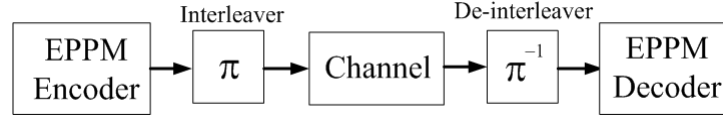
Figure 5.4: Schematic view of a EPPM system using interleaver and de-interleaver for dispersive channels.
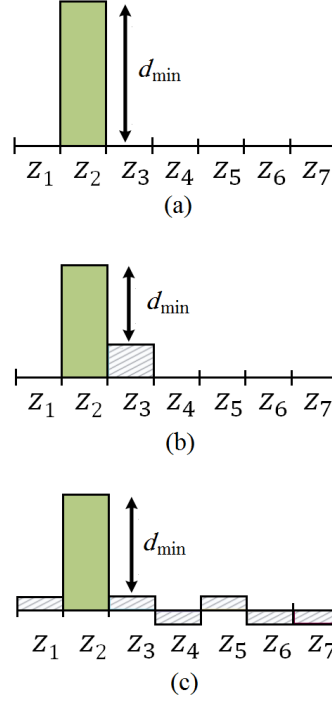
Figure 5.5: The decoded signal and the minimum distance between symbols, $d_{\min}$, for (a) ideal channel, and dispersive channels (b) without interleaver, and (c) with interleaver.

An interleaver and deinterleaver can be used in the transmitter and receiver to diminish the impact of ISI, as shown in Figure 5.4. This interleaver can be considered as a permutation matrix, π, with element (i, j) denoted as π_{ij}, and the deinterleaver would be its inverse, π^{-1}. So $\mathbf{c}_m \pi$ is transmitted instead of $\mathbf{c}_m$, i.e., the transmitted pulses in the EPPM symbol are rearranged. The code-length and code-weight of a (Q,K,λ)-EPPM after the interleaver remain as Q and K, respectively, and hence, the interleaver does not change the PAPR. At the receiver side, the inverse of the permutation matrix is applied on the received vector and then the decoder in Figure 3.5 is used to decode the received signal. Thus, in a noiseless non-dispersive channel, the output of the channel is $\mathbf{c}_m \pi$, and $\mathbf{c}_m \pi \pi^{-1} = \mathbf{c}_m$ is sent to the EPPM decoder.

Now let us consider the performance of this technique in dispersive channels. Still assuming

$\mathbf{c}_m$ is transmitted, in this case the noiseless output of the channel is proportional to $\sum_\ell h_\ell \mathcal{S}((\mathbf{c}_m \pi), \ell)$, and $h_0 \mathbf{c}_m + \sum_{\ell \neq 0} h_\ell \mathcal{S}((\mathbf{c}_m \pi), \ell) \pi^{-1}$ is sent to the EPPM decoder. Therefore, the expected value of the jth output of the decoder is

$$E\{z_{kj}|\mathbf{s}_k = \mathbf{c}_m\} = \Lambda_0 \left(h_0 K \delta_{jm} + (1+\Gamma) \sum_{\ell \neq 0} h_\ell \left(\langle \mathbf{c}_j, \mathcal{S}((\mathbf{c}_m \pi), \ell) \pi^{-1} \rangle - K \right) \right), \quad (5.2)$$

where

$$\delta_{jm} = \begin{cases} 1 & ; j = m, \\ 0 & ; j \neq m \end{cases} . \tag{5.3}$$

Figure 5.5 shows the output of the decoder for both ideal (Figure 5.5-(a)) and dispersive channels (Figure 5.5-(b)), and the effect of the interleaver on the decoded signal. In this example, the tail of the received pulses due to the channel interferes with one symbol, and, therefore, the minimum distance between decoded signals is considerably reduced compared with the dispersionless case. Adding an interleaver spreads the interference over all symbols, as shown in Figure 5.5-(c), and hence, the minimum distance between decoded signals is increased.

The same interleaver/deinterleaver technique can also be used for multilevel-EPPM to increase the minimum distance between MEPPM symbols in dispersive channels. In Section 3.3, MEPPM is shown to achieve higher spectral-efficiencies compared to EPPM due to its larger constellation size, and thus, longer symbol-time. Hence, interleaved MEPPM can achieve an even-lower error probability in bandwidth-limited channels.

According to Section 3.2, the demodulator in Figure 3.5 computes $\hat{m}_k = \arg \max_{1 \leq m \leq Q} z_{km}$. Defining $d_{mj} := E\{(z_{km} - z_{kj})|\mathbf{s}_k = \mathbf{c}_m\}$, we assume that the error probability between symbols m and j can be expressed as $f(d_{mj})$, where $f(.)$ is a monotonically decreasing function. Then the symbol error probability can be approximated by

$$P_s \approx \frac{1}{Q} \sum_{m=1}^{Q} \sum_{\substack{j=1 \\ j \neq m}}^{Q} f(d_{mj}). \tag{5.4}$$

Therefore, in high signal to noise (SNR) regimes, we can write $P_s \simeq M_{d_{\min}} f(d_{\min})/Q$, where $d_{\min} := \min_{m \neq j} d_{mj}$ and $M_{d_{\min}}$ is the number of (m, j) pairs with $d_{mj} = d_{\min}$.

The optimal permutation matrix that minimizes the symbol error probability is the one that not only maximizes $d_{\min}$, but also minimizes $M_{d_{\min}}$. We first calculate a lower bound on P_s of interleaved EPPM, and then use binary linear programming (BLP) to find the best arrangement for the interfering pulses for a given channel. Note that the optimum permutation matrix for an

EPPM scheme with a given BIBD code may not be optimum for multilevel-EPPM that uses the same BIBD code.

In order to find the best interleaver for a given channel impulse response, let $B_{i,j} := \sum_{\ell \neq 0} h_\ell A_{i,j,\ell}$, for $\forall i, j$, and $b_{\max} = \max_{i,j} B_{i,j}$. According to (5.6), the optimum π is the one that: 1) minimizes $b_{\max}$ (i.e., maximizes $d_{\min}$), and 2) minimizes $\left| \{ B_{i,j} = b_{\max} | 1 \leq i, j \leq Q \} \right|$ (i.e., minimizes $M_{d_{\min}}$). To find the optimum π, we solve two successive BLPs, with the same constraints but with different objective functions. In the first BLP, the goal is to minimize $b_{\max}$, and then in the second BLP we minimize $\left| \{ B_{i,j} = b_{\max} | 1 \leq i, j \leq Q \} \right|$. In both programs, the sum of elements in each row and each column is set to 1 as equality constraints. The variables must also satisfy the following quadratic inequality constraint for $\forall m, j$:

$$\mathbf{c}_m \, \pi \, \mathbf{I}' \, \pi^{\mathrm{T}} \, (\mathbf{c}_j - \mathbf{c}_m)^{\mathrm{T}} \leq b_{\max}, \tag{5.5}$$

where $\mathbf{I}' = \sum_{\ell} h_\ell \mathbf{I}_\ell$. These binary quadratic constraints can be reduced to binary linear constraints by representing cross products by binary variables as explained in [74, pp. 67]. This introduces new linear constraints involving new and old variables.

Lower Bound on the Error Probability of Interleaved EPPM

Letting $A_{j,m,\ell} = \left\langle \mathbf{c}_j, \left(\mathcal{S}((\mathbf{c}_m \pi), \ell) \pi^{-1} \right) \right\rangle$,

$$d_{mj} \propto h_0 K - (1 + \Gamma) \sum_{\ell \neq 0} h_\ell \left(A_{j,m,\ell} - A_{m,m,\ell} \right), \; m \neq j. \tag{5.6}$$

Thus maximizing $d_{\min}$ is equivalent to minimizing $\max_{m,j} \sum_{\ell \neq 0} h_\ell (A_{j,m,\ell} - A_{m,m,\ell})$. To obtain a lower bound on P_s, we minimize $\max_{m,j} (A_{j,m,\ell} - A_{m,m,\ell})$ for each $\ell \neq 0$. To this end, we rewrite $A_{j,m,\ell}$ as $A_{j,m,\ell} = (\mathbf{c}_m \pi) \mathbf{I}_\ell (\mathbf{c}_j \pi)^{\mathrm{T}}$, where $\mathbf{I}_\ell$ is the ℓth right cyclic shift of the identity matrix. We can then define the $Q \times Q$ matrix $\mathbf{A}_\ell$ with (j, m) element equal to $A_{j,m,\ell}$, which can be represented as

$$\mathbf{A}_\ell = \mathbf{C} \, \pi \, \mathbf{I}_\ell \, \pi^{\mathrm{T}} \, \mathbf{C}^{\mathrm{T}}, \tag{5.7}$$

where $\mathbf{C}$ is the code matrix with mth row equal to $\mathbf{c}_m$, for $m = 1, 2, \ldots, Q$. We first prove the following lemma which is then used to derive constraints on the elements of $\mathbf{A}_\ell$.

Lemma: Let π be a permutation matrix, and define $\mathbf{P}_\ell := \pi \, \mathbf{I}_\ell \, \pi^{\mathrm{T}}$. Then the diagonal elements of $\mathbf{P}_\ell$ are all zeros for $\ell \neq 0$.

Proof: $\mathbf{P}_\ell$ is clearly also a permutation matrix. Let p_i and π_i, $i = 1, 2, \ldots, Q$, denote the positions of the '1' in the ith row of $\mathbf{P}_\ell$ and π, respectively. Therefore, $\mathbf{P}_\ell = \pi \, \mathbf{I}_\ell \, \pi^{\mathrm{T}}$ implies that $\pi_{p_i} = \pi_i + 1$, and therefore $p_i \neq i$ (the diagonal elements of $\mathbf{P}_\ell$ are zero). ∎

In order to calculate a lower bound on P_s, we prove the following theorem.

Theorem: The following three constraints hold for $A_{j,m,\ell}$'s:

(i) $\sum_{j=1}^{Q} A_{j,m,\ell} = K^2$ and $\sum_{m=1}^{Q} A_{j,m,\ell} = K^2$,

(ii) $\sum_{m=1}^{Q} A_{m,m,\ell} = \lambda Q$.

Proof: For (i), using (1.2) we obtain

$$\sum_{j=1}^{Q} A_{j,m,\ell} = \left\langle \sum_{j=1}^{Q} \mathbf{c}_j, \left(\mathcal{S}((\mathbf{c}_m \pi), \ell) \pi^{-1} \right) \right\rangle = K^2, \tag{5.8}$$

and similarly for the summation over the second index. To prove (ii), the sum of diagonal elements in $\mathbf{A}_\ell$ can be written as

$$\sum_{m=1}^{Q} A_{m,m,\ell} = \sum_{m=1}^{Q} \mathbf{c}_m \mathbf{P}_\ell \mathbf{c}_m^{\mathrm{T}}$$

$$= \mathbf{c}_1 \left(\sum_{m=1}^{Q} \mathbf{I}_m \, \mathbf{P}_\ell \, \mathbf{I}_m^{\mathrm{T}} \right) \mathbf{c}_1^{\mathrm{T}}, \tag{5.9}$$

since $\mathbf{c}_m = \mathbf{c}_1 \mathbf{I}_\ell$. As $\mathbf{P}_\ell$ is a permutation matrix, $\mathbf{T} := \left(\sum_{m=1}^{Q} \mathbf{I}_m \, \mathbf{P}_\ell \, \mathbf{I}_m^{\mathrm{T}} \right)$ is a circulant matrix with first column $(T_1, T_2, \ldots, T_Q)^{\mathrm{T}}$, and $T_1 + T_2 + \cdots + T_Q = Q$. From (1.2), $\sum_{m=1}^{Q} A_{m,m,\ell} = K T_1 + \lambda(T_2 + T_3 + \cdots + T_Q)$, and hence,

$$\sum_{m=1}^{Q} A_{m,m,\ell} = \lambda Q + (K - \lambda) T_1. \tag{5.10}$$

From the Lemma, $T_1 = 0$, and hence, (ii) holds for $A_{m,m,\ell}$'s. ∎

From the Theorem, the ideal interleaver is the one that generates $\mathbf{A}_\ell$'s, $\ell = 1, 2, \ldots, Q - 1$, that have $(K - \lambda)$ nondiagonal elements with value $(\lambda + 1)$ in each row and each column, and the rest of the elements are λ. Hence, a lower bound on P_s is given by

$$P_s \geq (K - \lambda) f \left(\Lambda_0 K \left[h_0 - \frac{1}{K - \lambda} \sum_{\ell \neq 0} h_\ell \right] \right). \tag{5.11}$$

Numerical Results

Although the results above apply to any dispersive channel, in this section we provide numerical results specifically for a VLC system. In all results in this section we make the following assumptions: the VLC system is affected by multipath, shot noise and background noise; the bit rate is fixed to be $R_b = 200$ Mbits/s per color; the best permutation matrix for the interleaver for each code is found using BLP as shown above; simulations use perfect symbol synchronization; no equalizer is used at the receiver; the VLC system receiver is exposed to 0.1 μW of background light.

Performance results using (11,5,2)-EPPM and (19,9,4)-EPPM with and without interleaving are plotted versus the normalized broadening factor, σ/T_b, in Figure 5.6. We use the results of [62], [63] and [75] to simulate $h(t)$, the impulse-response shown in Figure 4.3, where the channel is a combination of LOS and NLOS paths components. The delay between LOS and NLOS responses, τ, is assumed to be small compared to the symbol-time T_s. The energy per bit received via the LOS path is assumed to be 5×10^{-14} J. In this plot, increasing σ is assumed to be caused
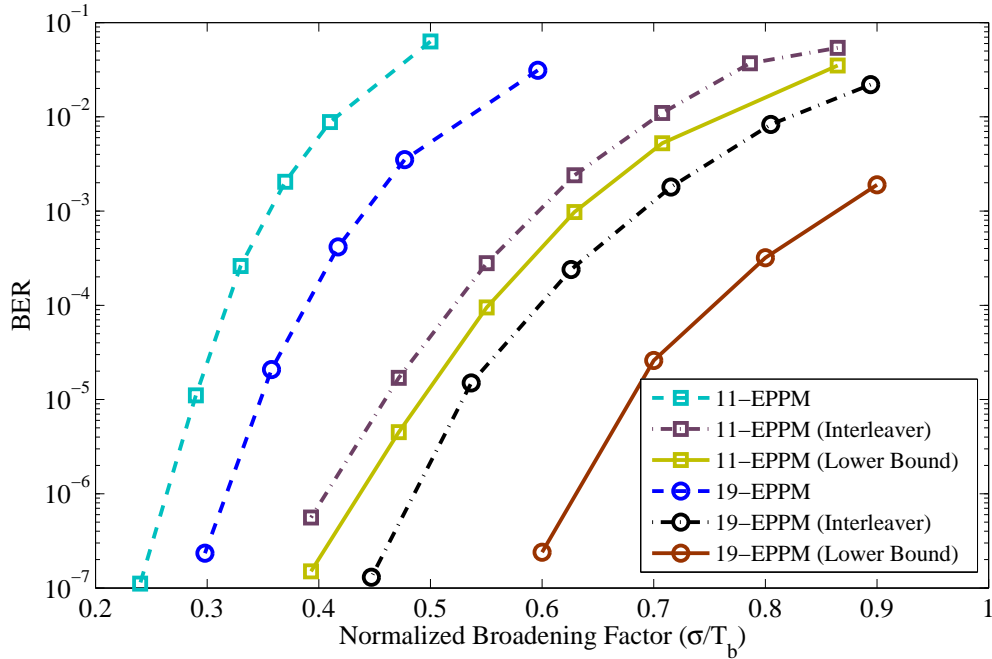
Figure 5.6: Simulated BER vs. normalized broadening factor (σ/T_b) for PPM and EPPM with and without interleaving using (11,5,2) and (19,9,4) BIBD codes in a VLC channel with LOS and NLOS paths.
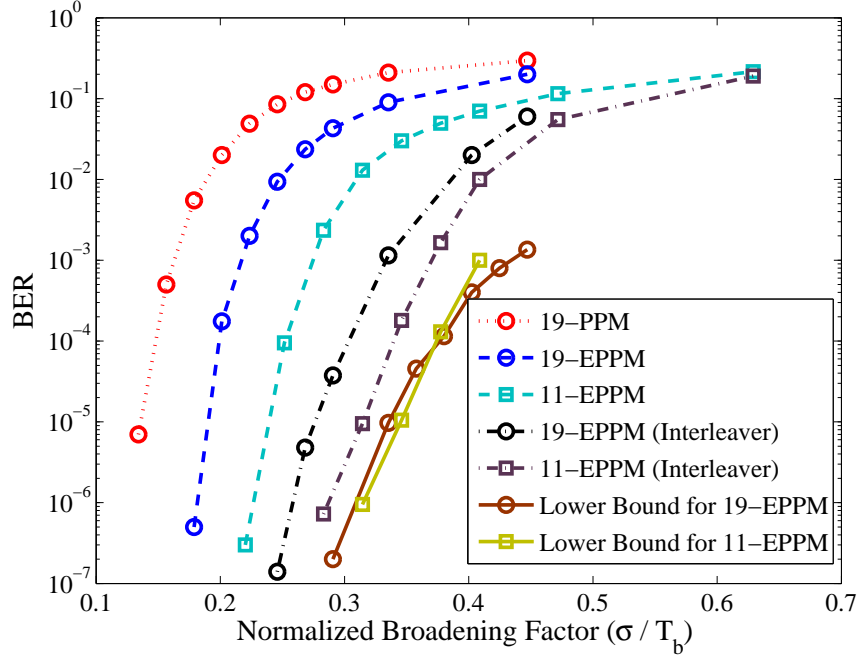
Figure 5.7: Simulated BER vs. normalized broadening factor for PPM and EPPM with and without interleaving using (11,5,2) and (19,9,4) BIBD codes in a VLC channel with blocked LOS path (only NLOS portion of the impulse response).

by increasing the number of reflecting objects and surfaces, and hence, large σ's correspond to stronger interference signals. The NLOS impulse response is approximated by a Gaussian pulse with a fixed peak amplitude, and the peak received power from NLOS path is assumed to be 0.1 μW. This power is equivalent to a NLOS illumination level of 1 lx. Thus, by increasing σ the energy of the multipath signal increases. According to these results, the energy of the interference signal is divided between a larger number of time-chips for a longer code-length, and it therefore achieves a lower BER compared to the a shorter code-length. Moreover, for both codes the BER for EPPM is reduced using an interleaver with a good permutation matrix. Lower bounds on the BER of the interleaved EPPM show the ultimate BERs that can be achieved using interleaving.

Figure 5.7 shows the interleaving effect on the BER of EPPM for a receiver that does not have a LOS path to the LEDs. In this figure the BER is again plotted versus the normalized broadening factor, where the channel is now assumed to have a Gaussian-shaped impulse-response. Here the energy received from the NLOS is assumed to be a constant 5×10^{-14} J as σ increases. According to these results, the BER for EPPM is lower than for PPM with the same length. The lower bound
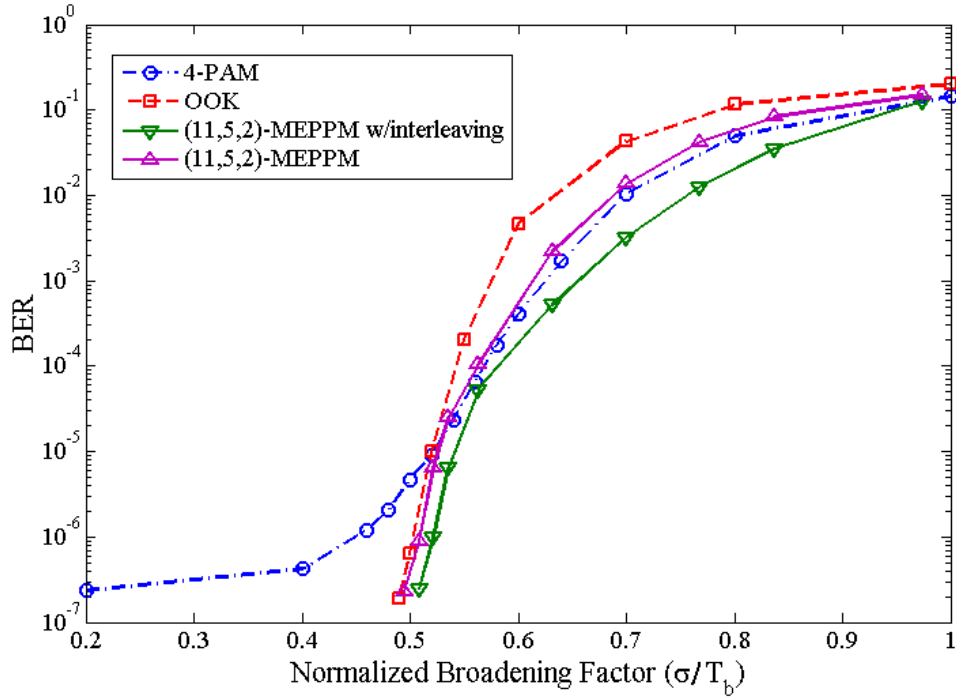
Figure 5.8: Simulated BER vs. normalized broadening factor (σ/T_b) for OOK, 4-ary PAM and 11-level type-II MEPPM with and without interleaving.

is tighter because the interference is less severe than in Figure 5.6.

In Figure 5.8, the BER of 11-level type-II MEPPM using a (11,5,2)-BIBD code is plotted versus normalized broadening factor and compared to on-off-keying (OOK) and 4-ary PPM, assuming the same channel as for Figure 5.6. Although 4-PAM has a better performance for high dispersive channels compared to OOK and MEPPM without interleaving, its BER is large for channels with weaker multipath effect. The BER of MEPPM is improved using interleaving, and its performance surpasses 4-PAM in all cases tried.

The effect of using an interleaver in coded-QPSK is shown in Figure 5.9. In this plot, interleaver is applied on the coded-QPSK that is used in Figure. 3.16. According to these results the performance of coded-QPSK using a good interleaver surpasses that of QPSK in channels with medium and low normalized broadening factors. For the coded-QPSK, the channel causes interference between pulses inside each symbol, which can be considered as intra-symbol interference. Since the symbol time of the coded-QPSK is large, the effect of the intra-symbol interference is larger than the effect of ISI. As a result, when an interleaver and deinterleaver are used at the transmitter and receiver sides, respectively, the intra-symbol interference is spread evenly over the
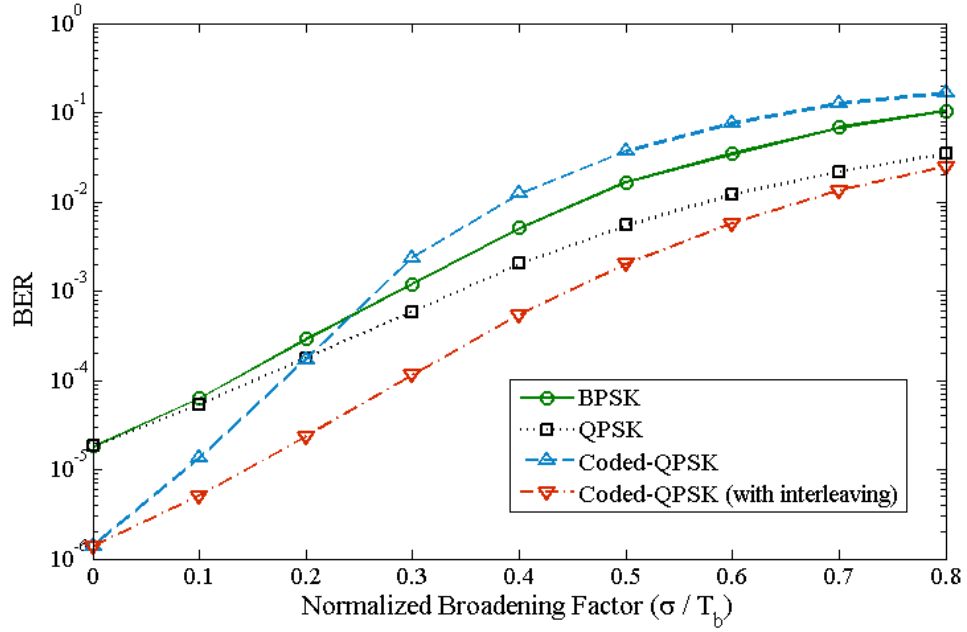
Figure 5.9: Simulation results for BER of a Gaussian dispersive channel versus the normalized broadening factor, σR_b, for QPSK, BPSK, 2^{14}-ary BIBD coded QPSK, and BIBD coded QPSK using an interleaver.

symbol time, and its effect on the error probability is decreased.

5.2 Overlapping Pulses Technique for Bandwidth-Limited Sources

In some FSO systems that use LEDs as sources, LEDs have a long relaxation time, and therefore limit the transmission rate. Overlapped PPM (OPPM) was first proposed for general optical communication systems with bandwidth-limited sources in [68] to increase the data-rate by spreading the pulses over multiple time-chips. OPPM has recently been proposed for indoor VLC application [67], since it can increase the transmission rate of the white LEDs. Using the same idea, we combine the overlapped pulses technique with EPPM in order to increase the symbol-rate in VLC systems. We call the new scheme overlapped EPPM (OEPPM).

In this scheme, we assume that the pulses generated by the LED are v times wider than a time-slot. For an OEPPM scheme that uses a (Q, K, λ)-BIBD code to modulate the symbols, each symbol is divided into $(Q + v - 1)$ equal time-slots, and K pulses with width v are transmitted in each symbol period. Figure 5.10 shows the generation of a OEPPM symbol using a (7,3,1)-

BIBD codeword and overlapping length of $v = 3$. Therefore, an LED array of size 3 is used to generate the OEPPM symbol, and each LED in the array is modeled as a sixth order Bessel filter. The response of each LED to a single rectangular input signal (Figure 5.10-(a)) is shown in Figure 5.10-(b). The first symbol of the OEPPM is shown in Figure 5.10-(d) and is generated by feeding the first codeword of a (7,3,1)-BIBD code (Figure 5.10-(c)) as the input of the LED array of size 3. As shown in Figure 5.10-(d), the rising edges of the optical pulses are determined by the "1"s in the corresponding BIBD codeword. Each color in Figure 5.10-(c) and (d) respectively indicates the input and output of an LED in the array. The distance between two successive "1"s in a BIBD codeword can be smaller than v, and therefore, the OEPPM symbols generated are multi-level signals, where the number of levels is smaller than or equal to $\min(v, K)$. LED arrays can be used to generate multilevel OEPPM symbols, and this modulation scheme can be implemented using at most $\min(v, K)$ pulse-modulated LEDs. For $v > Q$, an LED array with K pulse-modulated LEDs is required to implement OEPPM symbols. In other words each LED in the array is modulated by one pulse of the generating BIBD, and stays on for v time-slots corresponding to its limited bandwidth. The resulting minimum Euclidean distance between transmitted symbols is $\frac{T_{\text{LED}} P_0}{v} \frac{\sqrt{K-\lambda}}{K}$, where P_0 is the peak power of the LED array, and T_{LED} is the LED response time.

The bit-rate of a (Q,K,λ)-OEPPM is the same as for Q-ary OPPM. Given that each color diode of the LED has a response time of T_{LED}, the bit-rate using OEPPM with v overlapping time-slots,
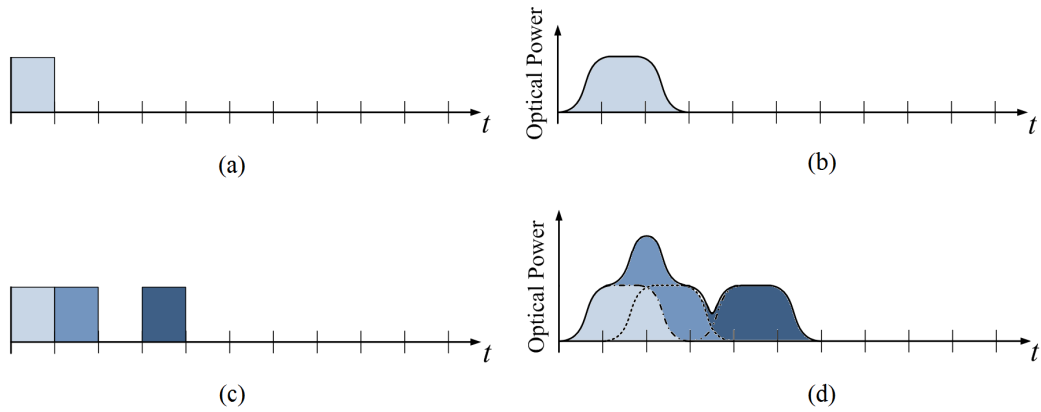
Figure 5.10: (a) A rectangular pulse input, and (b) the corresponding response of an LED with a sixth order Bessel filter model. (c) The first codeword of a (7,3,1)-BIBD code, and (d) its corresponding generated overlapping-EPPM symbol.

per color, is given by

$$R_{b,\text{OEPPM}} = \frac{\log_2 Q}{T_{\text{LED}}} \frac{v}{Q + v - 1}. \tag{5.12}$$

By increasing v the bit-rate increases, up to a limit of $\frac{\log_2 Q}{T_{\text{LED}}}$. Therefore, OEPPM schemes with larger Q's can achieve higher data-rates. Figure 5.11 shows the maximum achievable relative bit-rate, $R_b T_{\text{LED}}$ for $Q = 35$ as a function of v. The corresponding simulated shot-noise-limited BER is also shown. In these results, the peak received power is assumed to be 40 μW, and the LED is modeled as a sixth order Bessel filter with $T_{\text{LED}} = 20$ ns. For these values a bit-rate of 210 Mb/s per color is achievable with a BER of 10^{-3}.

The overlapping-pulse technique can also be utilized with the MEPPM scheme to further increase the data-rate possible with bandwidth-limited LEDs. The bit-rate of type-I and type-II MEPPM schemes utilizing v overlapped pulses are

$$R_{b,\text{OMEPPM-I}} = \frac{\log_2 \binom{Q}{N}}{T_{\text{LED}}} \frac{v}{Q + v - 1}, \tag{5.13}$$

and

$$R_{b,\text{OMEPPM-II}} = \frac{\log_2 \binom{Q+N}{N}}{T_{\text{LED}}} \frac{v}{Q + v - 1}, \tag{5.14}$$

respectively. Accordingly, for a fixed Q and arbitrarily large v, the maximum attainable relative bit-rate, $R_b T_{\text{LED}}$, for each scheme is $\log_2 \binom{Q}{N}$ and $\log_2 \binom{Q+N}{N}$.
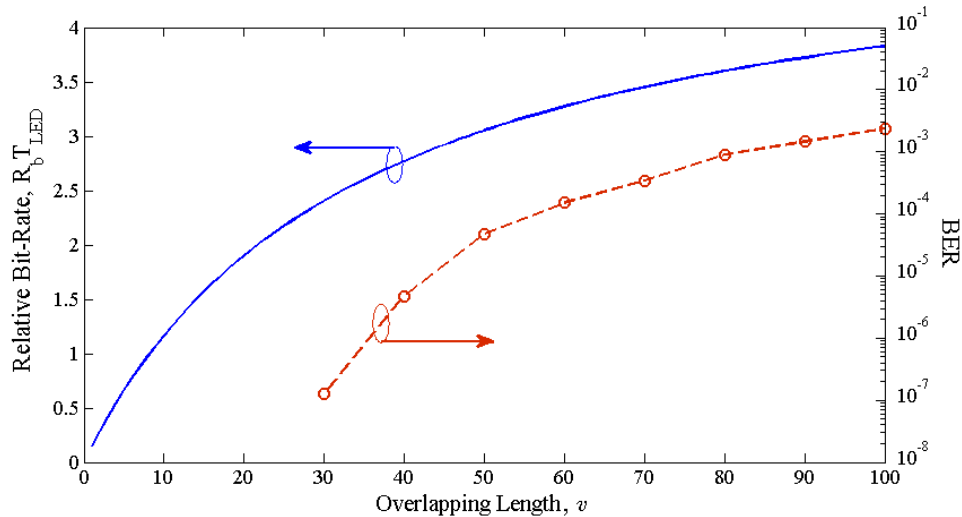
Figure 5.11: The maximum attainable relative bit-rate, $R_b T_{\text{LED}}$ (solid line), for $Q = 35$, and its corresponding simulated BER (dashed line) versus overlapping length, v.

106

We can combine the pulse-overlapping and interleaving for systems with both limited source and channel bandwidths. The pulse-overlapping can increase the data-rate of the transmitter, while interleaving reduces the channel-imposed interference between symbols.

5.3   Summary

Interleaving and overlapping techniques are introduced to increase the bit-rate of EPPM, MEPPM and coded-QPSK in systems with bandwidth-limited channels and sources, respectively. It is shown that applying an interleaver at the transmitter and deinterleaver at the receiver decreases the ISI effect in dispersive channels and increases the minimum distance between symbols. The performance of communication systems using interleaving is studied for a VLC application, where the bit-rate is limited by multipath effect, and interleaving is shown to significantly decrease the BER. An overlapping pulse technique is used to increase the data-rate in communication systems that utilize band-limited sources, such as VLC and NLOS-UV systems where LED arrays with limited modulation bandwidths are used to send the information.

Chapter 6

Open Problems on the Existence of BIBDs

The existence of BIBDs with given parameters is a longstanding problem in combinatorial mathematics. Even for symmetric designs this problem has not been solved. There are some necessary conditions that Q, K and λ must satisfy for the existence of a symmetric design, but these necessary conditions are not sufficient. The most important necessary conditions are $K(K-1) = \lambda(Q-1)$ and the Bruck-Ryser-Chowla condition [1, p.420].

There are many conjectures on the existence of difference-sets, which corresponds to cyclic symmetric BIBDs. Since these designs are used to construct codes and modulation schemes in the previous chapters, these conjectures are of importance in this dissertation. Some of these conjectures are partially proven, but still big portions of them remain unanswered. In this chapter we introduce the main open questions in this area, and then we provide some partial results on Ryser's conjecture. In this chapter, the notations $\mid$ and $\nmid$ are used as follows: for integers x and y, $x|y$ means x divides y, and $x \nmid y$ means the opposite. Also, $x \equiv y \pmod{z}$ denotes that x and y are equal modulo integer z.

6.1   Open Problems and Unanswered Conjectures

Ryser's Conjecture: In 1963 Ryser conjectured a relation between the parameters of a difference-set for the existence of that difference-set. Defining Q, K and λ as length, weight and cross-correlation, respectively, Ryser's conjecture states that there does not exist a (Q, K, λ) difference set when $\gcd(K-\lambda, Q) > 1$. This conjecture has been shown to be true for all known difference

sets.

Prime Power Conjecture: This conjecture states that if a planar abelian difference-set with parameters $(p^2 + p + 1, p, 1)$ exists, then p is a prime power.

Hall's Multiplier Conjecture: For a difference-set with parameters (Q, K, λ), if p is a prime factor of $K - \lambda$, then it is a multiplier of that difference-set.

Cyclic Hadamard Difference-Sets: Golomb and Song conjectured that all difference-sets with parameters $(4n - 1, 2n - 1, n - 1)$ (called cyclic Hadamard difference sets) have a Q either

i) prime

ii) a product of twin primes, i.e., $Q = p(p + 2)$, where p and $p + 2$ are primes

iii) $Q = 2^m - 1$ for some integer m.

Circulant Hadamard Matrices: A circulant Hadamard matrix is an $n \times n$ matrix $\mathbf{H}$ of ± 1's with cyclic symmetry for which $\mathbf{H}\mathbf{H}^{\mathrm{T}} = n\mathbf{I}$. It is conjectured that they exist only for $n = 1$ and 4. Such a matrix is equivalent to a difference set, which must have parameters $(4u^2, 2u^2 \pm u, u^2 \pm u)$. Schmidt showed the only possible counterexamples with $k < 5 \times 10^{10}$ are $u = 11715$ or 82005, and gave a heuristic argument that counterexamples are unlikely.

Barker Sequences: A Barker sequence is a sequence $\{x_1, x_2, \dots, x_Q\}$ of ± 1's for which $\sum\limits_{i=1}^{Q-j} |x_i x_{i+j}| = 1$ for $j = 1, \dots, Q - 1$. Leung and Schmidt showed that there there are no Barker sequences of length $13 < l < 1022$.

6.2 Existence Condition on Cyclic Symmetric BIBDs

In this section we use difference-sets to describe cyclic BIBDs because of mathematical simplicity. Thus, assume that $\{a_1, a_2, \dots, a_K\}$ is the difference-set that corresponds to the BIBD with first codeword $\mathbf{c}_1 = \{c_{11}, c_{12}, \dots, c_{1Q}\}$, where a_i is the position of ith "1" in $\mathbf{c}_1$ and $a_i < a_j$ for $i < j$. The fixed cross-correlation property of the symmetric BIBDs implies that

$$\left| \{(a_i, a_j) | a_j - a_i \equiv t \ (\mathrm{mod}\ Q),\ 1 \le i, j \le K\} \right| = \lambda \quad \text{for } t = 1, 2, \dots, Q - 1. \qquad (6.1)$$

In other words, $\{a_1, a_2, \ldots, a_K\}$ is a difference-set if and only if $(a_j - a_i)$'s and $(Q - a_j + a_i)$'s, $j > i$, covers the set $\boldsymbol{\Lambda}$, which is defined as

$$\boldsymbol{\Lambda} = \Big\{ \underbrace{1, 1, \ldots, 1}_{\lambda}, \underbrace{2, 2, \ldots, 2}_{\lambda}, \ldots, \underbrace{Q-1, Q-1, \ldots, Q-1}_{\lambda} \Big\}. \tag{6.2}$$

Let m and Q be positive integers. We define $S_m(Q)$ as

$$S_m(Q) = 1^m + 2^m + \cdots + (Q-1)^m. \tag{6.3}$$

Let p be a prime factor of Q, then using Faulhaber's formula [76, p. 2334] and according to [77]

$$S_m(Q) \equiv \begin{cases} 0 & \text{for} \quad m \nmid (p-1) \\ -\frac{Q}{p} & \text{for} \quad m | (p-1) \end{cases} \pmod{p}. \tag{6.4}$$

As mentioned before, the fixed cross-correlation property of symmetric BIBDs implies that $(a_j - a_i)$'s and $(Q - a_j + a_i)$'s cover the set $\boldsymbol{\Lambda}$. Therefore, for every integer m, the sum of the elements power $2m$ in both sets are equal, i.e.,

$$\sum_{i=1}^{K-1} \sum_{j=i+1}^{K} (a_j - a_i)^{2m} + \sum_{i=1}^{K-1} \sum_{j=i+1}^{K} \Big(Q - (a_j - a_i) \Big)^{2m} = \lambda \sum_{r=1}^{Q-1} r^{2m}. \tag{6.5}$$

An expanded form of (6.5) is

$$2 \sum_{i=1}^{K-1} \sum_{j=i+1}^{K} (a_j - a_i)^{2m} + \sum_{\ell=1}^{2m} (-1)^\ell \binom{2m}{\ell} Q^\ell \sum_{i=1}^{K-1} \sum_{j=i+1}^{K} (a_j - a_i)^{2m-\ell} = \lambda \sum_{r=1}^{Q-1} r^{2m}. \tag{6.6}$$

By expanding and rewriting the first term in the left hand side, we get

$$2K \Big(\sum_{i=1}^{K} a_i^{2m} \Big) + (-1)^m \binom{2m}{m} \Big(\sum_{i=1}^{K} a_i^m \Big)^2 + 2 \sum_{n=1}^{m-1} (-1)^n \binom{2m}{n} \Big(\sum_{i=1}^{K} a_i^n \Big) \Big(\sum_{i=1}^{K} a_i^{2m-n} \Big)$$
$$+ \sum_{\ell=1}^{2m} (-1)^\ell \binom{2m}{\ell} Q^\ell \sum_{i=1}^{K-1} \sum_{j=i+1}^{K} (a_j - a_i)^{2m-\ell} = \lambda \sum_{r=1}^{Q-1} r^{2m}. \tag{6.7}$$

Any (Q, K, λ) difference-set $\{a_1, a_2, \ldots, a_K\}$ should satisfy (6.7) for all integers m. Also any integer solution that satisfies (6.7) for all m is a difference-set. Therefore, (6.7) is a necessary and sufficient condition for the existence of a difference-set. We use this equation to derive partial results in the next sections.

As an example, we find the difference-set $\{a_1, a_2, a_3\}$ with parameters $(7,3,1)$ by solving (6.7). Without loss of generality we assume that $a_1 = 1$. For these parameters, (6.7) for $m = 1$ and 2

becomes

$$6(1 + a_2^2 + a_3^2) - 2(1 + a_2 + a_3)^2 + 14(2a_3 - 2) + 49 = 21, \tag{6.8}$$

$$6(1 + a_2^4 + a_3^4) + 6(1 + a_2^2 + a_3^2)^2 - 4(1 + a_2 + a_3)(1 + a_2^3 + a_3^3)$$
$$+ 28\Big((a_3 - a_2)^3 + (a_2 - 1)^3 + (a_3 - 1)^3\Big) + 294\Big((a_3 - a_2)^2 + (a_2 - 1)^2 + (a_3 - 1)^2\Big)$$
$$+ 1372(2a_3 - 2) + 2401 = 2275. \tag{6.9}$$

Solving these two equations gives us the following set of integer solutions: (1,2,4), (1,3,7), (1,5,6), (1,3,4), (1,5,7) and (1,2,6).

As another example, solving these set of equations for parameters (16,6,2) returns no integer solution, which mean there is no difference-set with these parameters.

6.3 On Ryser's Conjecture

There are two main methods presented for the study of difference-sets. The multiplier theorem proposed by Hall in 1947 [78] and the self-conjugacy approach presented by Turyn in 1965 [79] work well for proving the non-existence of difference-set with small parameters, Q, K and λ. Ryser presented a conjecture in 1963 for difference-sets, for which no counter-example has been found. Ryser's conjecture is one of the main open problems in combinatorial mathematics, and only some partial results are known. Turyn's paper is the only work on this conjecture over the years. Ryser's conjecture is a general case of the Barker and circulant Hadamard matrix conjectures [1]. In this section, we prove some lemmas that are related to Ryser's conjecture, and at the end we derive partial results on this conjecture.

Lemma 1 *Let Q, K and λ be the parameters of a difference-set, and p be a prime such that $p|\gcd(Q, K - \lambda)$. Then $p|K$ and $p|\lambda$. In other words, the Ryser's conjecture can be rephrased as follows: when $p|Q$, $p|K$ and $p|\lambda$, then no difference-set exists with parameters (Q, K, λ).*

Proof: It suffices to show that $p|K$. From (1.1), we get

$$K - \lambda = K\left(\frac{Q - K}{Q - 1}\right). \tag{6.10}$$

Since p is factor of the left hand side, it divides $K(Q - K)$, and since p is a factor of Q, it should also be a factor of K^2. This implies that $p|K$, and hence, $p|\lambda$. ∎

Lemma 2 *Let* $\{a_1, a_2, \ldots, a_K\}$ *be a* (Q, K, λ) *difference-set. Define* k_j *as*

$$k_j = \left| \{a_i | a_i \equiv j \,(mod\, p)\} \right|, \qquad j = 0, 1, 2, \ldots, p-1, \tag{6.11}$$

where p *is a prime that divides* Q. *Then*

$$(i) \sum_{j=0}^{p-1} k_j = K,$$

$$(ii) \sum_{j=0}^{p-1} k_j^2 = \lambda \frac{Q}{p} + (K - \lambda),$$

$$(iii) \sum_{j=0}^{p-1} k_j k_{j \oplus \ell} = \lambda \frac{Q}{p}, \qquad \ell = 1, 2, \ldots, p-1,$$

$$(iv) \sum_{j=0}^{p-1} (k_{j \oplus \ell} - k_j)^2 = 2(K - \lambda),$$

where $\oplus$ *is the sum modulo* p.

Proof: (i) The first relation between k_j's is obvious, since their sum is equal to the number of a_i's.

(ii) For the second equation, according to the definitions of k_j's, the number of $(a_j - a_i)$'s plus $Q - (a_j - a_i)$'s that are a factor of p is

$$2 \left(\frac{k_0(k_0 - 1)}{2} + \frac{k_1(k_1 - 1)}{2} + \cdots + \frac{k_{p-1}(k_{p-1} - 1)}{2} \right). \tag{6.12}$$

On the other hand, $(a_j - a_i)$'s and $Q - (a_j - a_i)$'s cover the set Λ, and p divides exactly $\lambda(\frac{Q}{p} - 1)$ elements in $\boldsymbol{\Lambda}$. Thus, we have

$$\sum_{j=0}^{p-1} k_j^2 - \left(\sum_{j=0}^{p-1} k_j \right) = \lambda \left(\frac{Q}{p} - 1 \right). \tag{6.13}$$

Simplifying this and using the result of part (i), we get (ii).

(iii) The third part can be obtained similar to the second part, by counting the number of $(a_j - a_i)$'s and $Q - (a_j - a_i)$'s that are equal to ℓ modulo p, which is $\sum_{j=0}^{p-1} k_j k_{j \oplus \ell}$. This number equals to $\lambda Q / p$, which is the number of integers in $\boldsymbol{\Lambda}$ that are ℓ modulo p.

(iv) The last part is obtained from the results of parts (ii) and (iii). ∎

Lemma 3 *Let $\{a_1, a_2, \ldots, a_K\}$ be a (Q, K, λ) difference-set. For any prime p that $p|Q$ and $p|K$, we have*

$$(-1)^m \binom{2m}{m}\Big(\sum_{i=1}^{K} a_i^m\Big)^2 + 2\sum_{n=1}^{m-1}(-1)^n \binom{2m}{n}\Big(\sum_{i=1}^{K} a_i^n\Big)\Big(\sum_{i=1}^{K} a_i^{2m-n}\Big)$$

$$\equiv \begin{cases} 0 & for \quad (p-1)\nmid 2m, \\ -\lambda\frac{Q}{p} & for \quad (p-1)|2m. \end{cases} \quad (mod\, p)$$

(6.14)

Proof: This relation is obtained by considering (6.7) modulo p. ∎

Lemma 4 *Let $\{a_1, a_2, \ldots, a_k\}$ be a difference-set with parameters (Q, K, λ), and $p > 2$ be a prime factor of Q and K. Then $p| \sum_{i=1}^{K} a_i^m$, for $m = 1, 2, \ldots, \frac{p-3}{2}$.*

Proof: We prove this lemma using induction. To this end, we put $m = 1$ in (6.14), which results in

$$\Big(\sum_{i=1}^{K} a_i\Big)^2 \equiv 0 \pmod{p}. \tag{6.15}$$

Hence lemma is true for $m = 1$. Now assume that the statement is true for any $n \leq m - 1$. Then, p is a factor of $\sum_{n=1}^{m-1}(-1)^n \binom{2m}{n}\Big(\sum_{i=1}^{K} a_i^n\Big)\Big(\sum_{i=1}^{K} a_i^{2m-n}\Big)$. Regarding this fact in (6.14), we conclude that p divides $\binom{2m}{m}\Big(\sum_{i=1}^{K} a_i^m\Big)^2$, and since $p \nmid \binom{2m}{m}$ for $m < \frac{p-1}{2}$, $p| \sum_{i=1}^{K} a_i^m$. ∎

Lemma 5 *Let $\{a_1, a_2, \ldots, a_K\}$ be a general difference-set with parameters (Q, K, λ), and $p > 2$ be a prime factor of Q, K and λ. Then $p| \sum_{i=1}^{K} a_i^m$, for $m = 1, 2, \ldots, p - 2$.*

Proof: This lemma is similar to the Lemma 4, just the divisibility condition of λ by p is added. Through Lemma 4, we know this statement is true for $m < \frac{p-1}{2}$. For $m = \frac{p-1}{2}$ we have

$$(-1)^{(\frac{p-1}{2})} \binom{p-1}{\frac{p-1}{2}}\Big(\sum_{i=1}^{K} a_i^{\frac{p-1}{2}}\Big)^2 + 2\sum_{n=1}^{\frac{p-3}{2}}(-1)^n \binom{p-1}{n}\Big(\sum_{i=1}^{K} a_i^n\Big)\Big(\sum_{i=1}^{K} a_i^{p-1-n}\Big) \equiv 0 \pmod{p},$$

which, using Lemma 4, reduces to

$$(-1)^{(\frac{p-1}{2})} \binom{p-1}{\frac{p-1}{2}}\Big(\sum_{i=1}^{K} a_i^{\frac{p-1}{2}}\Big)^2 \equiv 0 \pmod{p}.$$

Hence, p divides $\sum_{i=1}^{K} a_i^m$ for $m = \frac{p-1}{2}$.

Now we prove the lemma for $\frac{p-1}{2} < m < p - 1$. We use induction to prove this part. Let $m = \frac{p-1}{2} + m'$, where m' is a positive integer smaller than $\frac{p-1}{2}$, and let the statement be true for $n < m$. Considering (6.7) mod p^2 for m', we get

$$2K\left(\sum_{i=1}^{K} a_i^{2m'}\right) + (-1)^{m'}\binom{2m'}{m'}\left(\sum_{i=1}^{K} a_i^{m'}\right)^2 + 2\sum_{n=1}^{m'-1}(-1)^n\binom{2m'}{n}\left(\sum_{i=1}^{K} a_i^n\right)\left(\sum_{i=1}^{K} a_i^{2m'-n}\right)$$
$$-\binom{2m'}{1}Q\sum_{i=1}^{K-1}\sum_{j=i+1}^{K}(a_j - a_i)^{2m'-1} \equiv 0 \pmod{p^2}.$$

(6.16)

In this equation, using Lemma 4, and since $p|K$, p^2 is a factor of the first and second terms. Also, according to the inductive step, and since $2m' < m$, then $p|\sum_{i=1}^{K} a_i^{2m'-n}$. Therefore, p^2 also divides the third term. As a result

$$Q\sum_{i=1}^{K-1}\sum_{j=i+1}^{K}(a_j - a_i)^{2m'-1} \equiv 0 \pmod{p^2}.$$

(6.17)

Now let us consider (6.7) for m,

$$2K\left(\sum_{i=1}^{K} a_i^{p-1+m'}\right) + (-1)^m\binom{2m}{m}\left(\sum_{i=1}^{K} a_i^m\right)^2 + 2\sum_{n=1}^{m-1}(-1)^n\binom{2m}{n}\left(\sum_{i=1}^{K} a_i^n\right)\left(\sum_{i=1}^{K} a_i^{2m-n}\right)$$
$$+\sum_{\ell=1}^{2m}(-1)^\ell\binom{2m}{\ell}Q^\ell\sum_{i=1}^{K-1}\sum_{j=i+1}^{K}(a_j - a_i)^{p-1+m'-\ell} \equiv 0 \pmod{p^2}. \quad (6.18)$$

According to the Euler's remainder theorem, $a_i^{p-1+2m'} \equiv a_i^{2m'} \pmod{p}$, and $(a_j - a_i)^{p-1+2m'-1} \equiv (a_j - a_i)^{2m'-1} \pmod{p}$. Thus, $p|\sum_{i=1}^{K} a_i^{p-1+m'}$ and $p^2|Q\sum_{i=1}^{w-1}\sum_{j=i+1}^{K}(a_j - a_i)^{p-1+m'-1}$, and accordingly (6.18) becomes

$$(-1)^m\binom{2m}{m}\left(\sum_{i=1}^{K} a_i^m\right)^2 + 2\sum_{n=1}^{2m'-1}(-1)^n\binom{p-1+2m'}{n}\left(\sum_{i=1}^{K} a_i^n\right)\left(\sum_{i=1}^{K} a_i^{p-1+2m'-n}\right)$$
$$+2\sum_{n=2m'}^{m'+\frac{p-3}{2}}(-1)^n\binom{p-1+2m'}{n}\left(\sum_{i=1}^{K} a_i^n\right)\left(\sum_{i=1}^{K} a_i^{p-1+2m'-n}\right) \equiv 0 \pmod{p^2}.$$

(6.19)

For $n < 2m'$, $\sum_{i=1}^{K} a_i^{p-1+2m'-n} \equiv \sum_{i=1}^{K} a_i^{2m'-n} \equiv 0 \pmod{p}$, and hence, the second term in (6.20) has a factor of p^2. For $n \geq 2m'$, $p|\binom{p-1+2m'}{n}$, and accordingly, p^2 is a factor of the third term in

(6.20). Using these results, we get

$$(-1)^m \binom{2m}{m} \left(\sum_{i=1}^{K} a_i^m \right)^2 \equiv 0 \pmod{p}, \tag{6.20}$$

and $p| \sum_{i=1}^{K} a_i^m$. ∎

Theorem 1 *Consider the difference set* $\{a_1, a_2, \ldots, a_K\}$ *with parameters* (Q, K, λ). *Let p be a prime such that $p|Q$, $p|K$ and $p|\lambda$, then $k_j \equiv k_0 \pmod{p}$ for $j = 1, 2, \ldots, p - 1$.*

Proof: We expand $\sum_{i=1}^{K} (a_i \oplus j)^{p-1}$ in terms of $\sum_{i=1}^{K} a_i^m$ for $m = 1, 2, \ldots, p - 1$,

$$\sum_{i=1}^{K} (a_i \oplus \ell)^{p-1} \equiv \sum_{i=1}^{K} a_i^{p-1} + \sum_{j=2}^{p} \binom{p-1}{\ell} \ell^{j-1} \sum_{i=1}^{K} a_i^{p-j} \mod p. \tag{6.21}$$

From Lemma 5, $p| \sum_{i=1}^{K} a_i^m$ for $m < p - 1$ and $\sum_{i=1}^{K} (a_i \oplus \ell)^{p-1} \equiv K - k_\ell \pmod{p}$, (6.21) can be rewritten as

$$K - k_\ell \equiv K - k_0 \pmod{p},$$

and this concludes that $k_\ell \equiv k_0 \pmod{p}$. ∎

Theorem 1 can be used to prove the non-existence of difference-sets for some parameters. As an example, we show the non-existence of (141,21,3) difference-set using Theorem 1. **Example 1:** Non-existence of (141,21,3) difference-set ($\gcd(Q, K - \lambda) = 3$):

According to the Theorem 1, for $p = 3$, we have $k_0 \equiv k_j$ for $j = 1, 2$. Define $k_j' \doteq (k_j - k_0)/p$. Then through Lemma 2-(iv), we have

$$k_1'^2 + (k_2' - k_1')^2 + k_2'^2 = 36, \tag{6.22}$$

which does not have any integer solution. Therefore, no (141,21,3) difference-set exists.

Chapter 7

Conclusions and Future Work

This chapter summarizes and concludes the dissertation and proposes future research.

In this dissertation new applications of BIBDs in communications and networking are introduced. A NLOS UV system using spectral encoding using BIBDs for M-ary communication is proposed, and transmitter and receiver structures are presented for encoding and decoding signals in the UV range. An upper bound for evaluating the performance of the system is derived and compared with simulation results. The upper bound closely approximates the bit error probability for various geometries. The maximum achievable data rate for different distances and symbol sizes is calculated, and the data rate is shown to be bounded by ISI and SNR limits. Larger constellation sizes reach higher data rates at short ranges, compared to smaller code lengths. The proposed technique has a better performance compared to OOK for practical link distances. By increasing the elevation angles, the optimum code size becomes larger, since the ISI effect is greater. OOK performs better only for distances longer than 2 km, which results in data rates of around a few kb/s.

Novel modulation schemes, called expurgated PPM, multilevel expurgated PPM and coded-QPSK, using the symmetric BIBD are introduced, and their advantages over PPM and MPPM schemes are described. The new proposed approaches are efficient for peak-power limited communication systems and, therefore, can be used in FSO links and IR UWB communications. The bit-symbol mapping for EPPM is similar to PPM and can be easily implemented since all symbols are pair-wise equidistant. For MEPPM the bit-symbol mapping is more like MPPM and finding optimum mapping requires some work. The symbols in EPPM can be cyclic shifts of each other, which simplifies the transmitter and receiver structures and both can be implemented using

shift-registers. In MEPPM, the symbols are constructed by combining several BIBD codewords. Indeed, the symbols of these schemes can be considered as a subset of combined PPM-PAM symbols. Because of the large constellation sizes that can be achieved, the proposed schemes are more spectrally efficient than MPPM, PPM and EPPM. The same receiver as EPPM can be used to decode the signals for MEPPM. Coded-QPSK is shown to be more energy-efficient compared to PPM, QPSK and BPSK, and requires a lower SNR for the same performance at the expense of a larger required bandwidth for the same bit-rate. In these three proposed modulation schemes, the complements of BIBD codewords can be added to the symbols in order to increase the constellation size and achieve a more spectrally-efficient technique. The application of MEPPM and MAEPPM in dispersive FSO channels is also discussed, and their performances are compared with OOK and PAM. The proposed schemes are shown to outperform existing techniques over dispersive channels.

EPPM and MEPPM are proposed to increase the data-rate in VLC systems. Dimming of the lighting system can be done by changing the BIBD code, achieving an arbitrary level of illumination by using an appropriate code-weight and code-length. The correlation decoder is shown to be optimal for shot-noise limited systems. Two multiple-access methods based on MEPPM, are introduced and compared. The first method, using both OOC and BIBD codes to encode the user data, is shown to have a large distance between symbols. Unlike CCM-OCDMA systems, the parameters of the OOC that is used in C-MEPPM can be chosen independent from the given PAPR, and hence, C-MEPPM is able to provide a lower BER compared to CCM-OCDMA when MAI is the dominating factor. The second technique only uses BIBD codes to construct MEPPM symbols, and, therefore, can have a large constellation size and consequently high bit-rate for each user. It is also able to provide flexible and unequal data-rates to users. According to the numerical results, for low SNR cases the coded-MEPPM technique achieves a lower BER compared to divided-MEPPM, while the latter is preferred in high SNR regimes since it has a lower MAI effect.

Interleaving and overlapping techniques are introduced to increase the bit-rate of EPPM, MEPPM and coded-QPSK in systems with bandwidth-limited channels and sources, respectively. These techniques can be used with MEPPM to further increase the spectral efficiency. The performance of interleaving is evaluated in a practical VLC system, and it is shown to significantly decrease the interference effect between adjacent time-chips in EPPM and MEPPM, and hereby, reduce the error probability at the output of the channel. The overlapping pulses technique is

shown to have a potential to send data up to 5 times faster compared to OOK for a band-limited LED.

Proving the existence of BIBDs for an arbitrary set of parameters is an open problem. This existence problem is discussed, and a new approach is presented that can be helpful in solving the open problems. For a constrained set of parameters necessary and sufficient conditions are given for the existence of BIBDs.

As future work, determining the information rate that each proposed modulation scheme can achieve is of interest. This will help us study the performance of the modulation techniques from an information-theoretic point of view, and investigate how close they come to achieving the channel capacity. Applying BIBDs to OFDM and increasing the distance between OFDM constellations can be considered as another future avenue for the application of combinatorial designs.

Bibliography

[1] C. J. Colbourn and J. H. Dinitz, *Handbook of Combinatorial Designs, 2nd Ed.* Chapman and Hall-CRC, 2007.

[2] Center for Communications Research La Jolla, "Difference set repository," *www.ccrwest.org/diffsets/diff_sets*.

[3] B. Vasic and I. Djordjevic, "Low-density parity check codes for long-haul optical communication systems," *IEEE Photon. Technol. Lett.*, vol. 14, no. 8, pp. 1208– 1210, 2002.

[4] L. Lan, Y. Y. Tai, S. Lin, B. Memari, and B. Honary, "New constructions of quasi-cyclic LDPC codes based on special classes of BIBDs for the AWGN and binary erasure channels," *IEEE Trans. Commun.*, vol. 56, no. 1, pp. 39–48, 2008.

[5] B. Ammar, B. Honary, Y. Kou, J. Xu, and S. Lin, "Construction of low-density parity-check codes based on balanced incomplete block designs," *IEEE Trans. Inf. Theory*, vol. 50, no. 6, pp. 1257–1268, 2004.

[6] D. Pei, *Authentication Codes and Combinatorial Designs*. CRC Press, 2006.

[7] W. Kaut and R. Singleton, "Nonrandom binary superimposed codes," *IEEE Trans. Inf. Theory*, vol. 10, no. 4, pp. 363–377, 1984.

[8] A. Dyachkov, A. Macula, and V. Rykov, "New constructions of superimposed codes," *IEEE Trans. Inf. Theory*, vol. 46, no. 1, pp. 284–290, 2000.

[9] H. Kim and V. Lebedev, "On optimal superimposed codes," *J. Combin. Designs*, vol. 12, no. 2, pp. 79–91, 2004.

[10] P. W. Shor, "Polynomial-time algorithms for prime factorization and discrete logarithms on a quantum computer," *SIAM J. Comput.*, vol. 26, no. 5, p. 14841509, 1997.

[11] S. A. Camtepe and B. Yener, "Combinatorial design of key distribution mechanisms for wireless sensor networks," *IEEE/ACM Trans. Networking*, vol. 15, no. 2, pp. 346–358, 2007.

[12] P. C. Li, "New constructions of lotto designs," *PhD Thesis, University of Manitoba*, 2004.

[13] M. Noshad and M. Brandt-Pearce, "NLOS UV communication systems using spectral amplitude coding," *Proceding of IEEE Global communications conference (GLOBECOM)*, pp. 843–848, Houston, TX, Dec. 2011.

[14] A. Gupta, M. Noshad, and M. Brandt-Pearce, "NLOS UV channel modeling using numerical integration and an approximate closed-form path loss model," *Proceding of SPIE Conference on Free-Space and Atmospheric Laser Communications*, San Diego, CA, Aug 2012.

[15] M. Noshad, M. Brandt-Pearce, and S. G. Wilson, "NLOS UV communications using M-ary spectral-amplitude-coding," *IEEE Trans. Commun.*, vol. 61, no. 4, pp. 1544–1553, Apr. 2013.

[16] Z. Xu and B. Sadler, "Ultraviolet communications: Potential and state-of-the-art," *IEEE Commun. Magazine*, vol. 46, no. 5, 2008.

[17] G. Shaw, A. Seigel, and J. Model, "Ultraviolet comm links for distributed sensor systems," *IEEE LEOS Magazine*, vol. 19, no. 5, 2005.

[18] H. Ding, G. Chen, A. Majumdar, B. Sadler, and Z. Xu, "Modeling of non-line-of-sight ultraviolet scattering channels for communication," *IEEE Journal Sel. Commun.*, vol. 27, no. 9, pp. 1535–1544, 2009.

[19] G. Chen, Z. Xu, and B. M. Sadler, "Experimental demonstration of ultraviolet pulse broadening in short-range non-line-of-sight communication channels," *Opt. Exp.*, vol. 18, no. 10, pp. 10 500–10 509, 2010.

[20] Z. Xu, H. Ding, B. M. Sadler, and G. Chen, "Analytical performance study of solar blind non-line-of-sight ultraviolet short-range communication links," *Opt. Lett.*, vol. 33, no. 16, pp. 1860–1862, 2008.

[21] H. Kumagai, "Fine frequency tuning in sum-frequency generation of continuous-wave single-frequency coherent light at 252 nm with dual-wavelength enhancement," *Optics Letters*, vol. 32, no. 1, pp. 62–64, 2007.

[22] A. Kokh, T. Bekker, K. Kokh, N. Kononova, V. Vlezko, P. Villeval, S. Durst, and D. Lupinski, "Nonlinear LBO and BBO crystals for extreme light sources," *Int. Conf. Advanced Optoelectronics and Lasers*, pp. 127–129, 2010.

[23] M. Ebrahim-Zadeh, "Efficient ultrafast frequency conversion sources for the visible and ultraviolet based on BiB$_3$O$_6$," *IEEE J. Select. Topics Quantum Elect.*, vol. 13, no. 3, pp. 679–691, 2007.

[24] H. Wang and A. M. Weiner, "A femtosecond waveform transfer technique using type II second harmonic generation," *IEEE J. Quantum Elect.*, vol. 40, no. 7, pp. 937–945, 2004.

[25] P. R. Prucnal, *Optical code division multiple access: fundamentals and applications.* CRC Press, 2006.

[26] R. J. Drost, T. J. Moore, and B. M. Sadler, "UV communications channel modeling incorporating multiple scattering interactions," *J. Opt. Soc. Am. A*, vol. 28, no. 4, pp. 686–695, Apr. 2011.

[27] M. R. Luettegen, J. H. Shapiro, and D. M. Reilly, "Non-line-of-sight single-scatter propagation model," *J. Opt. Soc. Am. A*, vol. 8, no. 12, pp. 1964–1972, Dec. 1991.

[28] Z. Xu, "Approximate performance analysis of wireless ultraviolet links," *IEEE ICASSP Conf.*, 2007.

[29] L. Wang, Z. Xu, and B. M. Sadler, "An approximate closed-form link loss model for non-line-of-sight ultraviolet communication in noncoplanar geometry," *Opt. Lett.*, vol. 36, no. 7, pp. 1224–1226, 2011.

[30] M. Brandt-Pearce and B. Aazhang, "Optical spectral amplitude code division multiple access system," *International Symposium on Information Theory*, p. 379, 1993.

[31] J. Proakis and M. Salehi, *Digital Communications, 5th Ed.* McGraw-Hill, 2007.

[32] M. Noshad and K. Jamshidi, "Bounds for the BER of codes with fixed cross correlation in SAC-OCDMA systems," *J. Lightw. Tech.*, vol. 29, no. 13, pp. 1944–1950, 2011.

[33] G. Chen, F. Abou-Galala, Z. Xu, and B. M. Sadler, "Experimental evaluation of LED-based solar blind NLOS communication links," *Opt. Exp.*, vol. 16, no. 19, pp. 15 059–15 068, 2008.

[34] D. A. Guimaraes, *Digital Transmission: A Simulation-Aided Introduction with Vis-Sim/Comm*. Springer, 2009.

[35] M. K. Simon and V. A. Vilnrotter, "Performance analysis and tradeoffs for dual-pulse PPM on optical communication channels with direct detection," *IEEE Trans. Commun.*, vol. 52, no. 11, pp. 1969–1979, Nov. 2004.

[36] M. Z. Win and R. A. Scholtz, "Impulse radio: how it works," *IEEE Commun. Lett.*, vol. 2, no. 2, pp. 36–38, 1998.

[37] S. G. Wilson, M. Brandt-Pearce, Q. Cao, and J. H. Leveque, "Free-space optical MIMO transmission with Q-ary PPM," *IEEE Trans. Commun.*, vol. 53, no. 8, pp. 1402–1412, 2005.

[38] H. Sugiyama and K. Nosu, "MPPM: a method for improving the band-utilization efficiency in optical PPM," *J. Lightw. Tech.*, vol. 7, no. 3, pp. 465–472, 1989.

[39] S. G. Wilson, M. Brandt-Pearce, Q. Cao, and M. Baedke, "Optical repetition MIMO transmission with multipulse PPM," *IEEE J. Sel. Areas Commun.*, vol. 23, no. 9, pp. 1901–1910, 2005.

[40] B. Assanovich and M. H. Lee, "Modification of pulse position modulation for high data UWB systems and multi-user communication," *15th International Conference on Microwaves, Radar and Wireless Communications (MIKON)*, vol. 3, pp. 1024–1027, May 2004.

[41] F. Xu, M. A. Khalighi, and S. Bourennane, "Coded PPM and multipulse PPM and iterative detection for free-space optical links," *J. Opt. Commun. Netw.*, vol. 1, no. 5, pp. 404–415, 2009.

[42] M. Noshad and M. Brandt-Pearce, "Expurgated PPM using balanced incomplete block designs," *IEEE Commun. Lett.*, vol. 16, no. 7, pp. 968–971, 2012.

[43] ——, "Coded QPSK using balanced incomplete block design," *Proceding of Asilomar Conference on Signals, Systems and Computers*, Pacific Grove, CA, Nov 2012.

[44] ——, "Multilevel pulse-position modulation based on balanced incomplete block designs," *Proceding of IEEE Global communications conference (GLOBECOM)*, Anaheim, CA, Dec. 2012.

[45] J. E. Peajcariaac, F. Proschan, and Y. L. Tong, *Convex functions, partial orderings, and statistical applications*. Academic Press, 1992.

[46] M. Noshad and K. Jamshidi, "Code family for modified spectral-amplitude-coding OCDMA systems and performance analysis," *J. Opt. Commun. Netw.*, vol. 2, no. 6, pp. 344–354, 2010.

[47] K. Nikolaidis and M. J. N. Sibley, "Optimum mapping in an optical multiple pulse position modulation link using a maximum likelihood sequence detection scheme," *IET Optoelectronic*, vol. 3, no. 1, pp. 47–53, 2009.

[48] H. Zhang, W. Li, and T. Gulliver, "Pulse position amplitude modulation for time-hopping multiple-access UWB communications," *IEEE Trans. Commun.*, vol. 53, no. 8, pp. 1269–1273, 2005.

[49] Y. Zeng, R. Green, and M. Leeson, "Multiple pulse amplitude and position modulation for the optical wireless channel," *International Conference on Transparent Optical Networks (ICTON)*, pp. 193–196, Aug. 2008.

[50] M. Herceg, D. Zagar, and D. Galic, "Multi pulse position amplitude modulation for ultra-high speed time-hopping UWB communication systems over AWGN channel," *International Symposium on Communications, Control and Signal Processing (ISCCSP)*, May 2010.

[51] L. Zeng, D. ÓBrien, H. Minh, G. Faulkner, K. Lee, D. Jung, Y. Oh, and E. T. Won, "High data rate multiple input multiple output (MIMO) optical wireless communications using white LED lighting," *IEEE J. Select. Areas Commun.*, vol. 27, no. 9, pp. 1654 – 1662, 2009.

[52] D. Zwillinger, *CRC Standard Mathematical Tables and Formulae, 32nd Ed.* Taylor and Francis, 2011.

[53] S. S. Haykin, *Communication Systems, 4th Ed.* John Willey & Sons, 2001.

[54] H. Elgala, R. Mesleh, and H. Haas, "Indoor optical wireless communication: Potential and state-of-the-art," *IEEE Commun. Mag.*, vol. 49, no. 9, pp. 56 – 62, Sep 2011.

[55] M. Noshad and M. Brandt-Pearce, "Application of expurgated PPM to indoor visible light communications - part I: Single-user systems," *submitted to J. Lightw. Tech.*, 2013.

[56] ——, "Application of expurgated PPM to indoor visible light communications - part II: Access networks," *submitted to J. Lightw. Tech.*, 2013.

[57] ——, "Can visible light communications provide Gb/s service?" *submitted to IEEE Commun. Mag.*, 2013.

[58] ——, "High-speed visible light indoor networks based on optical orthogonal codes and combinatorial designs," *Proceding of IEEE Global communications conference (GLOBECOM)*, Athlanta, GA, Dec. 2013.

[59] I. E. S. of North America, "IESNA lighting handbook, 9th ed."

[60] H. L. Minh, D. ÓBrien, G. Faulkner, L. Zeng, K. Lee, D. Jung, and Y. Oh, "80 Mbit/s visible light communications using pre-equalized white LED," *34th European Conference on Optical Communication (ECOC)*, 2008.

[61] I. Stefan, H. Elgala, and H. Haas, "Study of dimming and LED nonlinearity for ACO-OFDM based VLC systems," *Proceeding of IEEE Wireless Communications and Networking Conference*, pp. 990–994, Apr. 2012.

[62] O. Gonzlez, S. Rodriguez, R. Perez-Jimenez, B. Mendoza, and A. Ayala, "Error analysis of the simulated impulse response on indoor wireless optical channels using a Monte Carlo-based ray-tracing algorithm," *IEEE Trans. Commun.*, vol. 53, no. 1, pp. 124–219, Jan. 2005.

[63] K. Lee, H. Park, and J. Barry, "Indoor channel characteristics for visible light communications," *IEEE Commun. Lett.*, vol. 15, no. 2, pp. 217–219, Feb. 2011.

[64] H. Elgala, R. Mesleh, and H. Haas, "Indoor broadcasting via white LEDs and OFDM," *IEEE Trans. Consumer Electronics*, vol. 55, no. 3, p. 11271134, 2009.

[65] C. Kottke, K. Habel, L. Grobe, J. Hilt, L. Rosal, A. Paraskevopoulos, and K. Langer, "Single-channel wireless transmission at 806 Mbit/s using a white-light LED and a PIN-based receiver," *International Conference on Transparent Optical Networks (ICTON)*, We.B4.1, 2012.

[66] J. Yoo and S. Jung, "Multi-coded variable PPM with level cutting for high data rate visible light communications," *18th Asia-Pacific Conference on Communications (APCC)*, Oct. 2012.

[67] A. Yang, X. Li, and T. Jiang, "Enhancement of LED indoor communications using OPPM-PWM modulation and grouped bit-flipping decoding," *Opt. Exp.*, vol. 20, no. 9, pp. 10 170 – 10 179, Apr 2012.

[68] I. Bar-David and G. Kaplan, "Information rates of photon-limited overlapping pulse position modulation channels," *IEEE Trans. Inf. Theory*, vol. 30, no. 3, pp. 455–464, 1984.

[69] M. Guerra-Medina, O. Gonzalez, B. Rojas-Guillama, F. D. J.A. Martin-Gonzalez, and J. Rabadan, "Ethernet-OCDMA system for multi-user visible light communications," *Electronics Lett.*, vol. 48, no. 4, 2012.

[70] J. Salehi and C. Brackett, "Code division multiple-access techniques in optical fiber networks - part I: Fundamental principles," *IEEE Trans. Commun.*, vol. 37, no. 8, pp. 824–833, 1989.

[71] F. Chung, J. Salehi, and V. Wei, "Optical orthogonal codes: design, analysis and applications," *IEEE Trans. Inf. Theory*, vol. 35, no. 3, pp. 595–604, 1989.

[72] P. V. Kumar, R. Omrani, J. Touch, A. E. Willner, and P. Saghari, "A novel optical CDMA modulation scheme: Code cycle modulation," *Proceeding of IEEE Global communications conference (GLOBECOM)*, San Francisco, CA, Nov. 2006.

[73] V. Vilnrotter and M. Srinivasan, "Adaptive detector arrays for optical communication receivers," *Jet Propulsion Laboratory, TMO Progress Rep. 42141*, May 15, 2000.

[74] A. Dutta, *Optimal Cooperative and Non-cooperative Peer-to-peer Maneuvers for Refueling Satellites in Circular Constellations*.   PhD Thesis, Georgia Institute of Technology, 2009.

[75] J. Barry, J. Kahn, W. Krause, E. Lee, and D. Messerschmitt, "Simulation of multipath impulse response for indoor wireless optical channels," *IEEE J. Select. Areas Commun.*, vol. 11, no. 3, pp. 367–379, Apr 1993.

[76] E. W. Weisstein, *CRC Concise Encyclopedia of Mathematics, 2nd Ed*.   Chapman & Hall CRC, 2003.

[77] C. J. Moreno and S. S. W. Jr., *Sums of Squares of Integers (Discrete Mathematics and Its Applications)*.   Chapman & Hall CRC, Taylor & Francis Group, 2006.

[78] M. Hall, "Cyclic projective planes," *Duke Math. J*, vol. 14, pp. 1079–1090, 1947.

[79] R. J. Turyn, "Character sums and difference sets," *Pacific J. Math.*, vol. 15, pp. 319–346, 1965.